Martian Water Frost:

Control of Global Distribution by Small–scale Processes

Thesis by

Tomáš Svítek

In Partial Fulfillment of the Requirements

for the Degree of

Doctor of Philosophy

California Institute of Technology

Pasadena, California

1992

(Defended October 30, 1991)

To my Ivuška

Abstract

This thesis analyzes the small–scale physical processes occurring in the Martian water polar frosts. The small–scale processes are considered from the point of view of how they control the global distribution and behavior of water on Mars. The analysis of the small–scale properties of the surface frost is essential in efforts to find solutions for some outstanding, contradictory observations, to interpret correctly remote sensing observations, to model the surface–frost thermal balance, and to implement the boundary conditions and parameterizations used in the global models of the volatiles' behavior on Mars. Two different problems are investigated in this thesis:

The effect of surface roughness on frost temperature and morphology is studied in Chapter 2 and 3. The investigation of the temperature/roughness feedback leads to the following suggestion: There is a natural tendency of volatile surfaces to develop spontaneously small–scale roughness in a sublimation–dominated environment. The evidence for this claim consists of the model of a rough–surface thermal balance, and of the terrestrial analogs of differential sublimation structures. Such a phenomenon can be tested by the Mars Observer and has important implications for the behavior of water frost on Mars.

Viking Lander 2 winter–frost observations are described in Chapter 4. This study suggests that winter water frost occurred there in two forms: a) thin, almost continuous, early frost, and b) much thicker, patchy, later frost with local cold–trapping of water vapor playing the crucial role. This conclusion is based on the correlation of multiple data sets (from both Viking Orbiter and Lander) and on the combined models of the physical processes occurring on a small scale — below the resolution of remote sensing. The evidence consists of the frost–surface coverage and color transitions, and of the calculation of the vertical and horizontal water–vapor transport near the surface. Again, this phenomenon can be confirmed or rejected by a set of observations from the Mars Observer.

The inherent rough–surface morphology and the frost cold–trapping must be a general property of at least some forms of the seasonal and residual frosts. Both effects must be considered in order to understand the global observations of the Martian frost and the surface environment of Mars in general.

Acknowledgments

It seems incredible to me that it is already six years since I have "reverently" entered the hallowed halls of this institute. At that time, I was new in this country and uncertain of many things. I have changed a lot since that time, and more importantly, I have learnt a great deal. I have found out about the tribulations and joys of conducting scientific research.

This would not be possible without the dedication and perseverance of the department's faculty. In the first place, I thank my advisor, Bruce Murray, for his willingness to take a chance with me, for his inspiration in my work and life, and for his commitment to the students. Many others are owed great appreciation from me: Andy Ingersoll, for countless help in my research, David Stevenson, for inspiration, Ed Danielson, without whom it would have been much more difficult at the beginning of my Caltech career, Yuk Yung, for his sage advice, Arden Albee, for his suggestions and insights, Barclay Kamb, for enabling me to see the seventh continent, and Duane Muhleman, Peter Goldreich, and Jim Westphal, for being available when I needed help.

In addition, I owe abundant thanks for the companionship and support over the years to my friends, inside and outside the department: Bruce, Mark, Tim, Eric, Jesus, and many others. I am certain that I will never forget my years at Caltech.

Martian Water Frost: Control of Global Distribution by Small–scale Processes

CONTENTS

1 Introduction 1

2 Temperature/roughness feedback and volatile surfaces ... 5

2.1 Previous work 7
2.2 Effect of surface roughness on temperature 11
2.3 Quantitative estimates for ΔT 32
2.4 Numerical thermal model for rough surfaces 36
2.5 Diurnal temperature variation of rough surfaces 43
2.6 Conclusions 51

3 Observations and interpretation of *penitentes* on Earth and Mars 52

3.1 *Penitentes* — terrestrial analogs? 54
3.2 Previous studies of terrestrial *penitentes* 60
3.3 Differential sublimation at polar regions 62
3.4 Field observations of differential sublimation in Antarctica 68
3.5 Proposed observational tests 75
3.6 Conclusions 83

4 Role of boundary layer in water–vapor exchange between surface and atmosphere at VL–2 site 85

4.1 Problem 86
4.2 Environmental setting 92
4.2.1 Frost–surface coverage and color 93
4.2.2 Atmospheric temperature 98
4.2.3 Atmospheric water vapor 102
4.2.4 Atmospheric transport 105
4.2.5 Surface temperature 108
4.2.6 Diffusion in the soil 110
4.3 Proposed model of cold–trapping 111
4.3.1 Sublimation of frost 113
4.3.2 Condensation of frost 115
4.3.3 Thermal balance of thin frost layers 117
4.3.4 Surface roughness and water–frost stability 119

4.4 Calculated frost thickness 120
4.5 Boundary–layer transport 123
4.6 Quantitative test of model at VL–2 site 127
4.6.1 Frost surface coverage, its color and timing of transition 127
4.6.2 Water vapor in atmosphere — holding capacity and vertical mixing 130
4.6.3 Conclusions about quantitative tests 134
4.7 Observations of edge of northern seasonal frost during spring 135
4.8 Conclusions 140

5 Summary of Conclusions 142

Bibliography 150

FIGURES

2.1 Geometry used to calculate temperature distribution 14
2.2 Geometry used to integrate over a rough surface feature 23
2.3 Temperature enhancement for visible effect 33
2.4 Temperature enhancement as a function of opening angle 34
2.5 Variation in surface temperature and opening angle 46
2.6 Variation in surface temperature and roughness effect 49
3.1 Examples of terrestrial *penitentes* 56
3.2 Solar–energy input in sky space 64
3.3 Solar energy integrated annually 65
3.4 Differential sublimation structures in Antarctica 69
3.5 Temperature difference inside and outside the ablation grooves 70
3.9 Viewing geometry of polar frost 76
3.10 Suggested signature for rough polar frost — visible 78
3.11 Suggested signature for rough polar frost — infrared 79
4.1 Viking Lander 2 panorama 89
4.2 Early continuous frost 90
4.3 Later patchy frost 91
4.4 Example of pixel retrieval processes 97
4.5 Synthesized atmospheric vertical temperature profile 99
4.6 Atmospheric holding capacity for water vapor 103
4.7 Difference in boundary layer transport on Earth and on Mars 107
4.8 Surface temperature from IRTM and VL–2 footpad sensor 109
4.9 Cartoon of model 112
4.10 Thickness of sublimated frost layer 121
4.11 Synthetic atmospheric profile 126
4.12 Changes of frost surface coverage and color 128
4.13 Estimated vertical mixing in boundary layer 131
4.14 Edge of retreating northern seasonal polar frost 137

TABLES

2.1 Program listing for one–dimensional thermal–diffusion model 38
4.1 List of VL–2 images used to study frost surface coverage 94
4.2 List of VL–2 images used to study frost color changes 96

Chapter 1

Introduction

Three questions comprise the basic idea of this thesis: what, why, and how. The issue of "what" is answered as follows: This work analyzes the small–scale physical processes occurring in the Martian water frost. I consider these small–scale processes from the point of view of how they control the global distribution and behavior of water frost on Mars.

The response to the issue of "why" can be presented in a very powerful manner: Current models of the global behavior of volatiles (water specifically) on Mars on diurnal, seasonal and astronomical timescales (e.g., Jakosky 1985, Paige *et al.*, 1990, Kieffer, 1990, Haberle and Jakosky 1990) fail to explain adequately remote sensing observations from orbiting spacecraft. These observations pose a number of substantial questions including:

- the asymmetry between polar residual frosts at the north and south,
- the relationship of water frost (observed spectroscopically) and carbon dioxide frost (observed radiometrically) at the south residual polar cap,

- the seasonal changes of the southern residual frost albedo,
- the coexistence of water vapor in the atmosphere with the year–around cold–trap at the south,
- the net seasonal exchange of water vapor between regolith and atmosphere,
- the latitudinal distribution of water vapor during spring and summer at the northern polar region,
- the appearance and properties of the Viking Lander 2 frost observed during both winters.

This thesis does not attempt to solve these problems in a comprehensive way. Rather, my objective is limited to addressing the methodology required to arrive at potential answers to the above–mentioned questions. I hope to convince the reader that the analysis of the small–scale properties of the surface frost is essential in efforts to find solutions for some outstanding contradictory observations and to provide appropriate concepts and analytical formulations.

I am specifically choosing two different areas for investigation: a) effect of surface roughness on frost temperature and morphology, and b) Viking Lander 2 winter–frost observations. I am going to use the analysis of small–scale processes to resolve these two questions. And I expect, by succeeding in this approach, to show that future work on the puzzles listed above has to include careful consideration of small–scale physical processes.

It is mandatory to consider these effects if one wants to interpret correctly remote–sensing observations. Both these effects play a fundamental role in the surface–frost,

thermal–balance calculations. In addition, the proper understanding of small scale effects is required to implement correctly the boundary conditions and parameterizations used in the global numerical models of the volatiles' behavior on Mars.

This motivation for my research leads to the reply to the "how" question posed above: I intend to apply a comprehensive analysis of the small–scale physical processes that control deposition, evolution and sublimation of water frost at the polar regions. This primarily encompasses the phenomena acting on a spatial scale less than 100 meters, smaller than a resolution of either Viking orbiting remote–sensing instruments or the modeling grid of a global computer simulation. Simultaneously, I place the major focus in this thesis on an extensive comparison with the *in situ* data and with the terrestrial analogs (when available and applicable).

To summarize, in my thesis research I have focused on:

Effect of surface roughness on frost temperature and morphology — Chapters 2 and 3. What is the effect of the natural (i.e., rough) surface on the behavior of the frost that is deposited on this surface? I have derived an analytic expression for surface temperature modification caused by the surface roughness with the assumptions of a) spherical geometry of a rough–surface feature, and b) Lambertian phase function. Using this analytic expression, it is possible to investigate the temperature/roughness feedback on a surface composed of the volatile material.

The investigation of the temperature/roughness feedback leads to the following suggestion: There is a natural tendency of a volatile surface to develop spontaneously small–scale roughness in a sublimation dominated environment. Evidence for this claim consists of the model of a rough–surface, thermal balance, and of the terrestrial analogs of differential sublimation structures. Such a phenomenon can be

tested by the Mars Observer and has important implications for future studies of the water (and similarly for carbon dioxide) frost on Mars.

Viking Lander 2 winter–frost observations — Chapter 4. In this study, I have investigated the observations of the Viking Lander 2 frost that was observed at the site during both winters. Observations of the VL-2 winter–frost suggest that water frost occurs in two forms: a) thin, almost continuous, early frost, and b) much thicker, patchy, later frost with local cold–trapping of water vapor playing crucial role. This conclusion is based on the correlation of multiple data sets (from both Viking Orbiter and Lander) and on the combined models of the physical processes occurring on a small scale — below the resolution of remote sensing. The evidence consists of the frost–surface coverage and color transitions, and of the calculation of the vertical and horizontal water–vapor transport near the surface. Again, this phenomenon can be confirmed or rejected by a set of observations from the Mars Observer.

I believe that the inherent rough–surface morphology and the frost cold–trapping must be general properties of at least some forms of seasonal and residual frosts. Both effects must be considered in order to understand the global observations of the Martian frost and the surface environment of Mars in general.

Chapter 2

Temperature/roughness feedback and volatile surfaces

The obvious consequence of an irregular surface illuminated by sunlight is varying temperature across the surface. In this chapter I will quantify this uneven temperature distribution and describe its effect on frost sublimation and deposition. Such a temperature distribution will differentially enhance frost sublimation from warmer places. The colder places will have less sublimation or possibly even net deposition of vapor and therefore there may be net accumulation in those areas. Together, these two effects are expected to lead to the development of rough surfaces on Martian H_2O frosts.

We have to ask whether there is any systematic and straightforward relationship between the geometry of surface and temperature. Other parameters, like the albedo, typically prevail in affecting surface temperature. Many complicated feedbacks between frost temperature and its albedo are widely recognized, particularly for mixtures of ice and dust. However, assuming uniform temperature–independent albedo and uniform emissivity across the frost surface, the critical parameters are: 1) slope towards the sun and 2) shadowing of surface elements from sunlight. I plan

to use these two effects to provide a simple method for expressing the relationship between surface roughness and temperature.

Provided there is such a definite relationship between roughness and temperature, then one of these two possibilities arises. If more exposed areas with higher relief are maintained at warmer temperatures, then the surface will get smoother. Roughness would diminish through such negative feedback. Vice versa, if higher relief areas are colder, positive feedback leads to a very rough surface regardless of initial conditions. Such positive feedback is crucial for ideas developed in the next chapter of this thesis. A consideration of the details of a positive feedback mechanism is the subject of this chapter.

There is a long history of investigations dealing with the problem, and they are summarized in the next section (2.1). The physics of temperature/roughness feedback in solar and surface thermal infrared wavelengths is presented in the following section (2.2) and a simple method to estimate quantitatively the effects of this feedback is described. The quantitative aspects of the feedback mechanism are presented next (2.3). Next, the one–dimensional surface temperature model is described (2.4). Finally, the diurnal cycle is introduced into this feedback mechanism (2.5). The conclusions end this chapter (2.6).

2.1 Previous work

The investigation of the surface thermal behavior of naturally rough surfaces of bodies in the solar system has a long history. This section reviews previous studies that attempted to calculate the temperature distribution on rough surfaces in the context of planetary science.

The first serious consideration of this effect was by Pettit and Nicholson (1930), who pioneered measurements of the lunar daytime surface temperature. Later, during the Apollo project, several researchers, mentioned below, considered the relationship between the surface temperature and roughness in order to interpret remote sensing observations of the physical properties of the lunar surface. Saari and Shorthill (1963) developed the first comprehensive numerical model of the brightness temperature of the Moon, including the effects of the crater geometry. Bastin and Gough (1969) developed another two–dimensional numerical model (12x96 grid) to explain the wavelength's dependence, eclipse cooling, and limb–darkening in the lunar thermal infrared observations. Their modeled roughness feature consisted of rectangular troughs. They concluded that the thermal radiation from the Moon exhibits a pronounced directional effect because of the roughness effect on temperature distribution. They also derived a general conclusion about the effect of the surface roughness on surface reflectance at visible wavelengths (i.e., the effective albedo for radiative balance): The rough surface has a higher brightness temperature than the comparable smooth surface made of the same material. However, this is true only if temperature observations are integrated on a scale much larger than the scale of rough–surface features and if the surface is viewed at an oblique emission angle. The higher brightness temperature effectively lowers the apparent

surface Bond albedo from the true value of the surface reflectance of the smooth surface material. Their conclusion included the increase in temperature only from the reradiation effect in thermal infrared wavelengths, not from multiple scattering of sunlight. The authors noted the strong directional effects of the rough surface and certain eclipse–cooling anomalies.

There were three additional studies published dealing with a similar problem: Buhl, Welch, and Rea (1968) developed a crater, hemispherical model including one–dimensional heat conduction to the subsurface. The aim of the model was to explain the temperature distribution inside microcraters. Adorjan, 1969, modeled the temperature distribution inside a lunar crater, primarily for the purpose of interpreting lunar–eclipse observations. Finally, Winter and Krupp in 1971 presented a review paper about the thermal characteristics of the lunar surface roughness.

More recently, other workers have investigated the effects of the surface roughness on temperature for other bodies. Hansen, 1977, developed a model for use in the photometric studies of asteroids. It extended the previous (lunar) models by its wide coverage of wavelengths, temperatures, and phase angles. Other than that, it is a standard model with the spherical craterlike shape subdivided into 65 equal surface elements.

In his Ph.D. thesis, Spencer (1990) developed a comprehensive model of the effect of surface roughness on temperature. However, he dealt with the asteroid observations, and focused on disk–integrated measurements of brightness and temperature and the roughness effect on the Bond albedo. This limits the usefulness of his model for my work.

On the theoretical side, Hapke (1984) studied the temperature/roughness relationship in order to correct his theoretical (Hapke 1981) phase function for the macroscopic roughness. The results were published in the third installment of a classical series developing Hapke's phase function. This is mathematically a very rigorous paper. Again, the primary focus is to calculate the integrated brightness, not the temperature distribution inside a single rough–surface feature.

For terrestrial applications, Pfeffer and Bretherton, 1987, tried to understand the effect of surface roughness on the thermal balance of glaciers. The authors considered how multiple scattering of the sunlight inside crevasses affects the thermal balance of glaciers. They modeled the rough surface with a V–groove structure. The paper points out the important conclusion, applicable for my work as well: One can think about the rough surface as a surface with lower reflectance than the reflectance of an equivalent flat surface made of the same material. They showed how the effective surface reflectance decreases with a rougher surface — the smaller opening angle of the V–groove. They also pointed out the lack of information about the phase function of ice surfaces for varying temperature, grain size, age, etc.

Finally, a study similar in some aspects to this thesis was described in Colwell and Jakosky, 1987, and Colwell *et al.*, 1990. Their study was conducted in parallel with my own work. They calculated the water and methane ice sublimation on comets and outer solar–system satellites. The essential conclusion is analogous to mine: A volatile surface in a sublimation–dominated environment has an inherent tendency to develop substantial surface roughness.

However, there are a number of differences between their work and mine. The obvious one is that I investigate the particulars of this phenomenon for Martian

conditions. Also, I deal extensively with terrestrial analogs — *penitentes* and other differential–sublimation features. I do not merely hypothesize the sublimation features, but I describe the real *penitentes* and other differential sublimation features on the Earth in the next chapter. I also present the actual temperature measurement inside a differential–sublimation feature in Antarctica.

Most importantly, I consider the feedback between temperature and surface roughness for the polar environment in Chapter 3. This is the relevant situation for Mars. Colwell *et al.*, 1990, investigate this effect at the equatorial region.

I also include the effect of surface thermal inertia in my model. The thermal inertia effect was included in most of the lunar models that started as attempts to understand lunar eclipse observations, but was ignored most recently in Colwell *et al.*, 1990.

In previous papers, the results were presented either as a comprehensive analytical expression (Hapke 1984), or as numerical models with strict assumptions (lunar or asteroid models). I have attempted in my work to derive a simple analytic estimate of the temperature difference across a rough surface. This derivation requires quite restrictive assumptions and is intended to bracket the dependence of the feedback on different parameters. and to compare with other natural surface phenomena on Mars.

It is crucial to stress that such a simple model can explain observations only conceptually. The strength of this model (and this thesis) is in providing the basic concept of roughness/temperature feedback on a volatile surface. The investigation of precise details of this feedback process awaits more comprehensive studies

involving a complete, numerical model. There are sophisticated scattering and sublimation analytical models but a comprehensive coupled model would probably have to be implemented with numerical techniques. Future work will also require better observational information about the polar environment on Mars.

2.2 Effect of surface roughness on temperature

In this chapter, these two terms are used: a "rough–surface feature" and a "rough–surface element." The first term (feature) designates the local surface area on the surface with both exposed and depressed parts (e.g., sun–cup, *penitentes*). The second term (element) is reserved for an individual elemental area of these surface features (e.g., bottom of a trough, top of a pinnacle) small enough to be considered as planar for the purpose of insolation and thermal radiation calculations.

Three effects have to be considered in calculating the thermal balance of natural rough surfaces:

- Diminished insolation that is due to the mutual shadowing of rough–surface elements, particularly at low Sun angles.

- Increased surface absorption of sunlight that is due to multiple scattering of solar photons from the walls of surface features. Rough–surface elements provide an additional chance for photons to be absorbed after initial reflection from the surface.

- Modified heat loss by surface thermal infrared radiation from the surface to space. Some surface elements radiate less than to 2π steradians of space, whereas other surface elements are exposed to more than 2π steradians of space. Another way of considering this effect for partially hidden elements is as follows: Normal $\epsilon\sigma T^4$ heat loss to 2π steradians is assumed. However, the surface receives an additional heat input to each surface element from the thermal infrared radiation of the walls of a rough–surface feature, which can be viewed by an individual surface element.

The thermal balance of a rough surface could be precisely determined, in principle, with an exact numerical model. Such an "ultimate" model would have to include multiple components. First, the finite–element heat–transfer model would need to be fully implemented in three dimensions. Second, a ray–tracing algorithm is necessary because of multiple scattering of solar photons from the elements of a rough–surface feature. Third, radiative transfer through the atmosphere has to be included to calculate the atmospheric scattering of sunlight — only direct sunlight is going to be affected by mutual shadowing inside a rough–surface feature. The brightness temperature of the atmosphere also has to be known for the thermal radiation towards the surface. Finally, a robust knowledge of the phase function and its dependence on frost deposition, crystal growth, and frost sublimation, would be essential.

An immense effort would have to be undertaken to interface satisfactorily these pieces together. I do not envision a definitive requirement for such a complex model at this time. And it is doubtful that precise enough atmospheric and surface

information would be available as the needed input. Therefore, I have undertaken to develop a simpler but adequate model, which is presented below.

The thermal balance of a surface element can be expressed in a simplified version as

$$F_D = I_D + I_S + F_W, \tag{2.1}$$

where F_D is the direct thermal infrared flux radiated from the surface element into 2π steradians, I_D is the direct flux of solar radiation absorbed by the surface element, I_S is the solar radiation scattered inside the rough–surface feature and absorbed by the surface element, and F_W is the thermal infrared flux radiated and/or scattered from walls of the rough–surface feature and absorbed by the surface element. The other components of the thermal–balance calculation would be: the latent heat flux from frost sublimation or deposition, the downgoing thermal infrared radiation from the atmosphere, the solar radiation scattered in the atmosphere, the sensible heat flux, and the heat conduction vertically and laterally.

However, only those four items in Equation 2.1 will used initially in this chapter. Later, the heat conduction into the ground (producing an effect of thermal inertia) will be considered (Sections 2.4 and 2.5). In Section 3.5, lateral heat conduction will be used to establish an approximate length–scale for rough–surface features on Mars. Finally, latent heat flux will be applied in Chapter 4, but in a different context than the temperature/roughness feedback of this chapter.

F_D and I_D are familiar expressions:

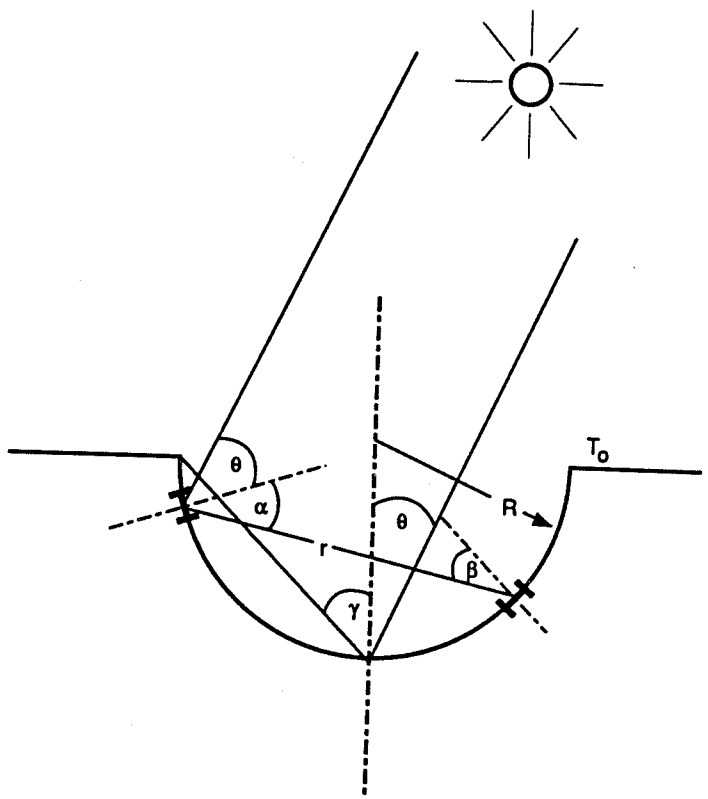

Figure 2.1 Geometry that was used to calculate temperature distribution inside a rough–surface feature

$$F_D = \epsilon\sigma T^4, \text{ and} \tag{2.2}$$

$$I_D = (1 - A)I_{sol}\cos\theta, \tag{2.3}$$

where ϵ is the surface emissivity, σ is the Stefan–Boltzmann constant, T is the surface temperature of the element, A is the surface reflectance measured at the θ incidence angle and integrated over π steradians of the emission angle, I_{sol} is the solar constant, and θ is the solar–angle orientation at the location of the surface element for which the thermal balance is calculated. This calculation assumes the approximation of the solar spectrum by a single solar constant. Only the average value of the surface reflectance is used, and one calculation covering all solar–energy input is performed. The surface emissivity is considered to be uniform everywhere. In the numerical examples in this and the next chapter, the surface emissivity is equal to one. However, I am going to consider the surface emissivity $\epsilon < 1$ for the general derivation in this section (A. Ingersoll, personal communication, 1991).

For the first–generation thermal infrared radiation (no scattering), the radiation absorbed by one surface element and originating from other surface elements of the walls of the rough–surface feature is written as follows:

$$F_{W1} = \frac{1}{\pi}\oint_S \epsilon\sigma T^4 g_S dS, \tag{2.4}$$

where the integral is over the whole inside surface of the rough–surface feature visible from our respective location. g_S is the geometry factor:

$$g_S = \frac{\cos\alpha \cdot P(\beta)}{r^2}. \tag{2.5}$$

α is the angle between the normal vector of this surface element and the vector toward the surface element, which contributes the surface thermal radiation (Figure 2.1). The angle β is a similarly defined but from the point of view of the contributing element. The function $P(\beta)$ is the phase function for the emission at the thermal infrared wavelengths. The distance r is between these two respective elements.

The exact solution of F_{W1} for the thermal balance of a rough surface would require a very complex, numerical integration. Contributions of all the elements of a rough–surface feature have to be considered. Also, mutual shadowing inside this surface feature has to be included, as well. This is a very difficult calculation. The resulting complexity would make it very hard to understand qualitatively the effects of rough, natural surface on temperature.

Therefore, I have used the following observation, which is valid for a spherical shape and for Lambertian phase function. I use these two assumptions to define an "idealized rough–surface feature." With these two assumptions, the integration over all elements inside a rough–surface element does not require the knowledge of the distribution of temperature across this surface. The integral is the same regardless of the position of the observer.

With the assumption of the Lambertian phase function, $P(\beta)$ in the geometry factor g_S (Equation 2.5) can be replaced simply by $cos\beta$. Further, the angles α and β are equal inside the spherical feature, as can be seen in Figure 2.1. Furthermore, this geometric relationship is used:

$$r = R \cdot (cos\alpha + cos\beta). \tag{2.6}$$

With that, g_S and F_{W1} simply become:

$$g_S = \frac{1}{4R^2}, \text{ and} \tag{2.7}$$

$$F_{W1} = \frac{1}{4\pi R^2} \oint_S \epsilon\sigma T_S^4 dS. \tag{2.8}$$

This derivation demonstrates that the contribution of thermal infrared radiation from the walls of a rough–surface feature is *equal* for all elements inside this feature regardless of their location. The derivation is based on these assumptions of the idealized, rough–surface feature: Lambertian phase function, and spherical geometry. This dramatic simplification was also noted previously in several published papers on the roughness/temperature feedback (Adorjan 1969; Hansen 1977; Colwell *et al.*, 1990). It is a rather counter–intuitive concept.

There are several approaches to explain the paradoxical conclusion that surface thermal reradiation does not depend on the details of temperature distribution inside a spherical–surface feature. By the way, the same procedure can also be applied to the multiple scattering at sunlight wavelengths. This simplifying conclusion can be derived for the idealized rough surface: Integrals $\oint_S \epsilon\sigma T^4 dS$ and $\oint_S (1-A) I_{sol} \cos\theta dS$ do not depend on details of the temperature distribution inside a rough–surface feature or on the viewing geometry. These integrals depend solely on the overall integral of the absorbed sunlight or the surface thermal radiation from all surface elements.

One way to understand intuitively this conclusion is to consider that an arc of a circle has always the same angular size as observed from any other position on that circle. In other words, a surface element of the sphere farther from our viewpoint will be smaller because of the greater distance from us, but it will be seen more face–on, therefore contributing equally as a nearer element. This nearer element will be seen as larger, but its contribution to the surface thermal radiation or sunlight–scattering flux will be diminished because of the more sideways viewing angle.

Figure 2.1 describes a two–dimensional case. For this model to be used in three–dimensional situation, it is important to note the following: There is always a single plane defined by three points: 1) the center of the rough–surface feature, 2) the rough–surface element for which the thermal balance is calculated, and 3) the rough–surface element that contributes the reflected sunlight or thermal radiation. In this plane, perpendicular dimensions are constant. Therefore, the three–dimensional case can be calculated using the two–dimensional scheme in Figure 2.1.

This calculation is not strictly accurate for a natural (not idealized) rough surface that does not consist of spherical elements and does not reflect according to the Lambertian phase function. However, even if this calculation is not quantitatively precise, it provides a very useful tool. It is possible to estimate easily the thermal environment for such a surface as will be shown in the rest of this section.

Next, I am going to consider the repeated reflections from the walls. For this calculation, I am using Kirchhoff's law: $1 - A_{TIR} = \epsilon$. Using Equation 2.8 for the surface thermal infrared reradiation covers appropriately only the first generation of thermal infrared radiation that is appropriate for $\epsilon = 1$. The complete F_W contribution includes, also, higher–order terms covering first, second, third, etc.

generations of reflections of thermal infrared radiation from the walls of a rough–surface feature:

$$
\begin{aligned}
F_{W1} &= \frac{1}{4\pi R^2} \oint_S \epsilon\sigma T_S^4 dS \\
F_{W2} &= (\frac{1}{4\pi R^2})^2 \oint_S \epsilon \oint_S (1-\epsilon)\sigma T_S^4 d^2 S \\
F_{W3} &= (\frac{1}{4\pi R^2})^3 \oint_S \epsilon \oint_S (1-\epsilon) \oint_S (1-\epsilon)\sigma T_S^4 d^3 S \\
F_W &= \sum_i F_{Wi} = F_{W1} \cdot [1 - \frac{1}{4\pi R^2} \oint_S dS\,(1-\epsilon)]. \\
&= \frac{1}{4\pi R^2} \oint_S \epsilon\sigma T_S^4 dS \cdot (1 - \frac{1}{4\pi R^2} \oint_S dS\,(1-\epsilon)).
\end{aligned}
\tag{2.8a}
$$

To determined whether Equation 2.8a is reasonable, I am going to calculate the equivalent emissivity of the whole rough–surface feature. This is done by balancing i) the hypothetical thermal infrared radiation flux from the cavity (with the cavity emissivity ϵ_C) and ii) the sum of the direct surface thermal emission out of the rough–surface feature and scattered thermal radiation (with a nominal surface emissivity of ϵ_S):

$$
\begin{aligned}
\frac{1}{4\pi R^2} \oint_S \epsilon_C \sigma T_S^4 dS &= \frac{1-s}{4\pi R^2} \oint_S F_D dS + \frac{1}{4\pi R^2} \oint_S F_W dS \\
&= \frac{1-s}{4\pi R^2} \oint_S \epsilon_S \sigma T^4 dS \\
&+ \frac{1}{4\pi R^2} \oint_S \epsilon_S \sigma T^4 dS \cdot \frac{s}{1-s(1-\epsilon_S)},
\end{aligned}
\tag{2.8b}
$$

where $s = \frac{1}{4\pi R^2} \oint_S dS$. By comparison:

$$
\epsilon_C = \epsilon_S[(1-s) + \frac{s}{1-s(1-\epsilon_S)}]. \tag{2.8c}
$$

This can be confirmed by the following argument:

$$\begin{aligned} s = 0 &\rightarrow \epsilon_C = \epsilon_S, \\ s = 1 &\rightarrow \epsilon_C = 1, \\ \epsilon_S = 1 &\rightarrow \epsilon_C = 1. \end{aligned} \tag{2.8d}$$

The first case is for the flat surface, where multiple scattering plays no role. The second case is for the completely enclosed cavity — black body. In this situation, there is no dependence on the surface emissivity of the material. For the rest of this chapter, I am going to assume the third case: The surface emissivity is uniformly equal to one. It is possible to perform the derivation for arbitrary surface emissivity but the expressions become rather complicated. Also, I have used the surface emissivity equal to one for all numerical examples, primarily because of the lack of good experimental values. Therefore, the surface emissivity will always be set to one in the rest of this chapter.

During the next few pages, I will derive the complete thermal–balance equation for this idealized, rough–surface feature. This will be calculated as an extension of the simple thermal balance:

$$\begin{aligned} F_D &= I_D \\ \sigma T^4 &= (1 - A) I_{sol} \cos\theta. \end{aligned} \tag{2.8e}$$

This calculation will be done in three steps. Initially, only thermal reradiation will be considered in addition to two basic terms (F_D, I_D) in Equation 2.8e. Next, only sunlight multiple scattering will be incorporated in the enhanced thermal–balance

calculation. Finally, both effects will be included (I_S and F_{W1} in addition to F_D and I_D) in the basic thermal–balance equation and the results compared.

Therefore, I am going to consider first the thermal reradiation from the walls as the only modification to the surface thermal balance (factors I_D, F_D, and F_{W1}). The instantenous thermal balance of such a rough–surface element is:

$$\begin{aligned} F_D &= I_D + F_{W1} \\ \sigma T^4 &= (1-A) I_{sol} \cos\theta + \frac{1}{4\pi R^2} \oint_S \sigma T^4 dS. \end{aligned} \tag{2.9}$$

Integrating Equation 2.9 over all elements inside the rough–surface feature results in:

$$\begin{aligned} F_{W1} &= \frac{1}{4\pi R^2} \oint_S \sigma T^4 dS \\ &= \frac{1}{4\pi R^2} \oint_S (1-A) I_{sol} \cos\theta dS + \frac{1}{4\pi R^2} \oint_S \frac{1}{4\pi R^2} \oint_S \sigma T^4 dS^2 \\ &= \frac{1}{4\pi R^2} (1-A) I_{sol} \oint_S \cos\theta dS + \frac{1}{4\pi R^2} \oint_S \sigma T^4 dS \cdot \frac{1}{4\pi R^2} \oint_S dS \\ &= \frac{1}{4\pi R^2} (1-A) I_{sol} \oint_S \cos\theta dS + F_{W1} \cdot \frac{1}{4\pi R^2} \oint_S dS \\ &= \frac{1}{4\pi R^2} \frac{1}{(1-s)} (1-A) I_{sol} \cos\theta_{sol} \int dS, \end{aligned} \tag{2.10}$$

where the identity $\oint_S \cos\theta dS = \cos\theta_{sol} \int dS$ is used and is described below. The parameter $s, = 1/4\pi R^2 \cdot \oint_S dS$, is a fraction of the 4π angular surface taken by the rough–surface feature. The next few paragraphs present a slight detour necessary to explain the terms and formulas in this calculation.

The parameter s from Equation 2.10 is equal to zero for the flat surface, to 0.5 for exactly hemispherical rough–surface features, and to one for the hypothetical, enclosed, rough–surface feature. $\int dS$ is the opening area of the feature. θ_{sol} is the Sun angle for the overall surface (see Figure 2.1). In this expression, there is no multiple scattering from the walls of the feature considered. Constant surface reflectance is assumed. Then, the integral $\oint_S \cos\theta dS$ can be replaced simply by the opening area of the surface feature ($\cos\theta_{sol} \int dS$). All solar photons to be absorbed inside have to enter first through the projection of the opening area in the direction of the Sun.

These two integrals, used in Equation 2.10, are easily calculated for spherical geometry (Figure 2.2):

$$\int dS = \pi r_d^2 = \pi R^2 \sin^2\alpha = \pi R^2 \sin^2 2\gamma, \text{ and} \tag{2.11}$$

$$\begin{aligned}\oint_S dS &= \int_{\alpha=0}^{\alpha=\pi-2\gamma} dS(\alpha) = \int_{\alpha=0}^{\alpha=\pi-2\gamma} 2\pi r(\alpha) dr = \int_0^{\pi-2\gamma} 2\pi R \sin\alpha \cdot R d\alpha \\ &= 2\pi R^2 [\cos\alpha]_{\pi-2\gamma}^0 = 2\pi R^2(1+\cos 2\gamma) = 4\pi R^2 \cos^2\gamma,\end{aligned} \tag{2.12}$$

where γ is the opening angle of a rough–surface feature. It is the angle between the surface normal and the line to the edge of a feature as measured from the bottom of the feature. In summary, note the following identities that are used in this section:

$$\begin{aligned}\frac{1}{4\pi R^2}\oint_S dS &= \cos^2\gamma, \\ \frac{1}{4\pi R^2}\oint_S \cos\theta dS &= \frac{\cos\theta_{sol}}{4\pi R^2}\int dS, \text{ and} \\ \frac{1}{4\pi R^2}\int dS &= \sin^2\gamma\cos^2\gamma.\end{aligned} \tag{2.13}$$

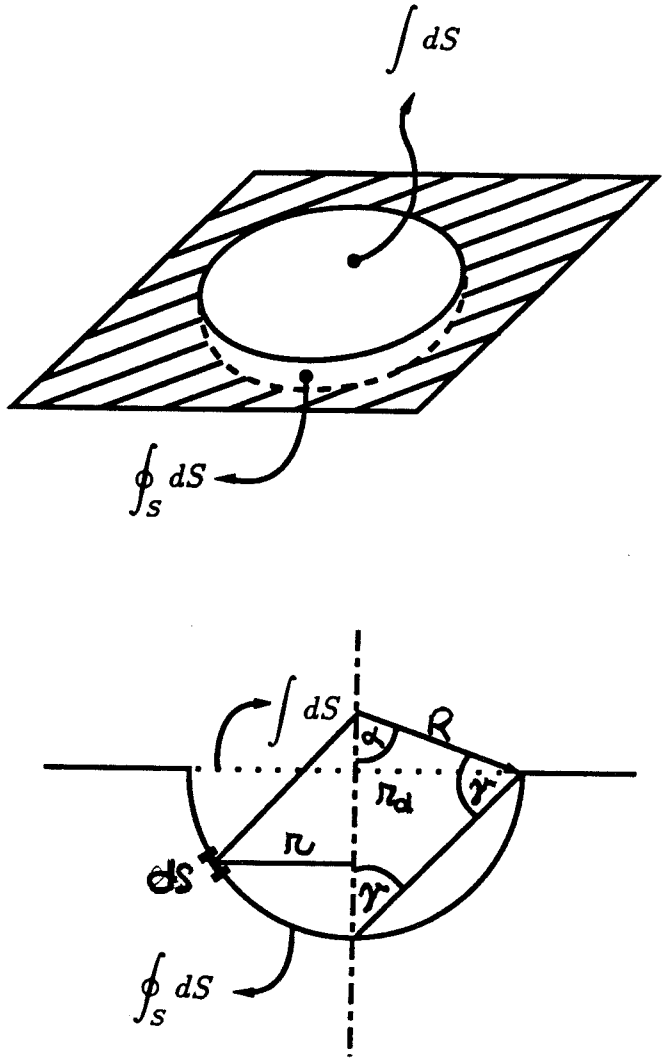

Figure 2.2 Geometry that was used to integrate $\int dS$ and $\oint_S dS$ over a rough–surface feature

Now, we return to the original, thermal–balance calculation (Equation 2.9) and its integral version (Equation 2.10). Equations 2.13 can be used to further simplify Equation 2.10:

$$\frac{1}{4\pi R^2} \oint_S \sigma T^4 \, dS = (1 - A) I_{sol} \cos\theta_{sol} \cos^2\gamma. \tag{2.13a}$$

This is the expression for the average thermal infrared emission inside the spherical rough–surface feature. Equation 2.9 must be used again in its non–integral version to calculate the thermal balance for a specific rough–surface element. For example, Equation 2.14 is valid for the surface element at the bottom of a rough–surface feature, where θ is equal to θ_{sol}, and for direct insolation (the rough–surface element is not in shadow). The assumption of the bottom element is an artificial constraint in the rest of this chapter and the next chapter, imposed principally for convenience of calculation. The derivation could be performed for an arbitrary rough–surface element.

The following expression is derived from Equation 2.9 with the substitution from Equation 2.13a for F_{W1}:

$$\begin{aligned} \sigma T^4 &= (1 - A) I_{sol} \cos\theta_{sol} + (1 - A) I_{sol} \cos\theta_{sol} \cos^2\gamma \\ &= (1 - A) I_{sol} \cos\theta \cdot (1 + \cos^2\gamma) \end{aligned} \tag{2.14}$$

Therefore:

$$\left(\frac{T}{T_0}\right)^4 = 1 + \cos^2\gamma, \tag{2.15}$$

where T_0 is the surface temperature for the equivalent flat surface:

$$T_0^4 = (1 - A)I_{sol} \cos\theta/\sigma. \tag{2.16}$$

This is a very important result. It shows that the temperature will be enhanced at the bottom of an idealized rough–surface feature over the equivalent temperature for a flat surface.

The second step of this three–step calculation of thermal balance of a rough–surface feature is to include only sunlight multiple scattering from the walls of a rough–surface feature (in addition to the basic F_D and I_D). The enhanced energy input enabled by sunlight multiple scattering does not change the temperature distribution inside the rough–surface features for the type of idealized surface described above (spherical and Lambertian). Energy flux is increased by the same amount everywhere because all points inside the feature receive an equal contribution of scattered sunlight energy from all other points (i.e., I_S in Equation 2.1 does not depend on the surface–element location).

The calculation proceeds in a similar way in the case of multiple scattering of sunlight except that the assumption of the Lambertian phase function is doubtful at solar wavelengths (it is quite correct at thermal infrared wavelengths). In addition, the surface reflectance becomes another free parameter. The calculation will be performed for direct (I_D) and scattered (I_S) sunlight only, without the surface thermal infrared reradiation (F_{W1}):

$$F_D = I_D + I_S, \tag{2.17}$$

where a multiple scattering component results from adding first, second, third, etc. generations of reflections from the walls of a rough–surface feature:

$$\begin{aligned} I_{S1} &= (1-A)\frac{1}{\pi}\oint_S AI_{sol}\cos\theta g_S dS \\ &= (1-A)AI_{sol}\frac{1}{4\pi R^2}\oint_S \cos\theta dS \\ &= (1-A)AI_{sol}\cos\theta_{sol}\sin^2\gamma\cos^2\gamma \end{aligned}$$

$$\begin{aligned} I_{S2} &= (1-A)\frac{1}{\pi}\oint_S A\frac{1}{\pi}\oint_S AI_{sol}\cos\theta g_S dS g_S dS \\ &= (1-A)A^2 I_{sol}\frac{1}{4\pi R^2}\oint_S \cos\theta dS\frac{1}{4\pi R^2}\oint_S dS \\ &= (1-A)A^2 I_{sol}\cos\theta_{sol}\sin^2\gamma\cos^4\gamma \\ &= I_{S1}\cdot A\cdot\cos^2\gamma \end{aligned} \tag{2.18}$$

$$\begin{aligned} I_{S3} &= I_{S2}\cdot A\cdot\cos^2\gamma \\ &= I_{S1}\cdot(A\cos^2\gamma)^2 \end{aligned}$$

$$\begin{aligned} I_S &= \sum_i I_{Si} = \frac{I_{S1}}{1-A\cos^2\gamma} \\ &= (1-A)\cdot A\cdot I_{sol}\cos\theta_{sol}\,\frac{\sin^2\gamma\cos^2\gamma}{1-A\cos^2\gamma.} \end{aligned}$$

Substituting this expression in the original formula $F_D = I_D + I_S$ yields:

$$\begin{aligned} \sigma T^4 &= (1-A)I_{sol}\cos\theta_{sol} + (1-A)AI_{sol}\cos\theta_{sol}\,\frac{\sin^2\gamma\cos^2\gamma}{1-A\cos^2\gamma} \\ &= (1-A)I_{sol}\cos\theta_{sol}\frac{1-A\cos^4\gamma}{1-A\cos^2\gamma}, \text{ and} \end{aligned} \tag{2.19}$$

$$\left(\frac{T}{T_0}\right)^4 = \frac{1 - A\cos^4\gamma}{1 - A\cos^2\gamma.} \tag{2.20}$$

The third (final) step of this three–step calculation is for inclusion of both sunlight multiple scattering and the surface thermal infrared reradiation:

$$\begin{aligned} F_D &= I_D + I_S + F_{W1} \\ \sigma T^4 &= (1-A) I_{sol} \cos\theta \\ &\quad + (1-A) I_{sol} \cos\theta_{sol} \frac{\sin^2\gamma \cos^2\gamma}{1 - A\cos^2\gamma} \\ &\quad + \frac{\oint_S \sigma T^4 dS}{4\pi R^2.} \end{aligned} \tag{2.22}$$

The next step is to integrate the last equation over the whole rough–surface feature (this was also done before for the thermal reradiation case):

$$\begin{aligned} F_{W1} &= \frac{1}{4\pi R^2} \oint_S \sigma T^4 dS \\ &= (1-A) I_{sol} \frac{1}{4\pi R^2} \oint_S \cos\theta dS \\ &\quad + (1-A) I_{sol} \cos\theta_{sol} \frac{\sin^2\gamma \cos^2\gamma}{1 - A\cos^2\gamma} \frac{1}{4\pi R^2} \oint_S dS \\ &\quad + \frac{1}{4\pi R^2} \oint_S \sigma T^4 dS \cdot \frac{1}{4\pi R^2} \oint_S dS \\ &= (1-A) I_{sol} \cos\theta_{sol} \frac{\cos^2\gamma}{1 - A\cos^2\gamma.} \end{aligned} \tag{2.23}$$

Therefore:

$$\begin{aligned} \sigma T^4 &= (1-A) I_{sol} \cos\theta_{sol} \left(1 + \frac{A\sin^2\gamma\cos^2\gamma}{1 - A\cos^2\gamma} + \frac{\cos^2\gamma}{1 - A\cos^2\gamma}\right) \\ &= (1-A) I_{sol} \cos\theta_{sol} \frac{1 + \cos^2\gamma - A\cos^4\gamma}{1 - A\cos^2\gamma} \end{aligned} \tag{2.24}$$

yields this comphrensive expression for the surface temperature at the bottom of a rough–surface feature:

$$\left(\frac{T}{T_0}\right)^4 = \frac{(1+\cos^2\gamma - A\cos^4\gamma)}{1 - A\cos^2\gamma.} \tag{2.25}$$

At this point, it is possible to check the results for reasonableness. The average element temperature inside the rough–surface feature is defined as follows:

$$\langle T^4 \rangle = \frac{\oint_S T^4 dS}{\oint_S dS}, \tag{2.25a}$$

and, using Equation 2.23,

$$\frac{\langle T^4 \rangle}{T_0^4} = \frac{1}{1 - A\cos^2\gamma}. \tag{2.25b}$$

Two extreme cases are for $\gamma = 90°$ (flat surface):

$$\langle T^4 \rangle = T_0^4, \tag{2.25c}$$

and for $\gamma = 0°$ (closed cavity $\approx$ black body),

$$\langle T^4 \rangle = I_{sol}\cos\theta_{sol}/\sigma. \tag{2.25d}$$

The former case makes sense because there should be no roughness effect on the flat surface. The latter relationship corresponds to the albedo–independent temperature

inside the (almost) completely closed rough–surface feature which is also sensible. This quick "sanity" check gives support to the robustness of the conclusions of this calculation.

Finally, the results are summarized below. The final calculation (both multiple–scattering and thermal–reradiation effects included) is compared with the two previous conclusions for the surface thermal balance with only the direct sunlight or the thermal infrared reradiation:

$$\left(\frac{T}{T_0}\right)^4 = \begin{cases} 1+\cos^2\gamma & \text{thermal reradiation} \\ (1-A\cos^4\gamma)/(1-A\cos^2\gamma) & \text{multiple scattering} \\ (1+\cos^2\gamma-A\cos^4\gamma)/(1-A\cos^2\gamma) & \text{both} \end{cases} \tag{2.25e}$$

Equation 2.25 is the concluding expression of this section. It describes the instantaneous thermal balance of a surface element at the bottom of an idealized rough–surface feature. This balance is a function of an opening angle γ of that feature. It is based on an assumption of a) spherical geometry, b) Lambertian phase function in both solar and surface thermal infrared wavelengths, and c) uniform emissivity equal to one. The numerical results based on this derivation are presented in the following section.

These results seem qualitatively valid to me also for the non–idealized surface even though it is rather difficult to quantify the differences between the idealized and non–idealized surface without solving the thermal balance for the non–idealized surface. The departures from the idealized surface, described above, are noted:

- **Emissivity not unity.** The calculation presented above does not treat the case of surface emissivity smaller than one. The final thermal–balance equation

(2.22) should include the additional terms F_{Wi} accounting for the reflected thermal radiation inside the rough–surface feature. Such a solution can be derived utilizing Kirchhoff's law $1 - A_{TIR} = \epsilon$. However, I expect that the fundamental nature of the enhanced temperature that is due to the surface roughness is not altered by including this effect. The surface emissivity of natural solid surface is, in general, quite high ($\epsilon \approx 0.90$). Therefore, the surface–temperature distribution of rough–surface elements will not be changed drastically. But it would be necessary to include this effect for a more detailed and sophisticated model.

- **Location of rough–surface element.** The derivation above was restricted to the rough–surface element at the bottom of the surface feature. This was done to simplify numerical computations. However, the theory can be extended to any arbitrary location inside the rough–surface feature.

- **Non–uniform emissivity.** The same statement can be applied here, as well. Because the effect of the surface emissivity not equal to one is not significant, the variations in this emissivity will have only a second–order effect. Again, it would be essential to include this effect in more sophisticated models of the rough–frost, surface–temperature balance.

- **Non–Lambertian phase function at solar wavelengths.** This is probably the most serious departure because it can significantly diminish multiple scattering of sunlight from the walls of a rough–surface feature. It is known that the ice and frost surfaces have distinctly non–Lambertian phase function with the comparably higher–phase integral q. However, because in the case of the Martian polar frost the Sun angle is always low, the reliance on wide dispersion of reflected sunlight caused by the Lambertian phase function is not so critical

as it would be for more equatorial frost. Therefore, I conclude that for polar frost, the temperature/roughness feedback is not substantially altered by the non–Lambertian phase function of the frost surface.

- **Non–Lambertian phase function at the thermal infrared wavelengths.** From the limited information available about the phase function of a potential Martian polar frost, it can be concluded that there is not significant non–Lambertian phase function departure at the thermal infrared wavelengths. Therefore, any potential effect is probably small.

- **Non–uniform surface reflectance.** This could possibly result in a significant departure from the idealized surface geometry caused by temperature/roughness feedback. But it still would contribute toward spontaneously developed, small–scale roughness. The surface elements with the initial lower surface reflectance would sublimate faster and thus create deeper surface features. The elements with higher surface reflectance would not sublimate as fast, and with the added effect of higher surface–reflectance elements having lower temperatures, the positive feedback between roughness and temperature would still be active, and, would likely would enhance roughness. Only the exact geometry would be affected by the inital surface reflectance variations.

- **Non–spherical geometry.** This departure from the idealized rough–surface may be the hardest to quantify. However, there is one important argument as to why the temperature/roughness feedback is still active even for non–spherical rough–surface features: The terrestrial analogs that will be discussed in the next chapter. These analogs are not spherical, at all, but the feedback

between temperature and roughness is responsible for creating these structures. Pffefer and Bretherton, 1987, studied temperature distribution inside a V–shaped groove. They arrived at a similar conclusion about temperature enhancement inside a rough–surface feature. Therefore, I conclude that temperature/roughness feedback is a general relationship that does not depend on unique, spherical geometry.

- **Solid–state greenhouse.** The existence of any potential solid–state greenhouse is not expected be an impediment for the creation of rough–surface features. This is based on the assumption that the length–scale of rough–surface features is larger than the characteristic depth for sunlight absorption in the frost (Brown and Matson, 1987).

2.3 Quantitative estimates for ΔT

This section presents the numerical results derived from the expressions derived in the previous section. The temperature enhancement calculated from the instantenous surface thermal balance of the idealized rough–surface feature of the previous section (i.e., spherical geometry and Lambertian phase function) is presented in Figures 2.3 and 2.4.

Figure 2.3 deals with multiple scattering of sunlight only. This is an idealized surface that cannot exist in reality, but the calculation was performed to isolate and compare effects of sunlight multiple scattering and thermal reradiation. The temperature enhancement $T - T_0$ (y–axis) is plotted as a function of the opening

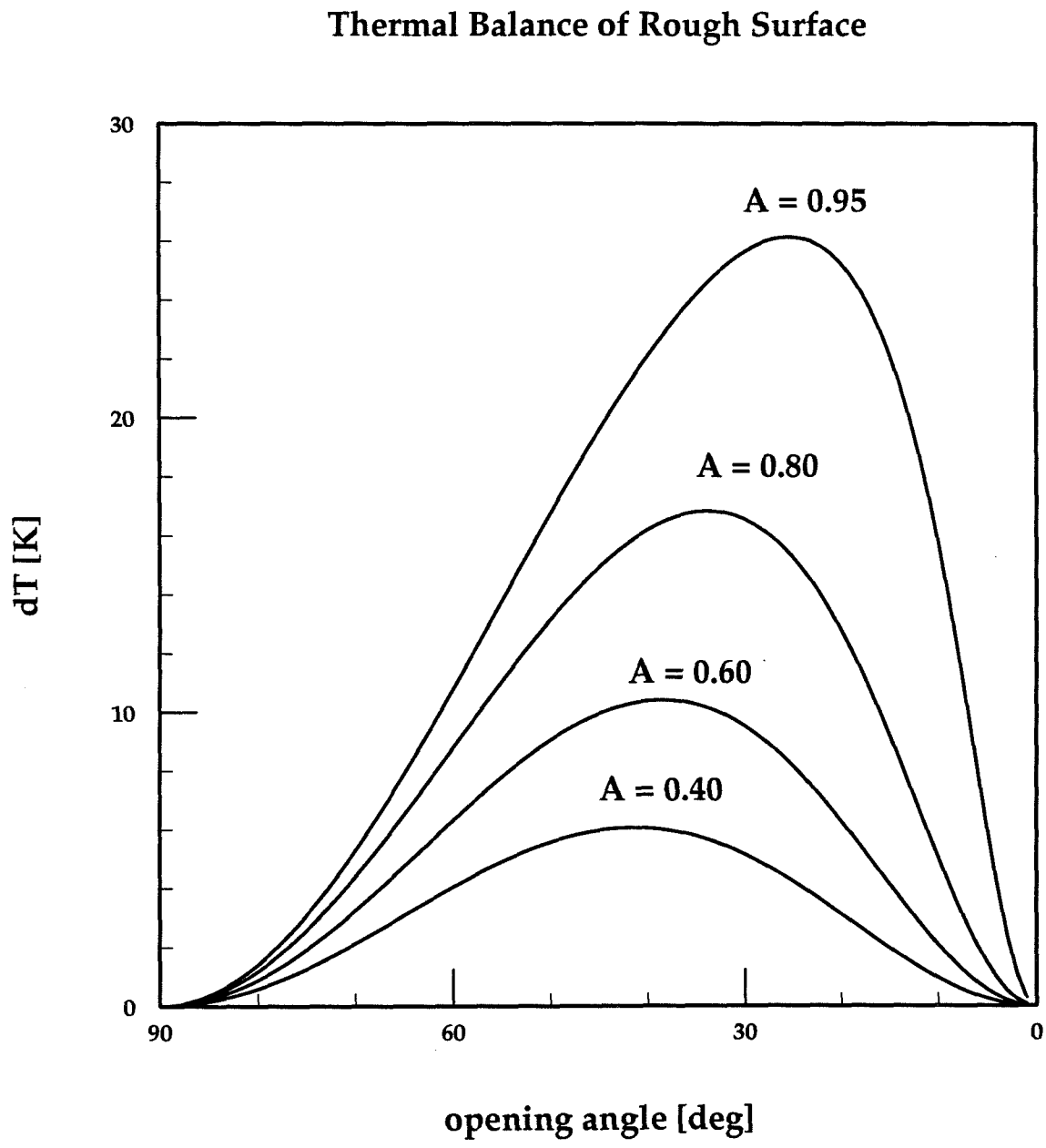

Figure 2.3 Temperature enhancement ΔT as a function of opening angle γ. Surface reflectance A is treated as a free parameter. Only the roughness effect in solar wavelengths (i.e., multiple scattering) is considered for this calculation.

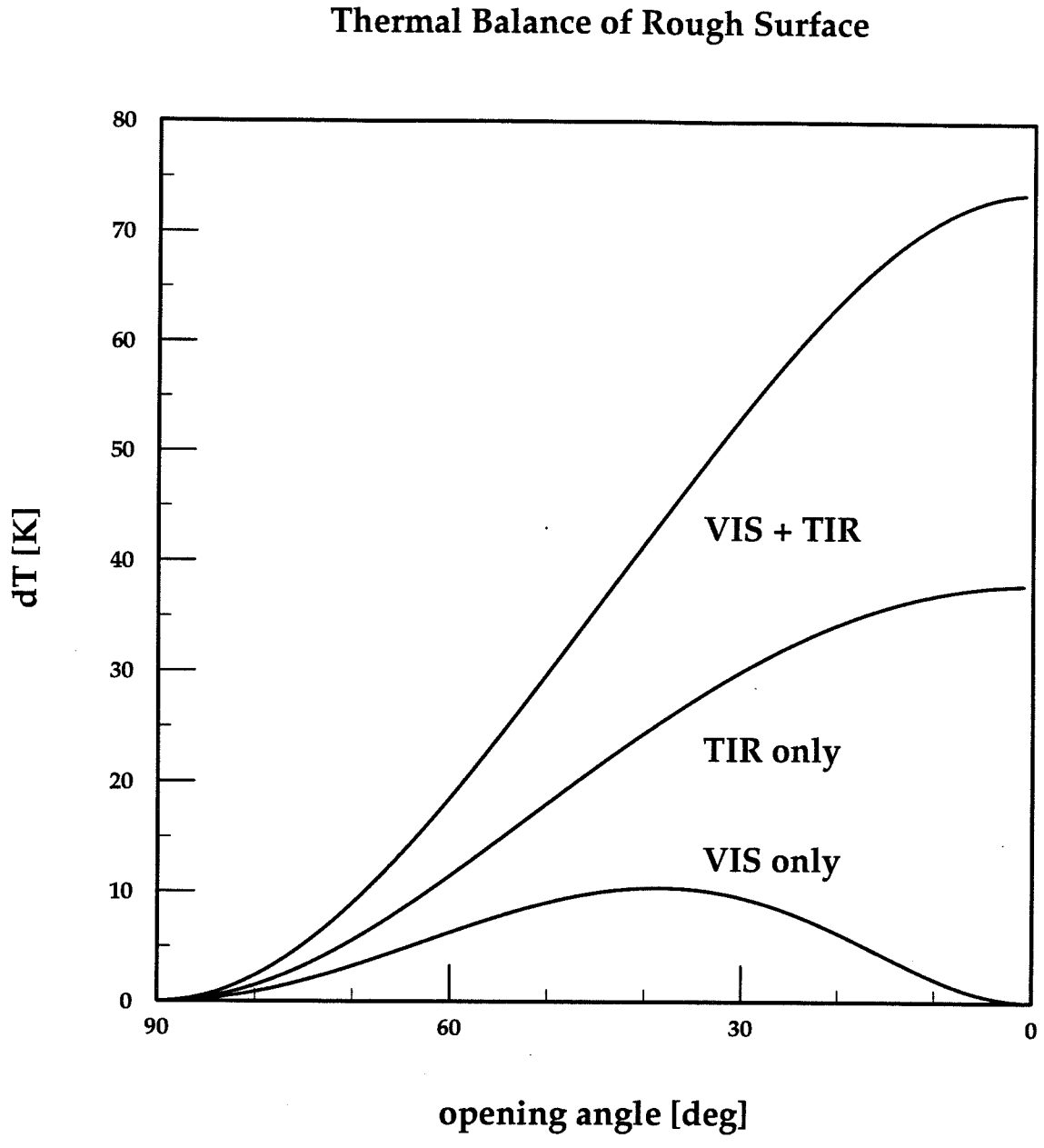

Figure 2.4 Temperature enhancement ΔT as a function of opening angle γ. Roughness effect in both solar and surface thermal infrared wavelengths is considered for this graph. Surface reflectance A is 0.60. Nominal temperature is 200 K.

angle γ (x–axis). The leftmost point on the x–axis is for $\gamma = 90°$, which is a flat surface. The roughness increases towards the right ($\gamma \rightarrow 0°$). The $\gamma = 0°$ would a (hypothetical) completely enclosed rough–surface feature. The surface reflectance A is a free parameter in Figure 2.3.

Figure 2.4 shows both effects (i.e., multiple scattering at solar wavelengths and reradiation at the surface thermal infrared wavelengths) combined. The axes are the same as in Figure 2.3. In both these plots, T_0 is arbitrarily chosen as 200 K, corresponding roughly to higher latitudes on Mars during the spring season. The factors $(1 - A)I_{sol} \cos\theta_{sol}$ are folded into one constant.

Notice the following interesting point: The temperature enhancement $T - T_0$ increases monotonously for the surface thermal infrared reradiation with the opening angle in Figure 2.4. That is, there is an ever higher temperature with rougher surface (with the decreasing opening angle). However, for multiple scattering of sunlight, there is an optimum opening angle for a given albedo. With the decreasing opening angle (i.e., rougher surface), the gain from multiple scattering becomes less important because of the diminishing solar input that is due to the smaller cross–section of a rough–surface feature. This optimum angle increases with the increasing albedo. Initially, brighter surface will become rougher; that is, the rough–surface features will have, overall, a smaller opening angle. This is somewhat counterintuitive because the brighter surface is usually expected to less affected by radiative processes than the comparably darker surface.

Also note the strong mutual enhancement between thermal infrared reradiation and sunlight multiple scattering. If thermal infrared reradiation is present, the reason

for the diminishing effect of sunlight multiple scattering (decreased cross–section) vanishes for the thermally static case.

2.4 Numerical thermal model for rough surfaces

In this section, the instantaneous, surface, thermal balance derived in Section 2.2 will be combined with a one–dimensional, numerical, thermal–diffusion model. The numerical results will be presented at the conclusion of this section. First, I will start with a description of the numerical thermal diffusion model.

Quite possibly, every graduate student in planetary science has at one point had the pleasure of solving numerically the following partial differential equation. This equation relates the time variation of temperature to the thermal gradient, using a finite–differencing method:

$$\frac{\partial T}{\partial t} = D\frac{\partial^2 T}{\partial x^2}. \tag{2.26}$$

A large number of numerical solutions have been described in published literature of the planetary science community (e.g., Kieffer *et al.*, 1977; Jakosky 1982; Paige 1985; Rudy 1988; Clifford 1989). I have used a model adapted from Rudy (1988), which is based on a model of Kieffer *et al.* (1977) (Table 2.1).

Periodically, I have checked the program by running a special set of test cases. These test cases were selected to test the integrity of the model and of the top and bottom boundary conditions. They were chosen in such a way that there was an

analytic solution to the problem. This was possible because the small temperature variations enabled linearization of the problem. Details of the verification will be briefly discussed after the description of the model.

The partial differential equation above first has to be differenced for a numerical calculation. I have used the common, Crank–Nicholson differencing scheme, that is second–order accurate in time but is also quite stable. Crank–Nicholson is considered to be the best scheme for this type of calculation (Press *et al.*, 1988, page 658).

$$\frac{T_i^{n+1} - T_i^n}{\Delta t} = \frac{D}{2}\left[\frac{(T_{i+1}^{n+1} - 2T_i^{n+1} + T_{i-1}^{n+1}) + (T_{i+1}^n - 2T_i^n + T_{i-1}^n)}{(\Delta x)^2}\right]. \tag{2.27}$$

This is then reduced to solving a tridiagonal set of linear equations:

$$-T_{i-1}^{n+1} + \beta T_i^{n+1} - T_{i+1}^{n+1} = T_{i-1}^n - \gamma T_i^n + T_{i+1}^n, \tag{2.28}$$

or in another form as:

$$\begin{bmatrix} \beta_1 & -1 & \cdots & & & & \\ \vdots & \vdots & \ddots & & & & \\ & & -1 & \beta_i & -1 & & \\ & & & & \ddots & \vdots & \vdots \\ & & & & \cdots & -1 & \beta_N \end{bmatrix} \cdot \begin{bmatrix} \vdots \\ T_i^{n+1} \\ \vdots \end{bmatrix} = \begin{bmatrix} \vdots \\ r_i^n \\ \vdots \end{bmatrix}, \tag{2.29}$$

```
#include <stdio.h>
#include <math.h>
#define N 20                              /* number of layers */
const double k = 320.0e-6;                /* thermal conduct (5e-6 => I = 1) */
const double csp = 0.24;                  /* specific heat */
const double rho = 1.00;                  /* density */
const double T_init = 200.0;              /* initial temperature */
const double dx = 1.0;                    /* layer size step */
const double dt = 480;                    /* (dx*dx)/(2*D) => time step */
const double sigma_c = 1.35e-12;          /* Stefan-Boltzmann constant [cgs] */
const double sigma_m = 5.67e-8;           /* Stefan-Boltzmann constant [mks] */
const double I0 = 236.5;                  /* maximum solar insolation [W/m2] */
const double Td = 86400.0;                /* length of day */
const double A = 0.75;                    /* surface ablbedo */
const double g = 90;                      /* opening angle */
const double no_days = 10;                /* integration time */
double r [N], T [N], gamma [N];
void tridag (double b0, double bi, double bN);

void main ()
   {
   const double D = k/(csp*rho);                  /* diffusion constant */
   const double cg = cos (g/57.3);                /* cosine of opening angle */
   const double sg = sin (g/57.3);                /* sine of opening angle */
   const double gf = A*sg*sg*cg*cg / (1-A*cg*cg);
   const double omega = 2*3.141592654/Td;    /* angular velocity of Sun */
   const double ai = dt*D/(2*dx*dx), bi = -(2 + 1/ai), bN = -(1+1/ai);
   double a0, b0, T_sun, Tb3, I, sf;
   long no = 0;
   int i;
   for (i = 0; i < N; i ++)
      T [i] = T_init;
   while (++no*dt <= no_days*Td)
      {
      sf = sin (omega * (no*dt - Td/4));
      I = I0 * sf * (1.0*(sf>0) + gf*(sf>cg)) * (1+cg*cg);
      T_sun = sqrt (sqrt (I / sigma_m));
      Tb3 = (T[0] + T_sun) * (T[0]*T[0] + T_sun*T_sun) / 4;
      a0 = 2 * sigma_c * Tb3 * dt / (csp*rho*dx);
      b0 = -(a0+ai+1)/ai;
      r [0] = (a0+ai-1)/ai * T[0] - (T[1] + 2*a0/ai*T_sun);
      for (i = 1; i < N-1; i ++)
         r [i] = (2-1/ai) * T[i] - (T[i-1] + T[i+1]);
      r [N-1] = (1-1/ai) * T[N-1] - T[N-2];
      tridag (b0, bi, bN);
      fprintf (stderr, "%+7ld %.2lf %.2lf %.2lf\r",
         (long) (no*dt) % (long) Td, T[0], T[N/2], T[N-1]);
      if (no*dt >= (no_days-1)*Td)
         printf ("%+7ld %.2lf\n", (long) (no*dt) % (long) Td, T[0]);
      }
   }
```

Table 2.1 Program listing of the one–dimensional thermal diffusion model

```
void tridag (double b0, double bi, double bN)
   {
   double beta = b0;
   int i;
   T [0] = r[0]/beta;
   for (i = 1; i < N; i ++)
      {
      gamma [i] = 1/beta;
      beta = ((i < N-1) ? bi : bN) - gamma [i];
      T [i] = (r [i] - T [i-1]) / beta;
      }
   for (i = N-1; i > 0; i --)
      T [i-1] -= gamma [i] * T [i];
   }
```

Table 2.1 Cont.

where $\beta_i = 2 + 1/\alpha$ (for $1 < i < N$); β_1 and β_N depend on the boundary conditions and will be described below, $\alpha = D\Delta t/2(\Delta x)^2$, $r_i^n = T_{i-1}^n - \gamma T_i^n + T_{i+1}^n$, and $\gamma = 2 - 1/\alpha$.

This special case of a system of linear equations, called *tridiagonal,* can be solved by this simple routine (Press *et al.*, 1988, page 47):

$\delta = \beta_1;\ \ T_1 = r_1/\delta$

for $i = 2, \ldots, n$

$\gamma_i = 1/\delta;\ \ \delta = \beta_i - \gamma_i$

$T_i = (r_i - T_{i-1})/\delta$

for $i = n-1, \ldots, 1$

$T_i = T_i - \gamma_{i+1} \cdot T_{i+1}.$

The first priority in the development of my program is verification of the basic integrity of the simulation. This is accomplished by simulating the pulse in initial conditions and observing the program's response with a large number of layers (N). This result can then be compared with the well–known analytical solution for a simple, solid–heat diffusion.

The bottom boundary condition allows no thermal energy to escape the simulated system (zero–heat flux across the bottom of the simulated system). It is up to a person running the model to assure that a number of layers are sufficient to assure the required accuracy of simulation. The integrity of the bottom boundary condition can be (and was) verified by running the model for an initial pulse with a small number of layers N. The total heat in the system has to be conserved.

The top boundary condition (ΔF_1 = incoming direct solar radiation – surface thermal radiation) is rather tricky. I have used the following linearization to approximate the heat flux across the top boundary:

$$\begin{aligned}\Delta F_1 &= (1-A)\cos\theta\, I - \sigma T_1^4 \\ &= \sigma T_S^4 - \sigma T_1^4 \\ &= \sigma\,(T_S^2 + T_1^2)(T_S + T_1)(T_S - T_1) \\ &= k_1 \Delta T_1 / \Delta x,\end{aligned} \tag{2.30}$$

where T_S is the equivalent brightness temperature of the Sun at Mars, and k_1 is linearized as follows (T_S and T_1 are used from the previous step):

$$k_1 = \sigma(T_S^2 + T_1^2)(T_S + T_1)\Delta x. \tag{2.31}$$

This quantity is then used in the top layer of heat–diffusion integration instead of regular heat conductivity k_i in $D = k_i/c\rho$.

An initial condition is simply the constant temperature of 200 K throughout the system. The model is then allowed to run for a number of days (≥ 8) to assure the equilibrium state with respect to the solar energy input.

The following is a suggestion for limited verification of correctness of the top boundary condition. Obviously, there is no analytical solution for a non–linear system with σT^4. (If there were one, we would not be forced to use a numerical model.) But we can use the analytical expression for a linear boundary condition (Crank 1954) with quantity C :

$$\frac{C - C_2}{C_0 - C_2} = \text{erfc}\ \frac{x}{2\sqrt{Dt}} - \text{e}^{hx+h^2DT}\text{erfc}(\frac{x}{2\sqrt{Dt}} + h\sqrt{Dt}), \tag{2.32}$$

where $h = \alpha/D$, and α is a proportionality constant in the boundary condition: $D\frac{\partial C}{\partial x} = \alpha(C_0 - C_s)$. This expression can be converted to temperatures:

$$\frac{T - T_{init}}{T_S - T_{init}} = 1 - \text{erfc}(\sqrt{\alpha^2 t/D}). \tag{2.33}$$

Using this solution, a certain degree of confidence can be obtained that the model is correct.

As is readily seen in the expressions above, the solar–brightness temperature T_S is used as a driving function for numerical simulation. It is modulated by $\sin\theta$ to simulate the diurnal cycle:

$$s_f = \sin\omega(n \cdot \Delta t - \frac{T_d}{4}), \tag{2.34}$$

$$T_S = \sqrt[4]{(1-A)I_{sol}/\sigma}, \tag{2.35}$$

$$I_{sol} = \begin{cases} I_0 s_f(1 + \cos^2\gamma)g_f & \text{if } s_f > 0 \\ I_0 s_f(1 + \cos^2\gamma)(1 + g_f) & \text{if } s_f > \cos\gamma, \end{cases} \tag{2.36}$$

where $\omega = 2\pi/T_d$, T_d is length of day (24 hours), and $g_f = A\sin^2\gamma\cos^2\gamma/(1 - A\cos^2\gamma)$. Insolation in this model follows a simple cycle: sunrise at 6 a.m., sunset at 6 p.m., and no atmospheric scattering. The first case in the expression (2.36) for $I_{sol}(s_F > 0)$ occurs when the Sun is above the horizon; some sunlight falls on walls of a rough–surface feature but none at the bottom of the feature. Therefore

the only sunlight is scattered from walls. In the second case ($s_F > \cos\gamma$), there are both the direct sunlight at the bottom element and scattered sunlight from walls.

For this calculation, the latitude effect involves setting a) the value of T_S, and b) the timing of sunrise/sunset. Therefore, this calculation can be applied to a range of possible latitudes. However, the calculation is chosen to be characteristic for roughly 60° North at late spring ($L_S = 340°$). Also, it is assumed in the calculation that the rough–surface feature size is larger than the thermal–skin depth. The situation when the rough–surface feature size is comparable to the thermal–skin depth will be investigated in the next chapter in order to arrive at a characteristic length–scale of these differential–sublimation features on Mars.

In this section, the one–dimensional thermal diffusion numerical model was described. It is going to be used in the next section to describe the effects of temperature/roughness feedback on volatile surfaces over a diurnal cycle.

2.5 Diurnal temperature variation of rough surfaces

In the previous sections, I have described analytical and numerical tools that can be used to study temperature/roughness feedback on rough surfaces. I am going to conclude this chapter by discussing in this section some consequences of this phenomenon.

As I have mentioned above, the principal increase in temperature inside the rough–surface element is from a) thermal reradiation from elements of a rough–surface

feature and b) multiple scattering of sunlight from the same elements. For not very rough surfaces, this increased energy is proportional to $(\pi/2 - \gamma)^2$ for a), and $A \cdot (\pi/2 - \gamma)^2$ for b), where γ is the opening angle and A is the surface reflectance.

The absorbed solar energy for a rough surface will be higher by a factor of $1/(1 - A\cos^2\gamma)$ (Equation 2.25b) than for the equivalent flat surface when illuminated by sunlight. And the thermal infrared energy radiated to space will be smaller by that factor, again. This is valid for the bottom of a rough–surface feature. For the top of such a feature (element at elevated location), the approximate reverse will be true. The temperature for this element will not be higher than the equivalent flat surface temperature because of the additional losses caused by higher than 2π exposure to cold space. In fact, the surface temperature of such an elevated surface element will be lower than of the equivalent flat surface because of the additional thermal–radiation losses.

Also, there will be time shifts. The peak temperature of a bottom element of a rough–surface feature will last a shorter time than the peak temperature for the equivalent flat surface. This is an obvious consequence of the shadowing of direct insolation during sunrise and sunset. For more exposed elements, the reverse is true. These elements will have a faster rise in temperature in the morning and a delayed drop in temperature in the evening from direct insolation. However, the overall temperature rise during the day will be lower than for the equivalent flat surface.

In addition to this reduced–peak temperature duration, there will be a broader "shoulder" of enhanced duration, lasting longer for the bottom elements than for the equivalent flat surface. This is an effect of thermal–radiation shadowing. And

obviously, there will time shifts for different elements across a rough–surface feature. Certain parts of the surface will peak in temperature earlier and others later.

Figure 2.5 shows diurnal temperatures of rough surface for different opening angle γ. Both effects — thermal reradiation and sunlight–wavelengths multiple scattering — are included. The time shifts compared to a flat surface are notable in these graphs. Thermal inertia I and surface reflectance A are fixed. Data in these graphs were calculated by combining the solution of $(F_D = I_D + I_S + F_{W1})$ derived previously with a one–dimensional heat–diffusion model. This was done by inserting the expression derived in Equation 2.25 into the top boundary condition (Equations 2.30 and 2.35).

The "kinks" in Figure 2.5 represent a real effect. They occur at the moment when direct sunlight reaches the bottom element of the rough–surface feature (in the morning) or stops illuminating that particular element (in the afternoon). Even when direct sunlight does not reach the bottom element, that element still receives energy from scattered sunlight and thermal radiation from the walls of the rough–surface feature. This behavior is dependent on the assumption of the spherical–surface geometry but even for the real surface, there would be discontinuous change in the temperature slope.

The expected consequence of varying temperature across the rough, volatile surface is differential–sublimation or condensation on that surface. This results in varying feedback mechanisms, which would cause the surface to get naturally more rough or smooth, depending on the direction of a feedback. This conclusion is plausible only if it is kinematically feasible to move the required amount of frost material.

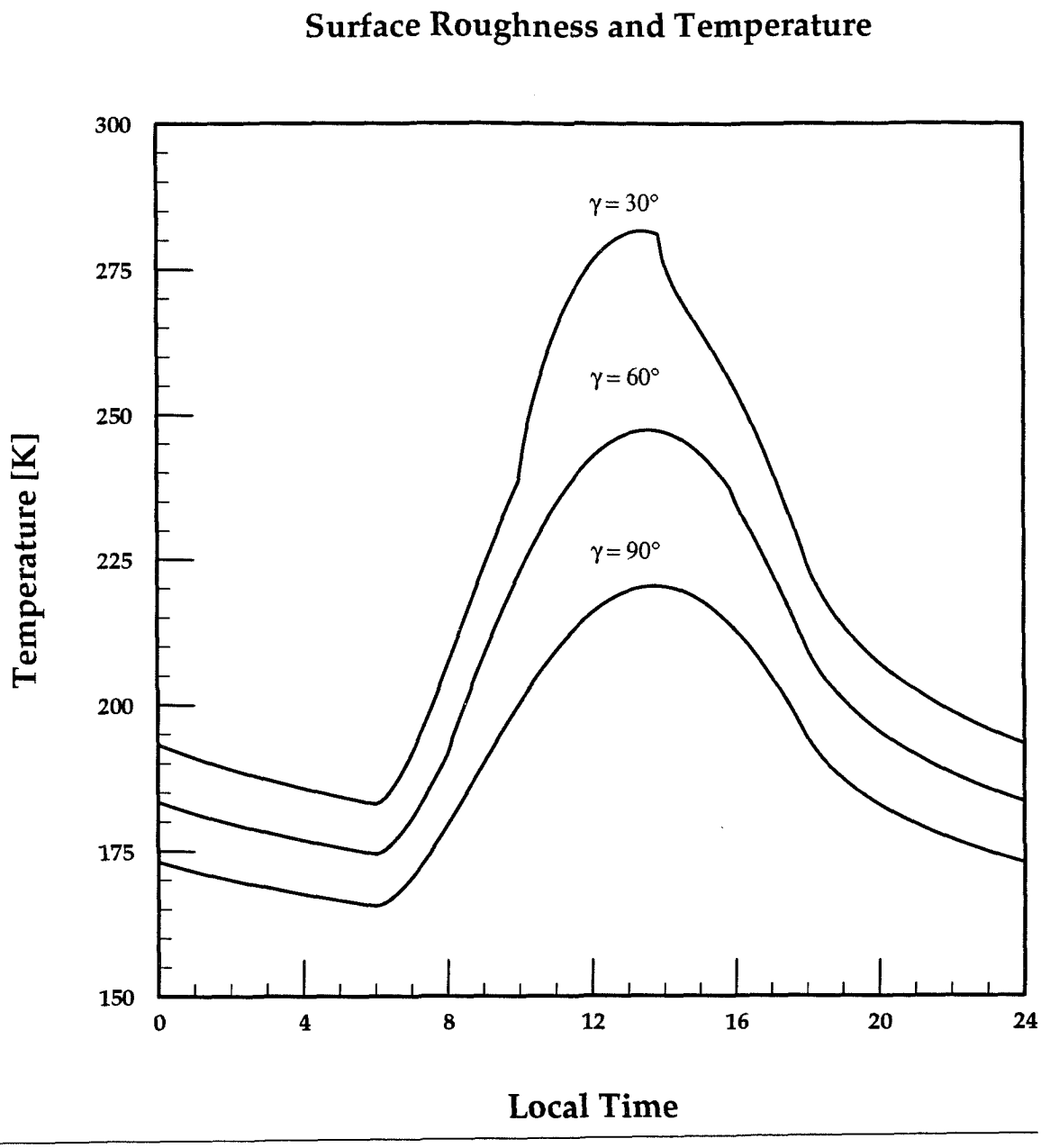

Figure 2.5 Diurnal variation in surface temperature T. Opening angle γ is treated as a free parameter. The curve with the label $\gamma = 90°$ is equivalent to the flat surface. Roughness effect in both solar and surface thermal infrared wavelengths is considered for this graph. Surface reflectance A is 0.75 and surface emissivity ϵ is 1. Thermal inertia I is $8 \cdot 10^{-3}$ in cgs units, which is typical for Martian surface. The temperature is arbitrarily set to an average of 200 K for a flat surface. The "kinks" in the curves are discussed in the text.

The further details of this argument will be discussed in the next chapter, which describes this hypothesized effect in Martian conditions.

Negative feedback will occur if more exposed elements of a rough–surface feature will be warmer than the more hidden elements. This can happen, for example, because the elevated elements are receiving more sunlight than the bottom elements of a rough–surface feature. The overall surface will be inherently smooth. Any rough–surface features will diminish through differential sublimation and deposition.

However, I have tried to demonstrate that the opposite effect is more plausible. That is, more hidden elements will have a higher temperature because of thermal reradiation and multiple scattering at solar wavelengths. This is particularly true for bright — high albedo — surfaces, like frosts. Hence, positive feedback will occur. Any roughness, however small, will reinforce itself. The growth of such features in any typical Martian conditions will be rapid. This is true even when starting from an almost smooth, original surface. Any natural surface will always have some initial roughness.

Obviously, the situation is rather more complicated than simply a division between positive and negative feedbacks. Temporal evolution has to be considered. In reality, both types will occur on the same surfaces at different times. The sublimation rate has to be integrated over time:

$$\frac{dm}{dt} \approx \sqrt{\mu/2\pi RT}\, p_V(T), \tag{2.37}$$

where dm/dt is the rate of frost sublimation, μ is frost–molecular weight, R is the universal gas constant, T is temperature, and p_V is vapor pressure. The exponential

dependence of vapor pressure ($p_V \simeq$ f[exp(T)]) puts a premium on a peak temperature. Terrestrial experience shows that most frost sublimation and redeposition occur within the warmest hour of a day.

Different aspects of surface thermal infrared and solar wavelengths effects can be noticed in Figure 2.6:

1) Multiple scattering of sunlight will extend the duration of the maximum temperature enhancement to a longer period around the local noon. There is a relative minimum of scattering at noon, but it increases in importance with lower solar angles. This will enhance the surface temperature for longer periods.

2) *Vice versa,* thermal reradiation will have the most effect at the maximum temperature. It will not extend the duration of the temperature peak but will enhance the temperature peak itself. This is because the relative enhancement by thermal reradiation is constant over the day. Therefore, the absolute maximum value will be at a time when there would be a temperature peak, anyway.

The relative strengths of sunlight multiple scattering and thermal reradiation effects depend on the most minute details of a particular situation. However, both these effects contribute comparably to bright surfaces. There are several other parameters that will control the exact nature of temperature/roughness feedback. In particular, there are:

A) Surface reflectance. As could be deduced from the quantitative data presented above, rough–surface features made of material with high surface reflectance will produce more significant, positive feedbacks. Eventually, at very low surface

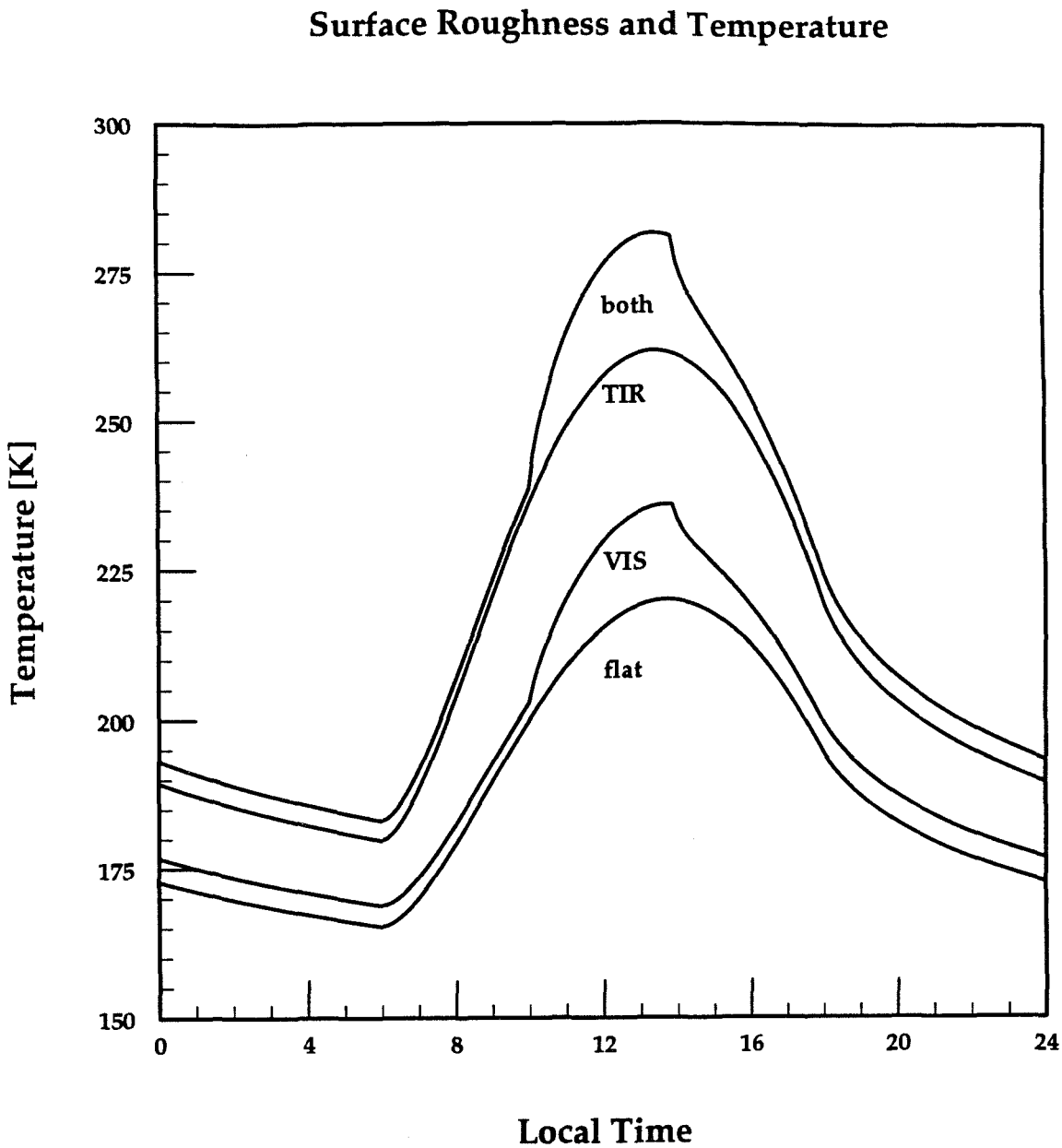

Figure 2.6 Diurnal variation in surface temperature T. Roughness effects in solar and surface thermal infrared wavelengths are plotted separately in this figure, along with diurnal curve for flat surface. Opening angle γ is 30°. Surface reflectance A is 0.75. Thermal inertia I is $8 \cdot 10^{-3}$ in cgs units which is typical for Martian surface. The temperature is arbitrarily set to average 200 K for flat surface.

reflectance (such as ice with high dust content), this feedback can turn negative. However, volatile (frost) surfaces usually have high surface reflectances.

B) Wind speed. There are a whole set of possible interactions between the atmospheric boundary layer and any frost subliming or condensing. Quantitative analysis of this effect is difficult and will not be considered in any comprehensive way in this context. In Chapter 4, there will be a discussion of the possible relationship between the atmospheric state and surface frost sublimation and condensation.

C) Direct vs. atmosphere–scattered sunlight. This is a very crucial parameter. The effect of multiple scattering of sunlight will be the most important for the environment with direct sunlight. From terrestrial experience, it is known that temperature/roughness feedback diminishes, or even reverses, in cloudy conditions. On Mars, this effect may be even more significant because of the higher ratio of atmosphere–scattered to direct sunlight. This is due to the high dust content of the atmosphere.

I have tried to present several ideas regarding the temperature/roughness feedback of volatile surfaces. For a large range of possible conditions, this feedback is positive, and this will produce an inherently rough surface.

2.6 Conclusions

The principal conclusion of this chapter is that there is a positive feedback between surface roughness and temperature distribution across this surface. The consequence of this feedback is rapid and spontaneous development of rough–surface features within the polar frost on Mars. The cause for this effect is the differential sublimation triggered by the positive feedback.

The morphology and properties of the frost surface will thus change drastically. This will significantly alter the apparent Bond albedo and brightness temperature of that surface. The presence of such a rough surface will have a profound effect on many aspects of the volatile cycle on Mars, including surface reflectance temporal changes, H_2O and CO_2 mixture at the southern residual cap, as well as infrared and radar signatures of polar frost. It is mandatory to consider these effects if one wants to interpret correctly remote–sensing observations or model thermal balance of the surface.

I have attempted to describe physical processes occurring on rough, volatile surfaces in a sublimation–dominated environment. After reviewing the previous work in this field and noting its deficiencies, I have presented a simplified model of roughness and temperature relationship. This model exploits an important simplification possible for spherical geometry and Lambertian phase function. I have coupled this model with the one–dimensional thermal diffusion numerical model. Also, I have shown quantitative results with qualitative implications and have presented possible feedback mechanisms.

Chapter 3

Observations and interpretation of *penitentes* on Earth and Mars

In this chapter I am going to discuss the natural property of a volatile surface to develop spontaneously small–scale roughness in a sublimation–dominated environment. This occurs because of the feedback mechanism between surface temperature and surface roughness. This feedback mechanism is controlled by several parameters, which determine if the feedback is positive or negative. These parameters include the Bond albedo, the ratio of direct–to–diffuse sunlight, atmospheric density and surface wind speed. If the feedback is positive, then the surface naturally gets more rough. Otherwise, the surface stays smooth. I believe that this general property of the volatile surface applies, at least in principle, to all volatile surfaces in the solar system, with only a thin atmosphere or none at all. Under these conditions, radiation dominates the heat transport, and vapor sublimation dominates the mass transport. The idea of the naturally rough surface is crucial for correctly interpreting remote–sensing observations and for correlating remote sensing data with *in situ* observations.

To establish plausibility of this phenomenon, I have developed the method of estimating the surface roughness/temperature feedback that was described in the previous chapter. In this chapter, I am, first, going to describe terrestrial analogs (i.e., differential–sublimation features) resulting from the positive feedback between temperature and surface roughness. Such rough–surface features formed in ice are often called *penitentes*, and their presence at both low and high latitudes is reviewed. There is rich, empirical evidence that they occur frequently, under relevant conditions, at low–to–mid latitudes on the Earth. In order for analogous frost features to exist on Mars, it is necessary that the same physical processes be active at high latitudes as well. There is contradictory evidence from the terrestrial experience in Antarctica, and the presence of these features there is disputed by some authors. The principal thrust of the next section of this chapter is to show that a similar effect exists at the polar regions on Earth as well.

The focus of this work is on pure ice behavior. There is obviously a blend of complex interactions of ice and dust mixtures, but I want to concentrate here on understanding the pure ice surface. That understanding is crucial before studying the behavior of mixtures. Also, ice/dust mixture features are more pronounced when sensible heat flux and scattered solar radiation dominate (Takahashi *et al.*, 1973). Under direct solar radiation and with little sensible heat flux (as is the case for Mars), two possibilities can occur. Either the ice in the ice/dust mixture sublimates rapidly, and the surface is quickly covered by the dust only (Kieffer 1990), or the "hot" dust sinks into the frost and thus creates a pure (high–surface reflectance) ice surface (Paige 1985). In both cases, no inherent surface morphology would be produced by the differential–sublimation.

Even if the evidence for terrestrial, polar, differential–sublimation structures is not as obvious as one would wish, I consider it likely that on Mars, peculiar features on the submeter scale cover the surface of the H_2O residual frost at north. The presence of similar features in the residual frost at the south is plausible as well, although the H_2O /CO_2 issue there is not clearly resolved.

As compared with previous studies of this nature, my work puts more emphasis on the existence of terrestrial analogs of Martian differential–sublimation features and on the testing of the hypothesis during future Mars missions (Svitek and Murray, 1988). Therefore, this chapter describes terrestrial analogs observed, first at low, and then at high, latitudes. Also, the ideas for future observations by spacecraft missions are discussed. I propose specific observational tests to determine if the hypothesized inherent roughness is truly found on Mars.

3.1 *Penitentes* — terrestrial analogs ?

The primary motivation for the work described in this section is to ascertain the reality of my claim about the roughness/temperature feedback having a significant impact on volatile surface morphology in a radiation–dominated environment. Are there any analogous, rough–surface features found anywhere on the Earth? The brief answer to this question is a cautious yes. I will describe these analogs in this section and the reason for my reservations in the next sections. However, the importance of identifying terrestrial analogs cannot be overstated. I consider that a very critical element of this work.

These terrestrial analogs are typically called *penitentes* in the glaciological community (Lliboutry 1954). They are commonly found in high and dry mountains at subtropical latitudes, particularly in the Andes. I will deal with these *penitentes* first. Afterwards, I will describe the conditions for the formation of the other types of differential–sublimation features at polar latitudes (ploughshare ice, ablation grooves).

The *penitentes* are ice forms — spikes or blades of compacted snow or ice, roughly arranged in an east–west direction. Under certain conditions, such a conglomeration of sharp pinnacles and deep troughs can cover extensive snow fields. Typical examples are shown in Figure 3.1. The *penitentes* were first observed by Charles Darwin during his Beagle voyage but were incorrectly attributed to the effect of the wind. Sightings of the *penitentes* have been reported from the majority of large mountain ranges on the Earth (Himalayas, Kilimanjaro, Pamir — Troll, 1942), including some poorly formed ones in the Sierra Nevada of the U.S (B. Kamb and N. Humprey; personal communication, also Figure 3.1). The best developed ones are in the Chilean Andes, where they reach heights of up to 8 meters (Lliboutry 1954 and 1956).

It is widely accepted in the glaciological community that a snow or ice surface is relatively smooth if wind is the driving agent of the surface formation (B. Kamb, personal communication). Otherwise, the snow surface tends to be rough if solar radiation is more important than wind action for the surface formation. However, two similar classes of features have to be distinguished: a) the *penitentes*, which form strictly by sublimation at sub–zero conditions, and b) the *suncaps*, which form by snow melting.

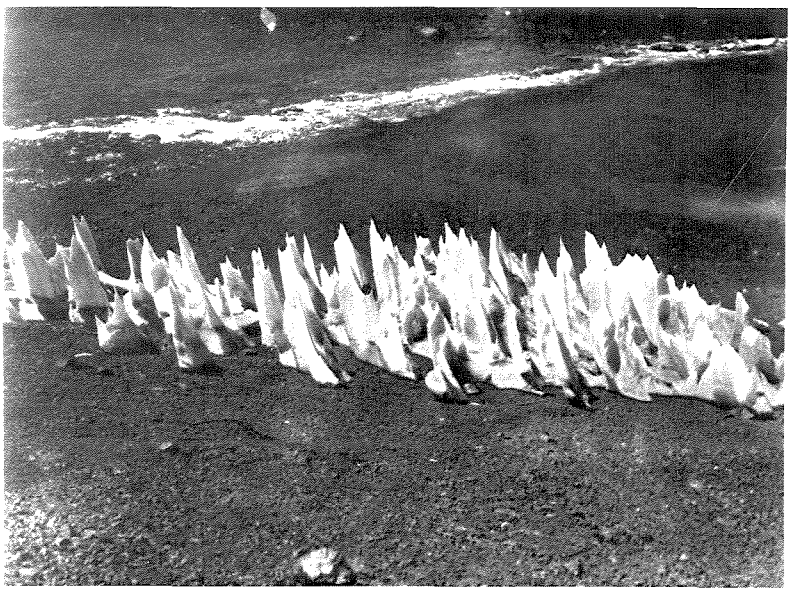

Figure 3.1a,b Examples of terrestrial *penitentes* from the Chilean Andes: a) and b) from Troll, 1942; c) from LLiboutry, 1954; and d) from N. Humprey, personal communication. The first three pictures are from the area near Cerro Azoncagua, which is about 100 km northeast from Santiago. The altitude varies from 12,000 to 18,000 feet. The fourth picture is taken at Plaza de Mulas (14,000 feet), about 80 km northeast from Santiago.

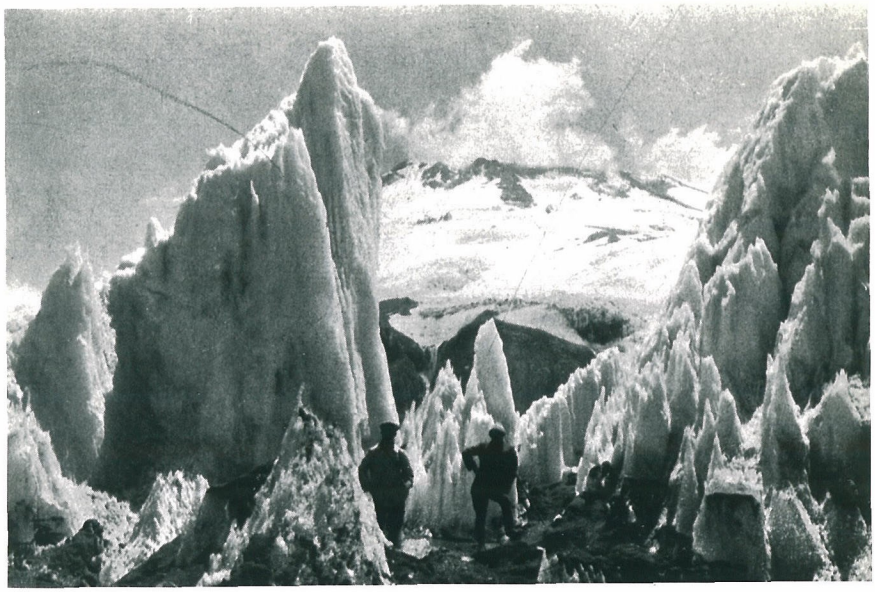

Figure 3.1c,d Examples of terrestrial *penitentes* from the Chilean Andes — cont.

It is also important to note that in this work only dust–free frost features are considered. There are a large number of other phenomena that occur during the sublimation of a frost and dust mixture (for example, Ball 1954; Ashwell and Hannell 1966; Drewry 1972; Malin and Zimbelman 1988). Unfortunately, this topic is beyond the scope of my work.

The terrestrial analogs which I have considered were limited to occurrences only in a sublimation–dominated environment. The term "radiation–dominated environment" is also sometimes used, but I believe that the former is a more precise description than the latter. It will be used consistently in this chapter.

There are three necessary conditions for the presence of terrestrial *penitentes*:

- that the ambient temperature be consistently below freezing
- abundant, direct, non–diffused insolation flux (few or no clouds), and
- low humidity (depressed dew point).

The lower atmospheric pressure at high altitude (above 4000 m) enhances formation of the *penitentes* by limiting the sensible heat flux.

The positive feedback between temperature and roughness starts to enhance any natural variations in the snow surface after it is deposited (among many references, the most important are Lliboutry 1954 and Rhodes *et al.*, 1987). The surface elements at depressed locations, partially hidden, experience higher temperatures and therefore sublimate faster, as was suggested in the previous section. The more exposed surface elements have lower temperatures and are more resistant to snow sublimation. As the relief increases, the differential–sublimation is accelerated, and

the *penitentes* develop steeper slopes. This constitutes the positive feedback. In the extreme case, the snow between *penitentes* is completely gone, and there are only individual pinnacles standing in the surface (Figure 3.1). The typical length–scale for these features is on the order of one meter or slightly less. Of course, much larger features were recorded as well (Figure 3.1).

One slightly controversial aspect of the *penitentes* development is the presence or absence of melting. Some observers (including Lliboutry, 1954) have noted substantial melting of snow between pinnacles of *penitentes*. Others (including me) have not observed any noticeable melting. Both types of *penitentes* evolution evidently occur. The most important observation related to this issue is the following: Regardless of what happens subsequently, the development of *penitentes* occurs solely in a sublimation environment. If there is any melting between pinnacles taking place, it is only because of the temperature enhancement that is due to the high surface relief. Otherwise, on a flat surface, no melting would occur. The only effect melting has is that it accelerates the development of surface roughness (by appreciably lower latent heat of melting than latent heat of sublimation and easier removal of excess matter from troughs of *penitentes*). The presence of low albedo substrate in some *penitentes* (Figure 3.1a) could also have a role in this melting/sublimation issue. However, as stated above, *penitentes* do not require any snow melting to be present.

The characteristic sign of the *penitentes* at low–to–mid latitudes is their approximate east–west orientation. The *penitentes* form rough rows in the direction following the solar positions in the sky. As further evidence of solar control, it was noted that if there was a mountain nearby that affected the distribution of sunlight

by casting a shadow, this tilted the *penitentes* orientation to follow more closely the solar path (Lliboutry, 1954).

3.2 Previous studies of terrestrial *penitentes* and differential–sublimation features

In this section, I am going to review published information about *penitentes* or other differential–sublimation features. I have attempted to include, to the best of my knowledge, all published papers that discuss the postulated feedbacks between temperature and roughness on a pure ice and ice/dust surface.

The first scientific description of *penitentes* was published in the final science report of the second Scott expedition to Antarctica (Wright and Priestley, 1922). The authors discuss quite extensively the field observations of different forms of differential–sublimation features, including several photographs. The first serious investigation of this phenomenon was conducted by the German geologist C. Troll during the 30's. He frequently observed *penitentes* during his field work in South America, and later conducted experiments during the winter in Germany (Troll 1942). His study is an extensive (125 pages) and systematic review of practically all reports of *penitentes* sightings reported so far in all large mountain ranges on the Earth.

The author of the classic explanation of the *penitentes* phenomenon is L. Lliboutry (1954 and 1956). For the first time, the origin of the *penitentes* was explained quantitatively by differential–sublimation. A series of papers published subsequently

attempted to use Lliboutry's work in the context of ice and dust mixtures: "dirt cones," "ablation polygons" (Wilson 1953; Ball 1954; Richardson and Harper 1957; Amstutz 1958). Discusssion of the normal trajectory theory (Ball 1954) and the role of turbulence within the surface boundary layer (Richardson and Harper 1957) appear for the first time.

A series of papers by German authors attempted to develop a numerical model of *penitentes* (von Hofman 1963 and 1967; Kraus 1966). The purpose was to develop comprehensive heat and matter transfer models that could be used to simulate the development of surface morphology made of volatile material. As far as I know, this goal was never achieved.

During the 70's, there appeared another assortment of observational papers with some partially convincing theoretical explanations (Ashwell and Hannel 1966; Jahn and Klapa 1968; Drewry 1972; Kotlyakov and Lebedeva 1974; Hastenrath and Koci 1981). The most important aspect of these papers is that they extend the recorded observations of *penitentes* and other differential–sublimation structures (primarily with ice/dust mixtures) to other geographical areas (Sweden, Poland, Greenland, East Pamir, Peru). A particularly important paper was published by Takahashi *et al.*, in 1973. He described the results of the extensive field and wind–tunnel observations of the development of differential–sublimation features under varying wind conditions. Finally, pictures of *penitentes* appeared in two reference publications published in this period (Post and LaChapelle 1971, Schwerdtfeger *et al.*, 1976).

In 1987, Pffefer and Bretherton published a sophisticated presentation of the effect which roughness has on the thermal balance of a pure ice surface. They used glacier

crevasses as a model for their calculation. Another important paper published that year was by Rhodes, Armstrong and Warren. The primary subject of that study was the effect of direct sunlight or overcast/windy weather on the formation of *penitentes* or differential–sublimation features. They concluded that rough–surface features created by differential–sublimation in pure snow grow under direct sunlight and decay in overcast and windy conditions. The reverse is true for "dirty" snow rough–surface features. This is controlled by the relative magnitudes of radiative and sensible heat fluxes.

Data from Antarctica in Clow *et al.* (1988) are important to assess the sensitivity of the sublimation rate to different ambient conditions. Malin and Zimbelman (1988) suggest the presence of characteristic surface landforms on a cometary nuclei that are due to differential–sublimation of the ice and dust mixture.

3.3 Differential sublimation at polar regions

The terrestrial analogs in low latitudes present us with a convincing argument that positive feedback between roughness and temperature is an important agent in the formation of the morphology of a volatile surface. The problem of extending this phenomenon to Mars is that the *penitentes* do not commonly form on the Earth at the right place. The frequent reports of *penitentes* observations at low latitudes contrast with occasional and not very convincing sightings of *penitentes* structures in the polar regions. Ironically, the most comprehensive study of polar *penitentes* published so far is still the scientific report of the second Scott expedition mentioned earlier. These polar observations are critical for establishing a direct analogy with

Mars. Therefore, it is crucial for my work to investigate the polar environment and its susceptibility for *penitentes* formation in order for this phenomenon to be relevant at all to Mars.

The next few paragraphs present a counterintuitive suggestion about non–uniform solar–energy distribution at the polar regions. At the first approximation, low solar elevation in the polar regions would seem to lead to uniform, azimuthal distribution of solar energy. Thus, there would be no preferred direction for the formation of the differential–sublimation features like the east–west orientation of *penitentes* at low latitudes. However, and this is crucial, sunlight distribution is totally uniform in azimuth only exactly at 90° latitude and for a perfectly level and flat surface.

Even as close to the pole as 85° latitude, the solar energy input in the equatorward direction is about one third larger as compared with the energy input from the poleward direction, as averaged over one year (Figure 3.3). Importantly, the south residual frost of Mars is centered around this latitude, and the north residual frost extends to this latitude range. This is further quantified in Figures 3.2 and 3.3. The graph in Figure 3.2 shows the map of energy distribution in the sky. The x–axis is the azimuth; the y–axis is the elevation. The sum of annually integrated sunlight coming from that direction corresponds to the intensity of the pixel. (The intensity in the map is actually reversed — the blacker the pixel, the more sunlight from that direction.) This was calculated by summing up all the positions of the Sun in the sky throughout the full year. The graph in Figure 3.3 presents data from Figure 3.2 integrated over the Sun elevation.

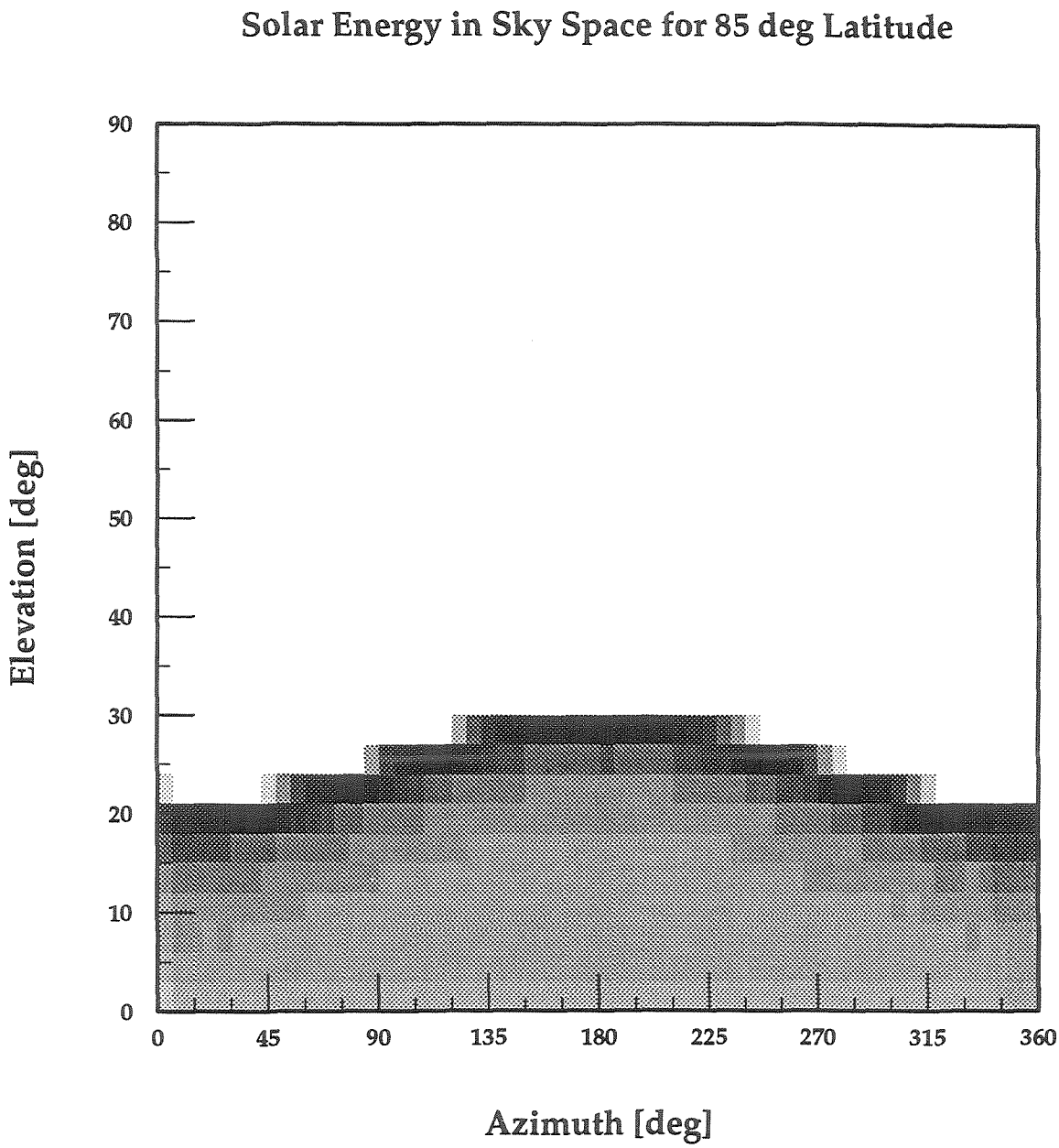

Figure 3.2 Solar–energy input in sky space (x–axis = azimuth, y–axis = elevation; brightness of pixels = annual sum of sunlight coming from that direction)

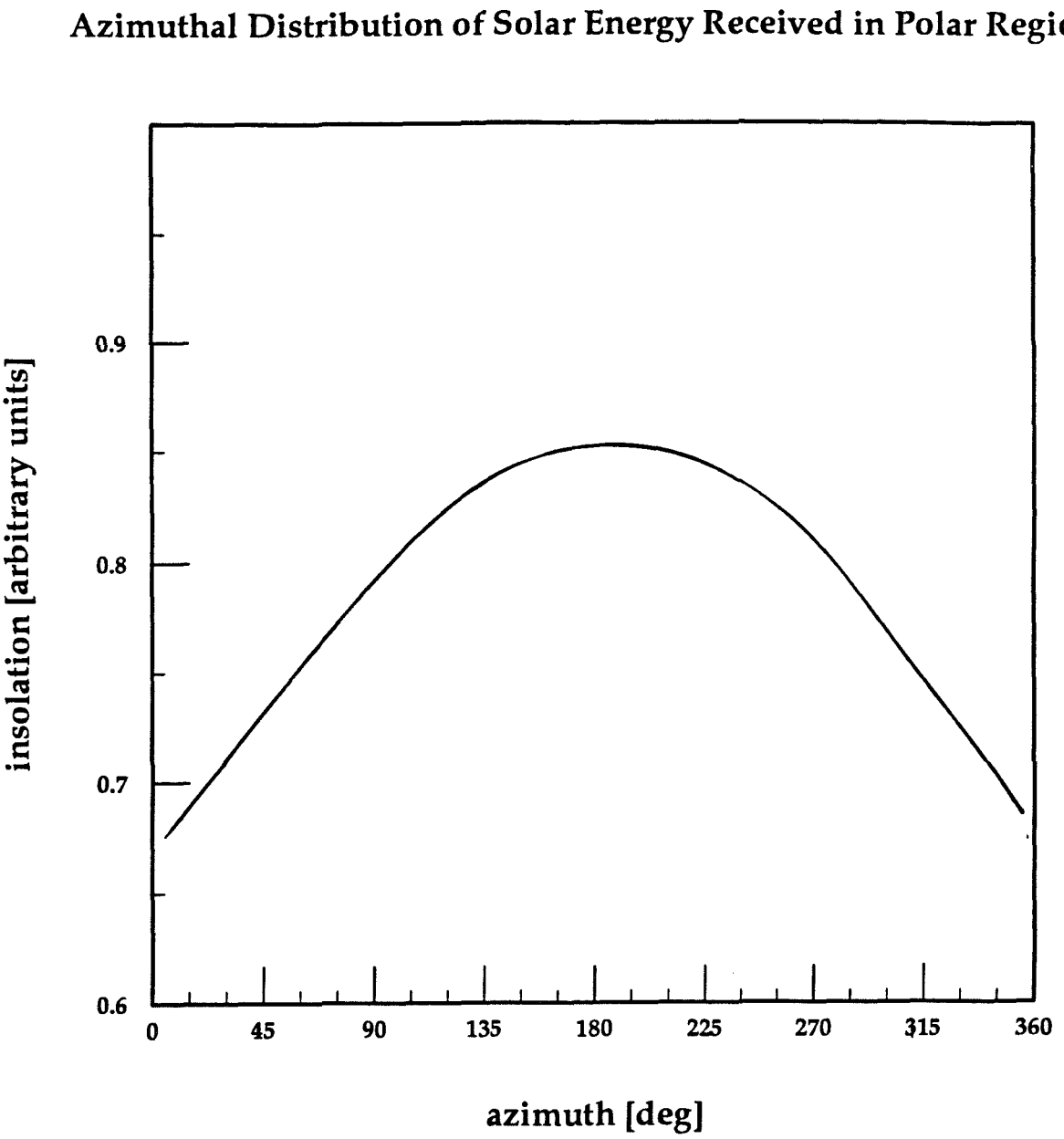

Figure 3.3 Solar energy integrated annually and summed over the Sun elevation. The x–axis is the azimuth, the y–axis is the total solar–energy input coming in the given azimuth and integrated over a) all possible elevations and b) one year.

In addition, the effect of local slopes will prevent the energy input from being uniform for any surface but a completely flat one. A surface with a uniform 5° slope right at the pole will experience illumination equivalent to that at 85° latitude.

And finally, any large–scale structure nearby (mountains, crater wall, etc.) will influence solar input when the Sun is low above the horizon. This happens primarily early in the season. Therefore, such an effect may be critical for any start–up of the development of annual, small–scale structures (for example, in the H_2O residual frost on Mars). Once these structures are formed, even though shallow, then the more uniform solar–energy distribution later in the season enhances the roughness in a direction consistent with the original, non–uniform insolation that is due to the positive feedback of roughness and temperature. (However, this has to be balanced against the fairly rapid sublimation rate of any annual, differential–sublimation features.)

No obvious structures in the Arctic and Antarctica, which would be equivalent to the *penitentes* found in low–to–mid latitudes, have been reported in the literature. There are fundamental differences between terrestrial north and south polar regions regarding the melting and sublimation patterns. Melt–pools are quite common in the north polar region but are very rare in the south. The reason lies in the different set of temperature, relative humidity, altitude, and wind characteristics (Andreas and Ackley, 1982). Sun–cups and related structures are very common in higher altitudes in the Arctic (Greenland), but these are not relevant for our discussion because of the presence of snow melting.

Therefore, the best chance to find relevant analogs is in Antarctica. The primary problem in finding differential–sublimation structures on that continent is

the widespread wind action, which erodes most of the potential surface features. This is why the search for any possible Antarctic *penitentes* has to concentrate on areas of low wind. However, the obvious place — sheltered areas next to the mountains or terrain obstacles is not good, as well, because of the changed solar–insolation patterns. The last constraint for the relevance of terrestrial analogs for Mars is the absence of dust (Antarctic snow, in general, has much higher surface reflectance than Martian frosts — Warren 1982).

Multiple brief references to *penitentes*and differential–sublimation features exist in the Antarctic literature, very often under a different name — e.g., ploughshare ice or ablation grooves (Post and LaChapelle, 1971; Wright and Priestley, 1922; Malin and Zimbelman, 1988). Most of the authors in the glaciological community prefer to use the term *penitentes* strictly for the Andean–type features. The differential–sublimation structures reported in Antarctica fall, in my opinion, into two categories:

- Structures caused by the ice/dust interaction and found primarily nearby the dry valleys or other ice–free areas (Wright and Priestley, 1922). These features are frequently called dust cones (Malin and Zimbleman, 1988). I do not consider these to be true *penitentes* because they do not originate by differential–sublimation triggered by the positive feedback between temperature and roughness.

- Rough ice surface encountered on glacier slopes (e.g., Wright and Priestley, 1922). I am going to discuss these below in relation to my own observations.

3.4 Field observations of differential–sublimation in Antarctica

Because of an opportunity to conduct my own modest field investigation during the 1989/90 summer season in Antarctica, I can contribute new observations. These observations are from the location of the Upstream B camp, which is a summer–only research field camp at 84° south latitude, 105° west longitude and an elevation of 480 m. The environment there is typical for the Antarctic plateau — very flat, light summer winds, summer average temperature about $-10°$ degrees Centigrade, and annual average temperature of $-26°$ degrees Centigrade.

The first and overwhelming observation from this location is that differential–sublimation is an effective process under these conditions: The features formed by differential–sublimation occurred a) on a sloping surface, b) under a clear sky, c) with a light wind ($\leq$ 6 m/s), and d) with no snowfall or blowing snow. The snow surface in such conditions develops the differential–sublimation features within a very few days (see the sequence in Figure 3.4). I will call these features *ablation grooves*.

The important part of my field activity was the measurement of the temperature differential in the ablation grooves. The best data available from this measurement for the diurnal cycle are plotted in Figure 3.5. Other data points were not selected because of the contamination from the presence of clouds or from the blowing snow. Only the data acquired after about 24 hours of clear skies and no significant wind were used ($<$ 7 km/hour). The measurements were performed on the surface which was close to the vertical ($\approx$ 15° angle between the slope and the local vertical direction). The azimuth of the surface was true north–west–north. This is the

Figure 3.4a,b Photographs of the differential–sublimation structures at the Upstream B camp described in the text. Note in a) the wires connecting the thermistors used in the temperature measurement of ablation grooves. The ruler in the picture is for the scale estimate. The b) photograph shows less developed differential–sublimation features on not as steep a surface (about 40° from the vertical). These feature are younger — only about 2 days old.

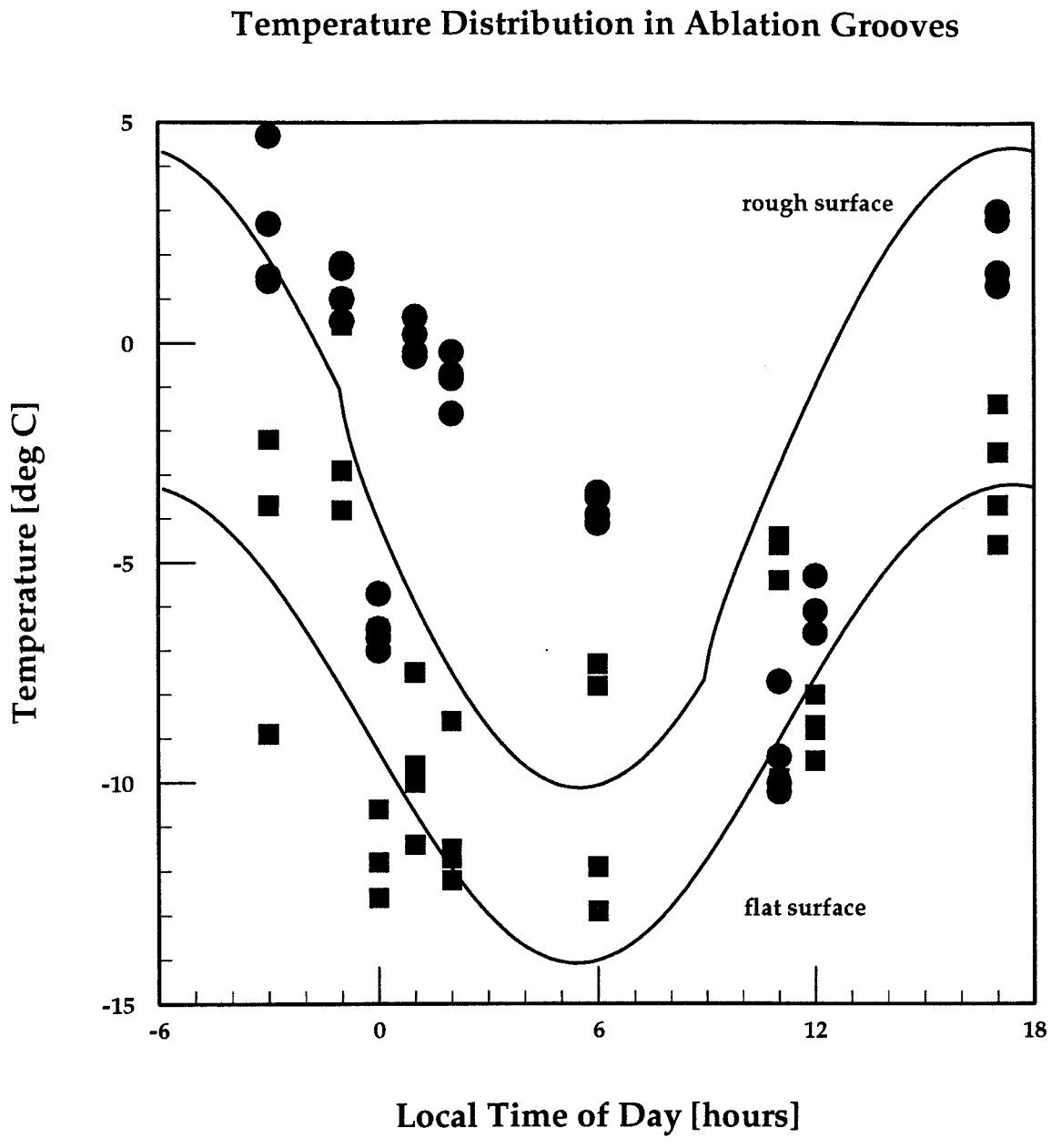

Figure 3.5 Observed temperature measured inside and outside the ablation grooves (circles are temperatures inside the grooves, squares are temperatures outside the grooves).

direction toward the sun in the early afternoon when the temperature was highest. In general, this was the most preferred orientation for differential–sublimation features to occur. At the same time, these differential–sublimation features — ablation grooves — were observed generally in any direction except the one facing the prevailing wind. The ablation grooves were observed to develop on a wide range of surfaces: from a surface sloping 45° (to the vertical direction) to an essentially vertical surface.

The temperatures were measured by eight thermistors (see the connecting wires in Figure 3.4). These temperature–sensing elements consisted of a resistor with strong temperature dependence. The calibration was performed as follows: First, all thermistors were taped together to obtain a close thermal contact, and the assembly was submerged in a mixture of ice and water that was periodically stirred. This eventual equilibrium value of resistivity gave the zero–degree Centigrade reference point. The second reference point was measured by storing the assembly in the snow cave, which was about 3 meters below the snow surface. The temperature in the cave was equal to the annual temperature average of $-26°$ degrees Centigrade (as determined by local, long–term observations). The third point, required for checking the integrity of the calibration, was measured by burying the assembly in the snow, about one foot, and letting the resistivity reach equilibrium. The equlibrium temperature there was about $-12°$ degrees Centigrade. Finally, the calibration data were fitted into this empirical relationship between the thermistor resistivity R and the temperature T:

$$T = \frac{1}{A + B \cdot \log R}. \tag{3.1}$$

Four thermistors (denoted by the circles in Figure 3.5) were located inside the ablation grooves. The other four thermistors (squares in Figure 3.5) were on the outside of the ablation grooves. The peak temperature is not at the 12 o'clock in the graph because true solar time does not coincide with the clock time used at Upstream B (which is the New Zealand daylight–savings time by convention). The y–axis temperature values are for comparison only, because there was a systematic shift (approximately a few degrees) for all thermistors in the measured temperature. This systematic shift was caused by the radiative effects caused by the packaging of the thermistors. Even with the greatest care, it became evident that solar radiation absorption by the white tape enveloping the thermistor caused the increase in temperature. However, I have assumed that at the first approximation, this temperature shift is comparable for all thermistors. I know for certain that the temperature never exceeded the freezing point because there was no evidence of the snow melting anywhere near the experiment area.

The inside temperatures are consistently above the outside temperatures taken at the same time. This is, of course, the result of the positive feedback temperature and roughness discussed in the last chapter. I consider that the temperature/location relationship depicted in Figure 3.5 to be powerful evidence for the postulated mechanism of creating the differential–sublimation features at the polar latitudes.

In order to verify this conclusion, I have used a calculation from the previous chapter (2.36) to compare with the observed temperature (Figure 3.5). Two solid lines in Figure 3.5 show the model diurnal temperature for the flat surface (lower curve) and for the rough surface (upper curve). The opening angle $\gamma = 68° = 90° - 22°$ gave the best fit. The sky temperature was 230 K (Sloan *et al.*, 1955; Bell *et al.*, 1960). The thermal intertia was $60 \cdot 10^{-3}$ in cgs units. The density was 1 g/cm^3.

I have to stress that the structure where the temperature data were taken and all the other pictures of ablation grooves in Figure 3.4 were on the sloped terrain. During the two–month stay at the Upstream B camp, I was not able to observe the formation of any type of differential–sublimation structure on a flat surface. As stated above, the most horizontal surface I have seen with the ablation grooves was sloped 45° to the local, vertical direction. Nevertheless, I believe that this is rather a question of kinematics. There would be *penitentes* forming even on the flat surface, provided there were enough sunny days in a row with light winds and no snowfall. These conditions did not happen for more than a few days (not more than four or five consecutive days) during our entire stay at the Upstream B camp.

But even during those few days, the formation of a hoar frost was very evident. The hoar frost consists of large, single crystals formed by vapor sublimation and redeposition. This is a clear sign that some kind of feedback between temperature and roughness is acting at these conditions.

The formation of hoar frost is a result of the metamorphosis of dry snow (Colbeck 1983; Adams and Brown 1983). Snowfall quickly develops a much coarser grain structure within a few days after its deposition. Only about one in $10^4 - 10^5$ grains survives and grows at the expense of others. This creates *firn* snow and the so–called "depth–hoar" frost. Such a metamorphosis is driven by the vertical temperature gradient across the subsurface layer of snow. This temperature gradient is almost always present in the surface, which has a finite thermal inertia. The solid–state greenhouse effect, to the extent that it is present in the snow/ice surface, can also contribute to the vertical–temperature gradient (Adams and Brown, 1983). The temperature gradient creates the vapor pressure gradient, which drives the mass flow from warmer to colder frost — from "hot spots" to "cold traps." In the terrestrial

environment, these inhomogeneities control the mass flow rather than the average temperature gradient. The large grains grow faster because they protrude farther away and conduct heat much more effectively than air. This creates a thermal short–circuit and compresses the temperature gradient in a much shorter, intergranular space. Eventually, the grains become large enough for positive feedback between temperature and roughness, desribed in the previous chapter, to occur. This was observed to occur at our Antarctica site, with the length–scale of few mm and a time–scale of less than 24 hours.

Therefore, I suggest this conclusion on the basis of my field observation: In spite of my best effort, I could find neither in the literature nor in the field a clear convincing example of an idealized, differential–sublimation structure like *penitentes* at the polar regions. This structure would have to satisfy these requirements: 1) existence in pure snow, 2) on a flat surface, 3) and with an even horizon. But I did find abundant evidence for the differential–sublimation process happening very quickly in an environment of non–uniform, solar insolation — for example, slopes. Because of that, and considering the fast kinetics described in the previous paragraph, I feel confident that such differential–sublimation structures would exist even on a flat slope in the polar regions, given enough time under favorable conditions, such as on Mars. The reason that such features are not easily observed on Earth is that there are only rarely enough clear–sky days with the light wind in Antarctica. As well, an exhaustive search for such features on that continent is yet to be conducted.

To summarize in one sentence: There is not a specific, terrestrial analog for the *penitentes* on Mars. But there is plentiful evidence for the the existence of polar differential–sublimation that is due to non–uniform solar insolation, thus creating small–scale roughness.

3.5 Proposed observational tests

The subject of this section is the potential verification of postulated differential–sublimation features by upcoming missions — Mars Observer, Mars'94, possible Mars'96 and others. There are four classes of observations (in visible, thermal infrared, and radio wavelengths, and *in situ*), which are described in the following paragraphs. I am discussing observation of differential–sublimation features in both H_2O and CO_2 frost even if I did not consider formation of differential–sublimation features in CO_2 frost in this thesis.

In principle, these differential–sublimation features in the Martian seasonal and residual polar frost may be directly imaged from the orbiting spacecraft. That would be the most convincing argument. However, I expect such direct observations by the Mars Observer Camera to be only marginally possible, given the terrestrial analogy for the scale of these features.

The more probable verification of the existence of differential–sublimation features is by indirect observations. There are several possibilities. In the first place, one can utilize the property found in the terrestrial *penitentes*, which typically line up along the direction of the ground trace of the diurnal motion of the Sun or more specifically along the direction of the maximum insolation. This is typically east–west, but it may be modified by the presence of the large–scale topography. This property is true even for the polar regions (my own observations in Antarctica and Wright and Priestley 1922). The ideal geometry for such measurement would be from a polar orbiting spacecraft with the noon local time of the equator crossing. One should find asymmetry in the phase integral measured in a) the orbital plane (along–track)

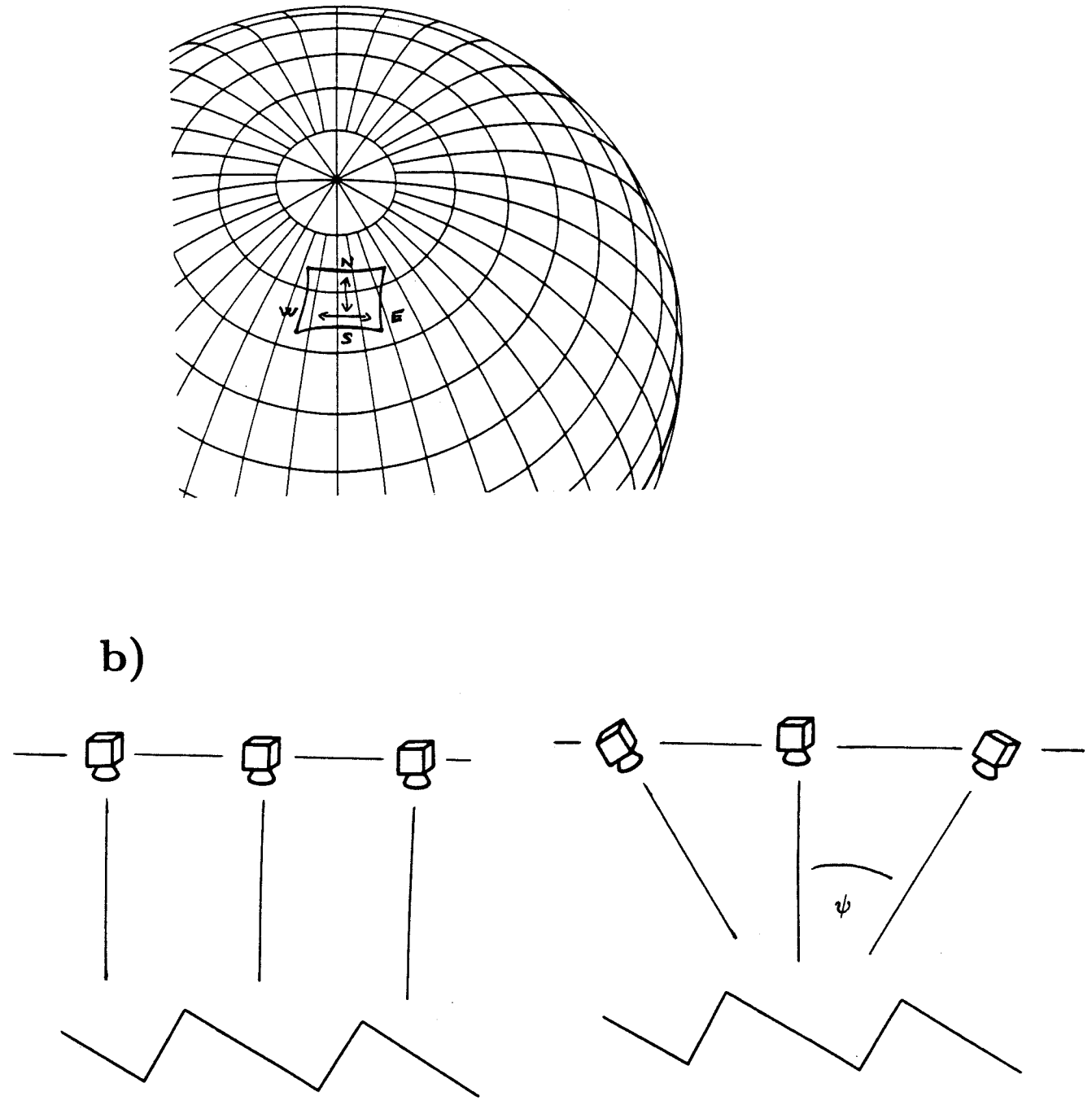

Figure 3.9a,b The viewing geometry of the differential–sublimation features in the polar frost for a polar–orbiting spacecraft like Mars Observer. In Figure 3.9b, the direction towards the equator is to the left; the poleward direction is to the right. The emission angle ψ is used in Figure 3.10 and Figure 3.11.

and b) the plane normal to the orbital plane (cross–track). Approximately, these two planes correspond to the local north–south and east–west directions on the surface (Figure 3.9a).

The roughness/temperature feedback acts primarily normal to the ground trace of maximum insolation (approximately east–west). Therefore, the surface would be relatively smooth in this direction — we are observing along the longitudinal axis of the saw–tooth pattern shown in Figure 3.9. This is reflected by labeling the symmetrical distribution of radiance in Figure 3.10 as "smooth (east–west)." For the completely smooth frost surface, the radiance dependence on the viewing geometry would be symmetrical around the azimuth of the subsatellite point.

For the rough–frost surface, the peak in surface reflectance will shift towards lower phase angles, closer to the incidence direction of sunlight. This is in the left direction in Figure 3.9b. The radiance profile would be more steep, less Lambertian, as is shown by the curve with the label "rough (north–south)."

In fact, for the completely Lambertian surface, there would be no dependence of radiance on the emission angle. For the Lambertian surface, the reflectance drops off as $\cos\theta$, but the geometry factor (provided a target fills the field of view of the instrument) goes as $1/\cos\theta$, and these two factors cancel each other.

Second, the relationship between surface reflectivity and brightness temperature may also reveal the presence of differential–sublimation features. This is depicted in Figure 3.11. There is an obvious and general relationship between the effective albedo and the surface temperature — negative correlation. This relationship is depicted as "T(typical)" in Figure 3.11. For the rough surface, this relationship

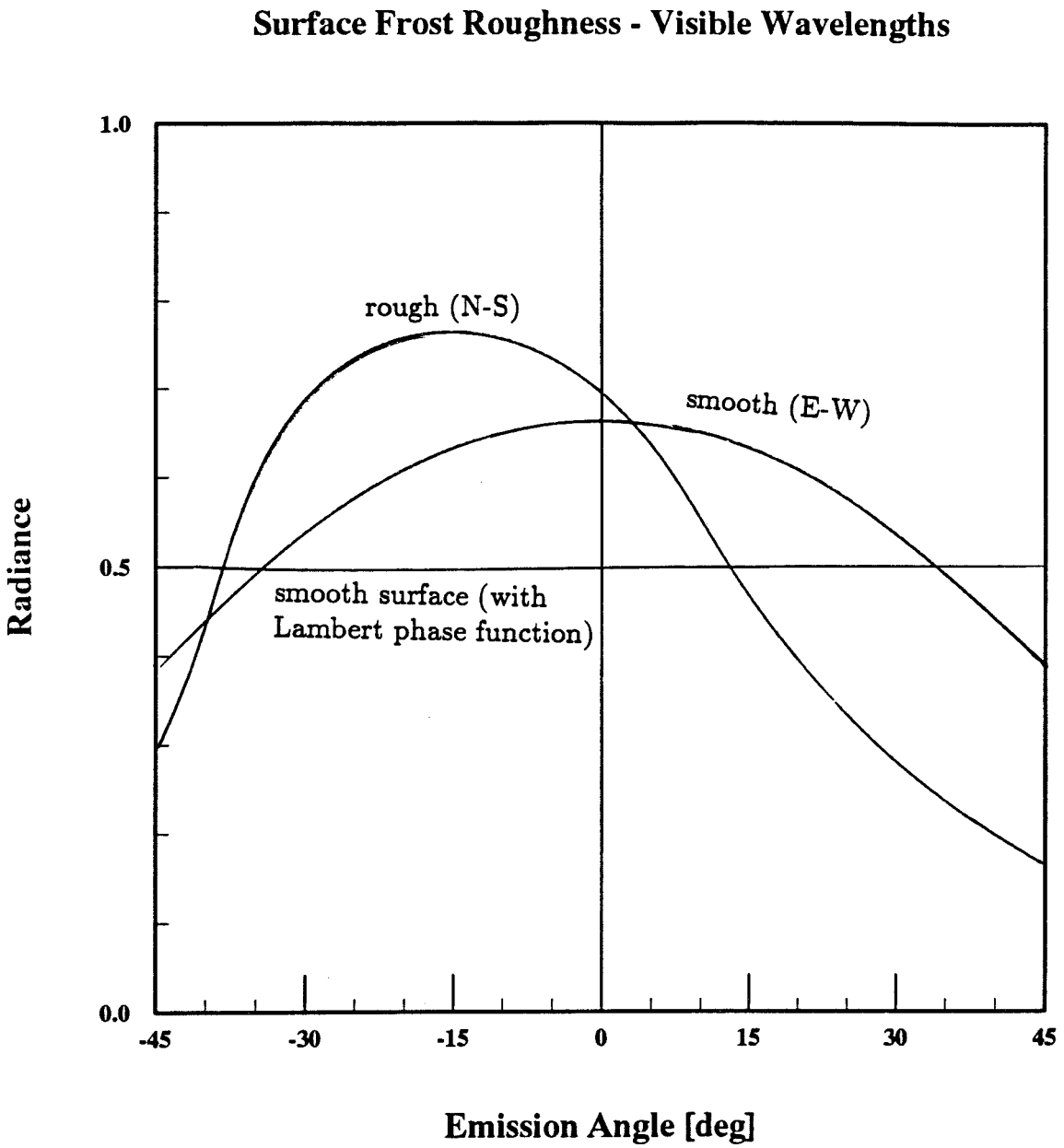

Figure 3.10 Suggested signature of rough polar frost at visible wavelengths. The x–axis is the emission angle ψ from Figure 3.9b (right side). The y–axis is the radiance at the remote–sensing instrument in arbitrary units.

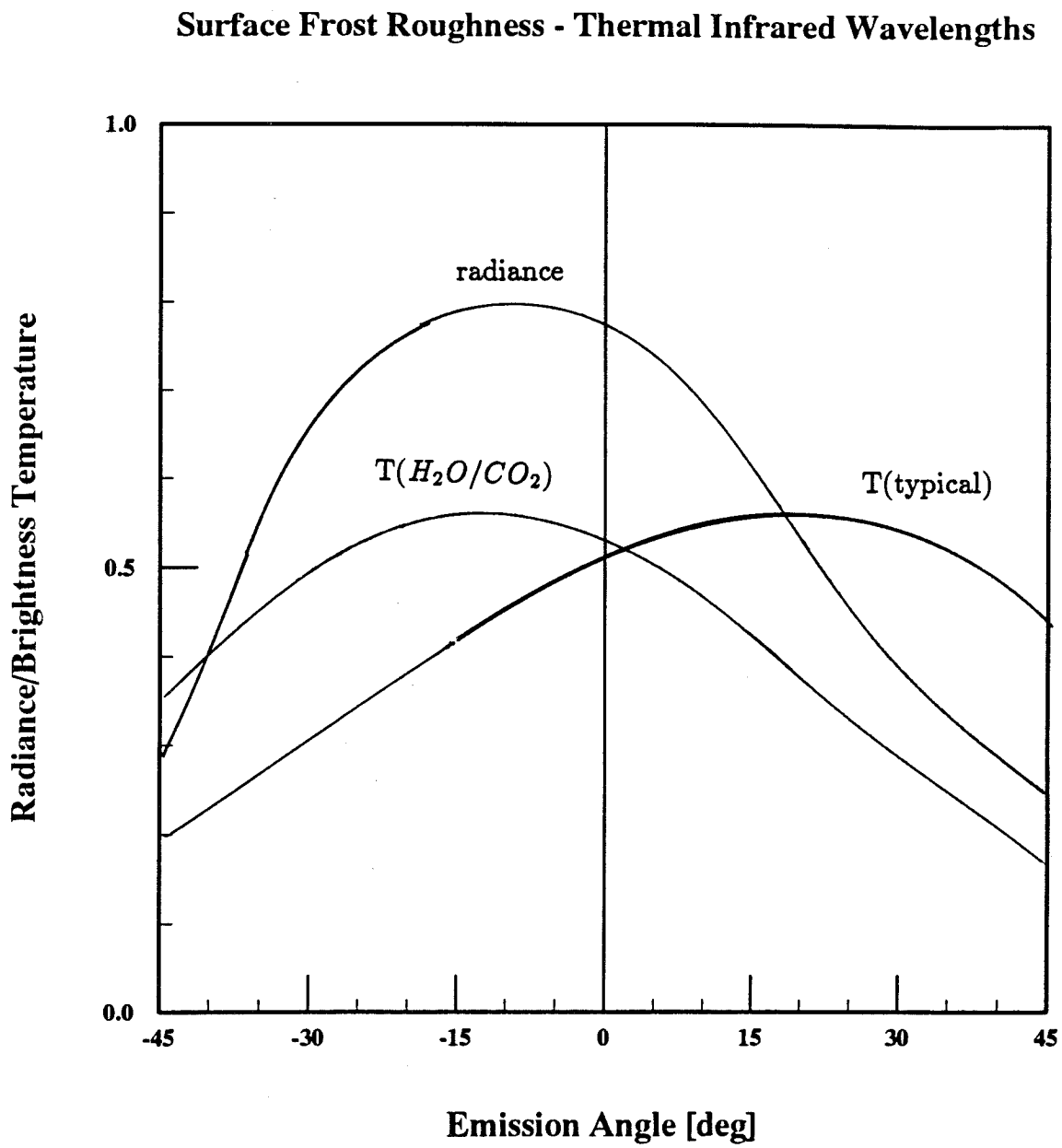

Figure 3.11 Suggested signature of rough polar frost at thermal infrared wavelengths and its relationship to visible signature. The x–axis is the emission angle ψ from Figure 3.9b (right side). The y–axis is the visible radiance and brightness temperature measured by the remote–sensing instrument in arbitrary units.

could vary with the viewing geometry. For example, it was suggested that the differential–sublimation features play a critical role in shielding the CO_2 residual frost from direct sunlight at the southern polar frost (Paige *et al.*, 1990).

There may be CO_2 frost "hiding" along the longer (less–illuminated) side of the saw–tooth pattern in Figure 3.9. In that case, this cold frost may not be visible (for brightness temperature measurements) for the observation geometry near the zero–phase angle when more illuminated surface (which is predominantly H_2O ice) fills the field–of–view of the instrument (that is, of course, the whole idea of hiding the CO_2 frost). This concept assumes non–uniform temperature distribution across differential–sublimation features. As we move to larger phase angles, and increase the emission angle (moving right in Figure 3.9b), we see less radiance in visible wavelengths (because of more multiple scattering, Figure 3.10), but also smaller brightness temperatures.

Therefore, in this situation we measure a completely reversed relationship between surface reflectance and brightness temperature for the rough surface consisting of the H_2O and CO_2 mixture than we would for a similar smooth surface. The coupled measurements, using visible and thermal infrared imaging systems would be required to verify this hypothesis.

Unfortunately for both examples shown in Figures 3.10 and 3.11, the Mars Observer Camera (MOC) utilizes a pushbroom technique for surface imaging (the left side of Figure 3.9b), and the surface emission angle is constant. One therefore must look for second–order effects to ascertain the presence of differential–sublimation features in the polar frost. Any such measurement is inherently difficult because of the separating effects of i) large–scale topography, ii) small–scale roughness, and iii)

surface–material properties, on the phase function observations. In the ideal case, the direct measurement of bidirectional reflectance–distribution function (BRDF) would be the most useful (the right side of Figure 3.9b). Thermal Emission Spectrometer (TES) may be able to provide some of this information because of its multiple viewing–angle capability. This is similar to the terrestrial measurement by the Multi–Angle Imaging Spectro–Radiometer (MISR) built by JPL for EOS. Or at least, the frame–type camera (similar to Viking or Voyager) would be useful for retrieving the phase function of the polar frost surface. Neverthless, for this experiment, a Mars'94 thermal–mapping radiometer (Termoskan II) with the variable viewing geometry might also be suitable. In any case, TES has an important role in identifying the surface composition of southern residual frost.

Third: Fortunately, the Sun–synchronized orbit of the Mars Observer and the fixed nadir pointing combined with the Mars Observer Camera Medium Resolution mode provides an ideal vehicle for studying the seasonal evolution of the polar–frost surface reflectance. This measurement could have not be done with the previous spacecraft, as those were not in polar orbit. At the same time, the more variable Mars'94 orbit may be better for the complementary phase function observations with varying illumination geometry. The lower resolution of Mars'94 cameras should not constitute any difficulty for this observation.

The development of differential–sublimation features will cause the surface reflectance of seasonal frost to increase rapidly with time shortly after insolation first reaches the frost. This effect should be observable with repeated imaging by MOC. The difficult task is in separating the effect of changes in properties of frost surface (for example, Paige 1985; Keiffer 1990) from the effect of small–scale roughness.

A very important property of these postulated, polar–frost features could be strong backscattering of a radio signal at wavelengths comparable to the suggested scale of differential–sublimation features. There are some hints that this was already observed by ground observations (Muhleman *et al.*, 1991). However, I feel that this is a rather premature interpretation and I prefer to wait for observations with a better spatial resolution from orbiting spacecraft. There are also alternative explanations for this observation (Hapke 1990). Another possible confirmation is randomization of the signal polarization because of multiple scattering from the rough–surface elements. Unfortunately, there will be only a limited radio–science capability on the Mars Observer and Mars'94.

Ideally, hypothesized, differential–sublimation structures would be confirmed by direct visual observations on the surface. The only near–term candidates appear to be the Mars Balloon of the Mars'96 mission (Linkin *et al.*, 1989). There is a slight chance of a Mars Balloon travelling through the northern residual frost on the basis of preliminary plans. Some of the proposed future U.S. hard landers or penetrators could land at a high latitude and so perform a similar function. It does not seem to be feasible for a rover (large or mini) to land at a latitude high enough during the upcoming decade of Mars exploration. However, depending on the final outcome, a possible follow–up Mars Observer mission could have improved the imaging resolution so that direct observation of differential–sublimation features would be possible even from the orbit.

3.6 Conclusions

There is a natural tendency of the volatile surface to develop spontaneously small–scale roughness in a sublimation dominated environment: This behavior

- can be plausibly predicted from "first principles,"
- is difficult to model exactly,
- is observed to occur on the Earth,
- may be tested by the Mars Observer,
- has important implications for future studies of H_2O (and possibly CO_2) frost on Mars.

I have shown that this effect is found extensively on the Earth at low latitudes and to a smaller extent, at the polar regions. Quite different surface morphologies can result, depending on the initial and ambient conditions. It is not possible to predict a detailed morphology of Martian differential–sublimation features with any reasonable degree of confidence. Also, this phenomenon occurs on the surfaces of pure ice as well as of ice/dust mixtures. I have attempted in this chapter to demonstrate that Martian polar frost is an environment conducive to formation of these features. This is based on theoretical considerations and terrestrial analogs.

I conclude that there is a high probability of substantial surface roughness being present on the Martian H_2O northern residual polar frost. I have not addressed the south residual frost in any substantial depth. The morphology and properties of the frost surface will thus drastically change. This will significantly alter the apparent

Bond albedo and brightness temperature of that surface. Future observational tests have been suggested considering specific instruments that will be flown in the Mars orbit in the near future. Finally, I wish to note that the arguments above could also be applied to other bodies in the solar system besides Martian polar frost. This leads me to a suggestion that the tendency of a volatile surface to develop small–scale roughness is relevant to small satellites, comets, and other bodies in the solar system, as well.

Chapter 4

Role of boundary layer in water vapor exchange between surface and atmosphere at VL-2 site

A key question in the study of Mars is the water exchange between the atmosphere and the surface on daily, seasonal and astronomical timescales (Jakosky 1985). The data from the Mariner 9 and Viking spacecraft present convincing evidence that substantial amounts of water modified the surface of Mars in the past (Carr 1986). However, at present, observable water exchange is limited to the dynamic behavior of the polar caps (Leighton and Murray, 1966, Jones 1979) and to occasional frosts, fogs and clouds (Christensen and Zurek, 1984).

As stated in the introduction, I believe that the small scale processes are a key to enhanced understanding of the global water behavior of Mars. The principal data for this part of my study of small scale properties of the Martian surface were collected predominantly by the second Viking Lander (VL-2) (with its more poleward location) and by both Viking Orbiters. The annual deposition and retreat of the frost layer were observed in-situ by VL-2. At the time of the Viking project, it was concluded that this frost represented the southernmost edge of the northern seasonal polar cap (Snyder 1979). However, the question of the composition (H_2O

or CO_2 ice) has persisted (Guiness *et al.*, 1979, Jones *et al.*, 1979) and is addressed here. This chapter is derived from Svitek and Murray, 1990.

The frost is inferred to be H_2O frost but with some properties suggesting a much thicker layer than would be expected from the simple mass balance calculation. My original contribution is in considering the effect of the cold-trapping (frost redeposition) which has been previously neglected and which enables the reconcilation of all the observations with environmental conditions. In addition, I believe that this study points to a more general phenomenon of the cold-trapping in the Martian environment.

4.1 Problem

In 1981, Wall published a study of the optical properties of the Viking Lander 2 frost. He showed that the measured phase function is consistent with a thickness of the frost layer on the order of several hundred micrometers. There is not enough water vapor for such a thick layer of H_2O frost to form simply by condensation from the Martian atmosphere (Davies *et al.*, 1977). Therefore, Wall argued that this phase function interpretation indicated a CO_2 , not a H_2O frost composition. Furthermore, there was an increase of only a few precipitable micrometers (at most) in the water vapor content of the atmosphere as frost disappeared in late winter.

Later, Hart and Jakosky (1986) presented heat balance calculations. They concluded that their calculation precludes formation of CO_2 ice at this latitude and season, and therefore argued instead for H_2O ice as the Viking Lander 2 winter

frost. However, this very important and critical conclusion has to be reconciled with the result of the Wall study. Hart and Jakosky (1986) suggested that frost photometric properties can be consistent with 10 μm of H_2O frost.

I believe that there are two problems with this interpretation. First, the 5 per cent increase in surface reflectance in visible wavelengths (quoted by Hart and Jakosky, 1986) is smaller by about a factor of ten as compared with the reflectance increase which I measured. The increase in surface reflectance measured by VL-2 cameras requires frost thickness much larger than 10 μm. Second, Hart and Jakosky (1986) suggested that deviations from Lambertian behavior in Wall (1981) could be explained by a much thinner layer than Wall proposed. But a comparison with the original laboratory data in Smith *et al.* (1969) shows that these deviations from Lambertian reflectance are far too small to allow a possibility of 10 μm frost layer.

These contradicting conclusions from Wall (1981) and Hart and Jakosky (1986) was intriguing, and I undertook the work reported here. The conclusion of the study reported in this chapter is twofold: Firstly, all the winter VL-2 frost was H_2O ice but existing in two distinct phases. Secondly, the second-phase was concentrated from the first-phase frost by cold-trapping due to local roughness at the VL-2 site (and probably on much larger scale as well). This first conclusion (H_2O ice composition) follows closely the previous result of Hart and Jakosky (1986). My original contribution extending the previous work of Hart and Jakosky (1986) is this: First, I have considered in-depth the photometric data obtained by an VL-2 imaging experiment and have been able to reconcile those with the calculation of thermodynamic stability of VL-2 frost. Second, I have developed a more detailed model of the water vapor transport in the boundary layer on Mars during the frost sublimation and redeposition. This model is an enhancement of a simpler model of Ingersoll (1970)

and (1974) and Toon *et al.* (1980) derived from terrestrial approaches. This model produces as its consequence the cold-trapping (frost redeposition) mechanism which has been previously neglected and which enables us to reconcile the "thick layer" results of Wall (1981) with the thermodynamic analysis of Hart and Jakosky (1986). My analysis of VL-2 frost is sufficiently complete to lead me to argue that some form of the cold-trapping must be a common attribute of the Martian environment in general.

My study of the VL-2 observations suggests that H_2O frost occurs in two forms:

- thin, almost continuous, early frost (Figure 4.2), and
- much thicker, patchy, later frost (Figure 4.3).

Both frost forms contain essentially the same total water content (averaged over large area) but they cover different fractions of the surface. The transition between two frost forms occurs by recondensation at local cold traps when solar insolation sublimates the first frost, but the atmosphere is still too cold to transport the resultant water vapor away. These lower-than-average-temperature cold traps are created by shadowing from the small scale surface roughness — rocks, troughs, etc.

This hypothesis hinges on the disparity between the capability for local and long-range transport of water vapor by the atmosphere. The short-range ($10^0 - 10^4$ m) transport is driven by the abundant solar energy available at the time of transition. This results in a large fraction of surface frost being moved rapidly into local thermodynamically preferable locations — cold traps. Long range transport is constrained by the atmospheric carrying capacity. At the time of the VL-2 frost transition, the atmosphere was still cold, not far from its winter minimum, and was

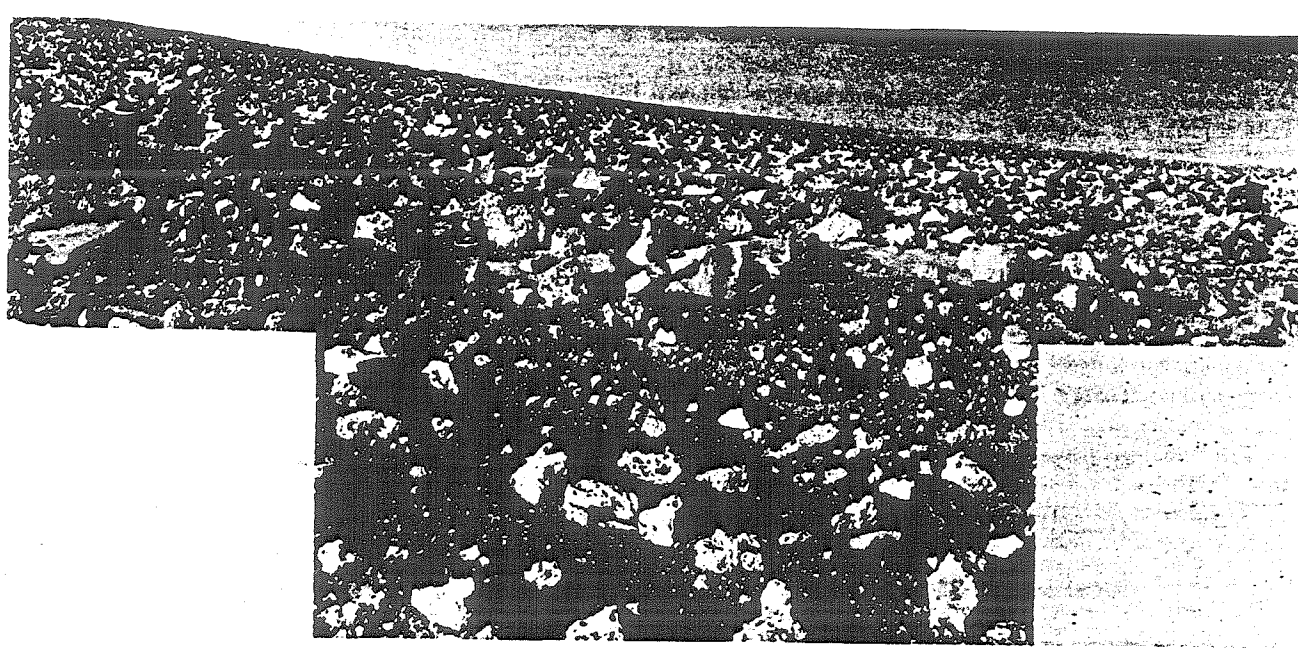

Figure 4.1 VL-2 panorama

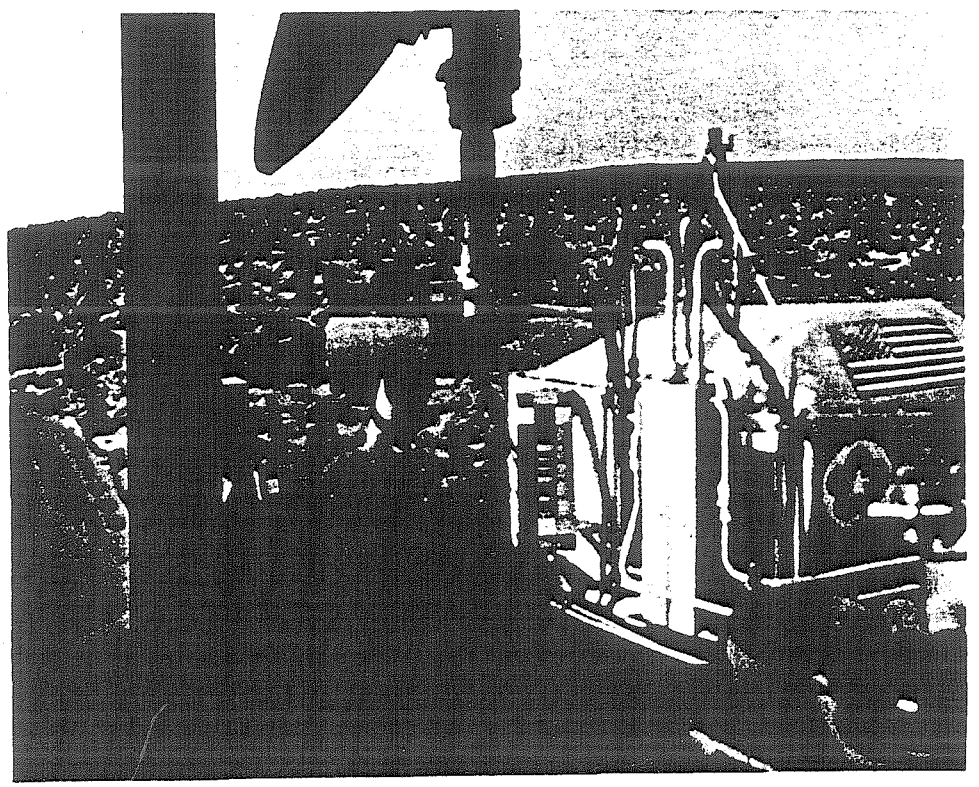

Figure 4.2 Early continuous frost

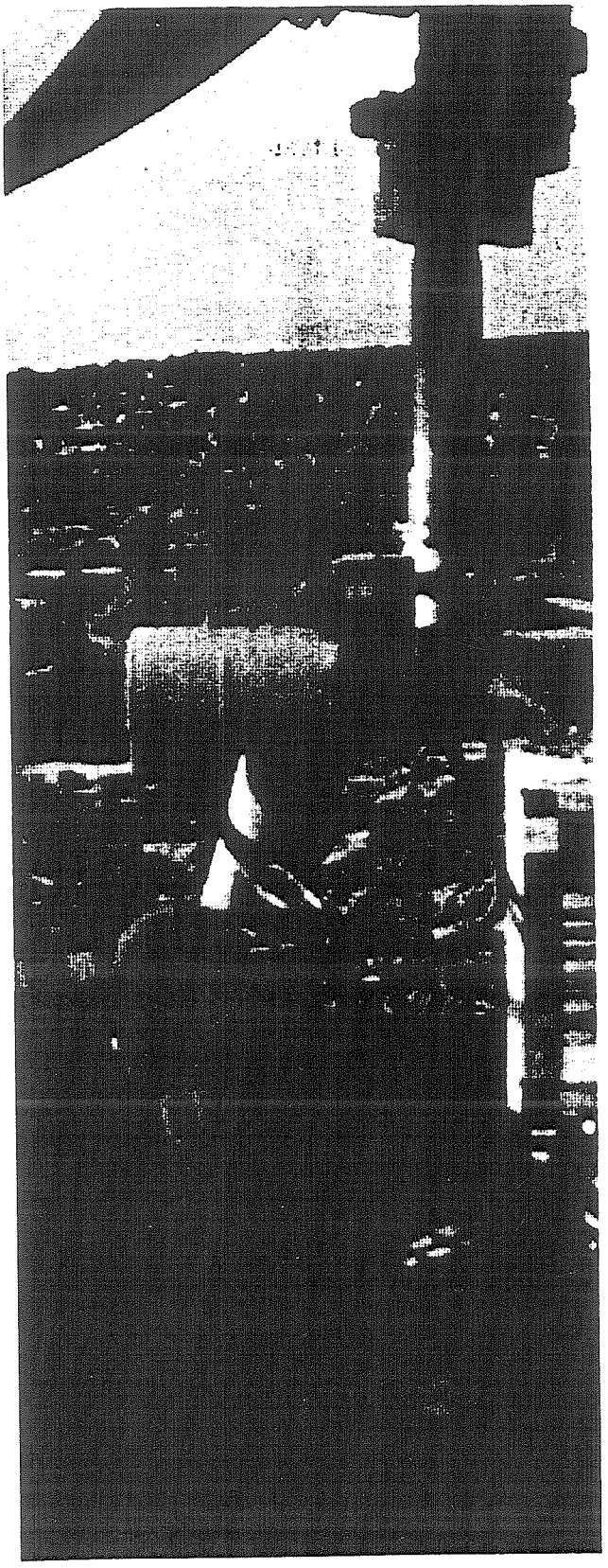

Figure 4.3 Later patchy frost

almost saturated by residual water vapor (5 to 8 precipitable microns). Therefore, it cannot have carried much additional water vapor to lower latitudes. This disparity delayed the global transport of water vapor by the atmosphere.

In the next section of this chapter, I will present the environmental setting of the observational platform — Viking Lander 2 — and summarize the data useed in our study. In the third, fourth, and fifth sections of this chapter, I describe the proposed concept of the frost cold-trapping and the physical processes operating at the VL-2 site. The following section presents the quantitative tests to which I subjected my hypothesis. Finally, I will discuss extensions of the concept to other situations as well as its limitations and also delineate possible tests using future data.

4.2 Environmental setting

The Viking Lander 2 landed on September 3, 1976, at Utopia Planitia, 47.96° N and 225.77° W. The landing site is on the ejecta debris blanket of the Mie crater located about 200 km to the southwest. The lander sits on a boulder field, with fine dust and sand as substrate and with no clearly visible bedrock. The panoramic view from VL-2 northward is in Figure 4.1. Besides the top priority search for life, the landers conducted a series of meteorological and soil properties experiments. This section describes data which were used in this study.

4.2.1 Frost surface coverage and color

Two facsimile cameras on top of the lander body took almost 3000 images during the lifetime of VL-2 (Guiness *et al.*, 1982, Arvidson *et al.*, 1983). About 600 of these were taken during the first and second winter and reveal the traces of the frost (Figures 4.2 and 4.3). I used a selected fraction of these images (Table 4.1) for measurement of the changes in frost surface coverage and color as a function of L_S. The surface coverage measurement was performed by visually inspecting the images and using a grid overlay to estimate the frost covered fraction of the surface.

The color changes were measured by extracting pixel values (DN — Data Numbers) from the identified frost spots on the surface (Figure 4.4). This was made possible by a sequence of images of the same area taken in color triplets (through red, green and blue filters), usually with the calibration target in the image, and at the same local time (Table 4.2). This sequence was taken during both winters and the measurement was repeated for both. The color change was measured by comparing DN values of frost, calibration target, lander cover, and bare soil in three color bands (red, green and blue). Only relative color change (comparing different areas of frost) is required for the sake of the argument in this study. Absolute color information is difficult to obtain because of uncertain calibration of cameras and the poorly quantified effect of atmospheric scattering. For my analysis, the relative color change is important only at the time of transition between two frost forms.

Measurement of the frost brightness and color as a function of phase angle could yield further clues about the Martian soil roughness and frost deposition mode on the surface. However, as these are not directly relevant to this topic, they are not pursued further here.

CE Label	Sol	L_S [deg]	Cover [%]	Uncertainty [%]
22D180	233	251	75	25
22D181	233	251	85	10
21D198	245	259	70	15
22D209	245	259	60	20
22D213	245	259	85	10
22D220	257	266	70	20
21D224	257	266	75	10
21D232	257	266	75	10
22D249	269	274	70	15
22D253	269	274	85	10
21E008	281	282	85	10
21E016	281	282	90	5
22E033	293	289	90	5
22E037	293	289	85	20
21E048	305	297	85	10
21E056	305	297	92	5
22E073	317	304	65	25
22E077	317	304	65	25
22E085	329	311	40	20
22E088	329	311	50	30
22E128	353	325	25	10
21E153	365	332	20	10
22E169	377	338	15	5
21E187	382	341	20	5
21E192	382	341	25	5
21E194	382	341	15	5
22E211	389	345	5	3
21E215	389	345	10	3
22E230	400	351	3	1
22E247	406	354	3	1
22F011	410	356	2	1
21D184	233	251	85	10
21D186	233	251	75	20
21D192	233	251	70	15
21D193	233	251	75	20
22D199	245	258	50	20
22D203	245	258	40	20
22D227	257	266	40	10
22D231	257	266	30	10
21D233	257	266	60	15
22E035	293	289	70	25
22E038	293	289	75	25
22E039	293	289	80	15
21E040	293	289	80	10
22E045	305	297	85	10
21E048	305	297	85	10
21E049	305	297	85	10
21E050	305	297	90	5

Table 4.1 List of VL-2 images used to study surface coverage of frost and results

22E051	305	297	70	10
21E052	305	297	80	15
21E054	305	297	60	25
22E055	305	297	80	5
21E057	305	297	85	5
21E058	305	297	85	5
21E059	305	297	80	10
22E071	317	304	75	15
22E075	317	304	70	20
22E078	317	304	60	20
22E085	329	311	70	25
22E088	329	311	40	30
22E091	329	311	50	15
22E092	329	311	60	20
21E094	329	311	60	15
22E095	329	311	80	5
22E098	329	311	50	25
21E099	329	311	75	5
22E111	341	318	85	10
21E113	341	318	80	5
21E114	341	318	80	15
21E117	341	318	65	15
21E119	341	318	80	15
22E128	353	325	25	5
22E129	353	325	25	10
22E136	353	325	10	5
21E153	365	332	25	10
22E169	377	339	15	5
21E227	398	350	3	2
22E230	400	351	3	2
22I057	874	233	40	30
22I058	886	241	40	30
22I059	898	249	50	20
22I060	910	256	70	15
22I061	922	264	85	10
22I062	934	272	85	10
22I063	946	280	85	10
22I066	955	285	85	10
22I067	955	285	80	15
22I075	955	285	85	10
21I093	960	289	85	10
22I096	967	293	75	10
22I097	977	299	75	10
22I098	987	305	75	10
22I099	997	311	70	10
22I100	1000	317	60	10
22I101	1001	323	60	15
22I102	1002	329	55	10
21I105	1003	334	20	5
22I065	955	285	60	30
21I090	959	288	80	30
21I091	959	288	65	15
22I094	960	289	70	20

Table 4.1 Cont.

CE label	L_S [deg]	Sol	White	Red	Late frost	Early frost
22I057	233	874	.9	2.7		1.8
22I058	241	886	1.0	3.2		1.9
22I059	249	898	1.0	3.1		1.6
22I060	256	910	.9	3.0	.9	1.3
22I061	264	922	.8		.9	1.1
22I062	272	934	.9	3.0	.9	1.0
22I063	280	946	.9	2.9	.8	1.0
22I066	285	955	.8	2.8	.8	.9
22I067	285	955	.8	2.8		.8
22I096	293	967	.8	2.9	1.0	1.0
22I097	299	977	.8	2.8	1.0	1.0
22I098	305	987	.8	2.8	1.0	1.0
22I099	311	997	.8	3.1	1.0	1.1
22I100	317	1007	1.0	3.0	1.0	1.1
22I101	323	1017	.8	3.2	.5	1.5
22I102	329	1027	.8	3.2	.6	1.6

Table 4.2 List of VL-2 images used to study color changes of frost and results

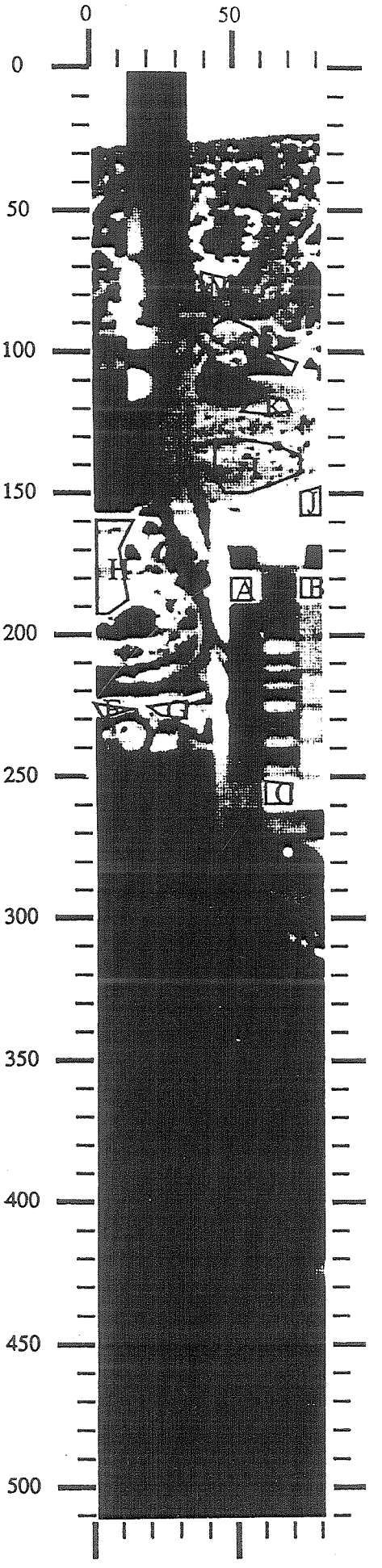

Figure 4.4 Example of pixel retrieval processe

4.2.2 Atmospheric temperature

Temperature is a key parameter in any study of volatiles. The primary use of temperature data in my study was to calculate the atmospheric holding capacity for water vapor. The first source of atmospheric temperature data was the Lander itself (Hess *et al.*, 1977). The ambient temperature sensor was included as a part of the more comprehensive meteorological package and was measured at a height of about 1.5 meter. A second source was the Viking Orbiter infrared radiometer (IRTM) with its 15 μm band which provided an atmospheric temperature with the weighting function peaking at about 25 km (Kieffer *et al.*, 1977). This is about the maximum altitude where water vapor can make a noticeable contribution to the total atmospheric column under most of conditions. The possible exception is a temperature inversion which can happen under either one of two conditions: 1) a vigorous dust storm, or 2) surface covered by CO_2 frost. Under these conditions, most of the water vapor can be stored at higher altitudes ($\approx$ 25 km) because of higher temperatures there. However, the season of my study was after the global dust storm when there was no permanent CO_2 frost deposit on the surface, and the large-scale thermal inversion at this latitude and season is not supported by VL-2 and IRTM data (the temperature of the IRTM 15 μm band is consistently lower than the temperature at the VL-2 site).

The synthesized vertical temperature distribution of the atmosphere and its diurnal variation above the VL-2 site is depicted in Figure 4.5. It is based upon the following expressions:

$$T(z) = T_{st}(z) + \Delta T \exp(-z/z_0), \tag{4.1}$$

$$T_{st}(z) = T_{VL} + (T_{25} - T_{VL}) \cdot z/25, \tag{4.2}$$

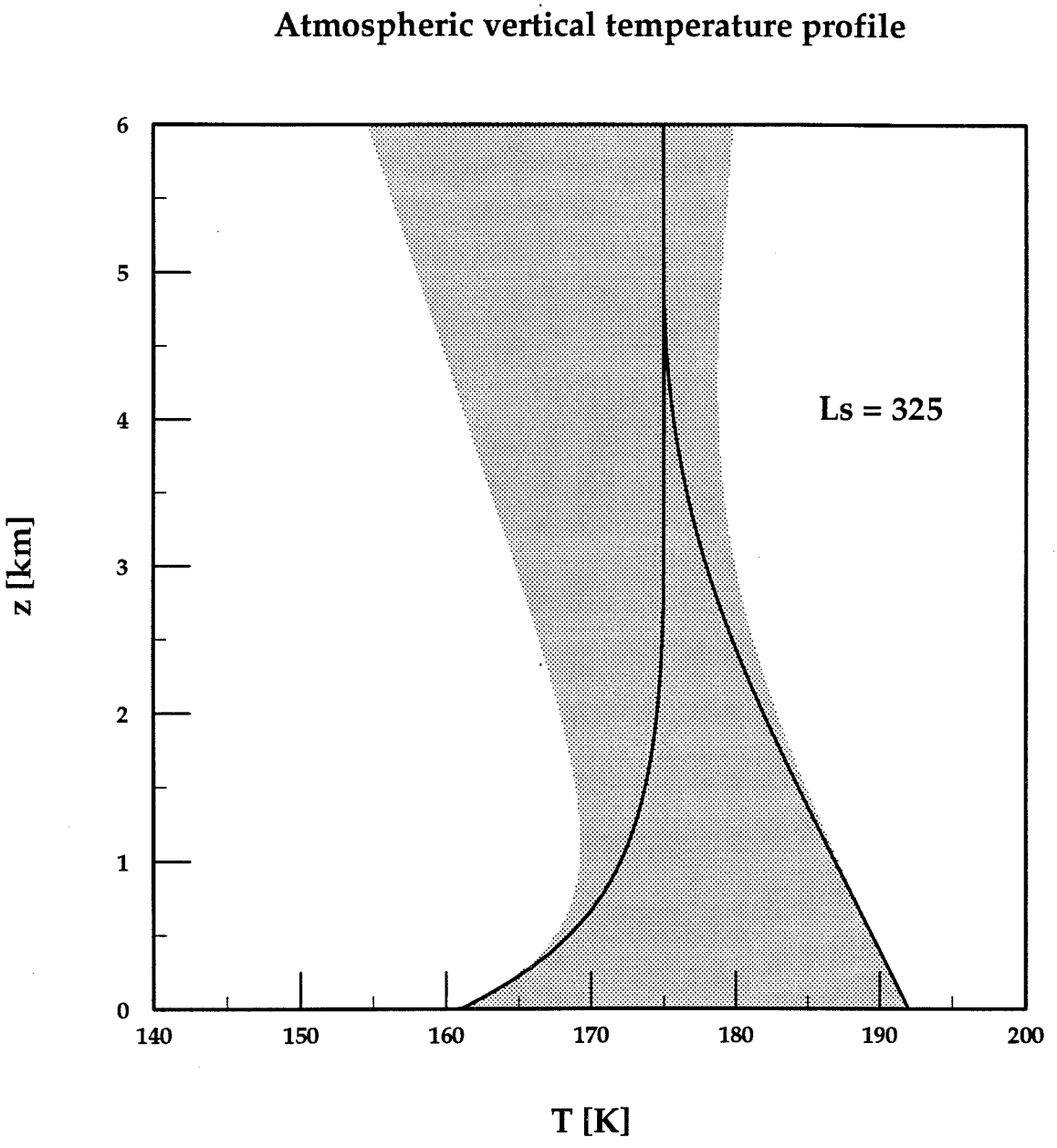

Figure 4.5 Synthesized atmospheric vertical temperature profile and diurnal variation in thermal boundary layer.

$$\Delta T = (T_{VL_{max}} - T_{VL_{min}})/2. \tag{4.3}$$

where $T(z)$ is the atmospheric temperature, z is the altitude (in km), T_st is the steady temperature (without diurnal variation), ΔT is the diurnal excursion from the steady state in the thermal boundary layer, T_{VL} is the ambient temperature at the Viking Lander site, T_{25} is the temperature at roughly 25 km altitude measured by the IRTM instrument at 15 μm band, and z_0 is the thickness of the thermal boundary layer. The atmospheric thermal gradient is estimated by linear interpolation between the Viking Lander near-surface measurement and the IRTM 25 km measurement.

The minimum value (left boundary of the shaded region in Figure 4.5) would be for the adiabatic atmosphere starting with the temperature given by the ambient sensor on VL-2. The profile considered in my study is a linear interpolation between the surface temperature from VL-2 and temperature at the 25 km altitude from 15 μm IRTM band. The extreme case (right boundary of the shadowed region) is for the thermal inversion during a dust storm. This inversion is not considered very likely at the time of my study (late winter).

The Figure 4.5 profile is for the $L_S = 325°$ and latitude of 48° N, values approximate for the Viking Lander 2 site at the time of winter frost retreat. The thickness of the thermal boundary layer, the magnitude of the diurnal temperature variation near the surface, and the temperature profile is an estimate based on these sources:

- theoretical calculation of Flasar and Goody (1975),
- GCM simulation of Pollack *et al.* (1981),
- spacecraft radio occultation measurements (Davies 1979b, Lindal *et al.*, 1979),

- Mariner 9 IRIS atmospheric temperature profiles (M. Santee and D. Crisp, personal communication, 1989), and

- calculation of diurnal variation of meteorological parameters at the Viking Lander sites (Sutton *et al.*, 1979).

The result is a compromise between the desire for accurate representation of the atmospheric temperature (particularly regarding the sensitivity of water vapor pressure on temperature) and a realistic assessment what is known about the atmospheric state at this particular latitude and season.

The constant thermal gradient with diurnal perturbation is not that much different as compared with one of the best sources of temperature profile data — from Mariner 9 IRIS experiment (M. Santee and D. Crisp, personal communication, 1989). This data set has a vertical resolution of about one scale height which hides possible thermal wave propagating upward (as seen in Viking Lander temperature profiles during entry). But I am interested primarily in diurnal variations, not in the absolute value of total atmospheric water-vapor holding capacity. A pocket of warm air at 25 km altitude can potentially contain substantial amount of water vapor but this water vapor is not available for surface interaction on a diurnal timescale.

Further support for not considering a potential localized storage of water vapor at high altitudes comes from the following feedback: a higher degree of sub-adiabatic temperature profile will create a more stable atmosphere, thus diminishing the effect of this high-altitude water. On the other hand, a closer-to-adiabatic temperature profile will enable more vigorous vertical mixing, but the amount of available water vapor will decrease. In both cases, this enables me to use the simplified model for vertical temperature profile as described above.

4.2.3 Atmospheric water vapor

In this subsection, I am going to use the thermal structure of the atmospheric boundary later described above to calculate the atmospheric holding capacity and relative humidity. Results are summarized in Figure 4.6.

First, I have to derive the relationship between the column abundance of atmospheric water vapor and the equivalent amount of water ice if all water vapor would precipitate on the surface. For this calculation, I am assuming that the scale height for vertical distribution of water vapor is the same as the scale height of the bulk of the atmosphere (in hydrostatic equilibrium). In that case, the column abundance of water vapor (m/A, in kg/m^2) can be expressed as:

$$\begin{aligned} \frac{m}{A} &= \int_z \frac{dm(z)}{A} = \int_z \mu \cdot n(z) \cdot dz = \int_z \mu \cdot n(0) \cdot \exp(-z/H) \cdot dz \\ &\approx \mu \cdot H \cdot n(0), \end{aligned} \tag{4.4a}$$

where m is the water vapor weight, A is the surface area, z is the altitude, μ is the molecular weight of water, $n(z)$ is the water vapor concentration, and H is the atmospheric scale height. The next step assumes ideal gas equation: $p = nkT$, where p is the pressure, k is the Boltzman constant, and T is the temperature. Then, the height h of the water vapor column if precipitated in the ice phase on surface is:

$$h = \frac{1}{\rho_{ice}} \frac{m}{A} = \frac{\mu}{\rho_{ice}} \cdot n(0) \cdot H = \frac{\mu}{\rho_{ice}} \cdot \frac{p_v}{kT_S} \cdot H, \tag{4.4b}$$

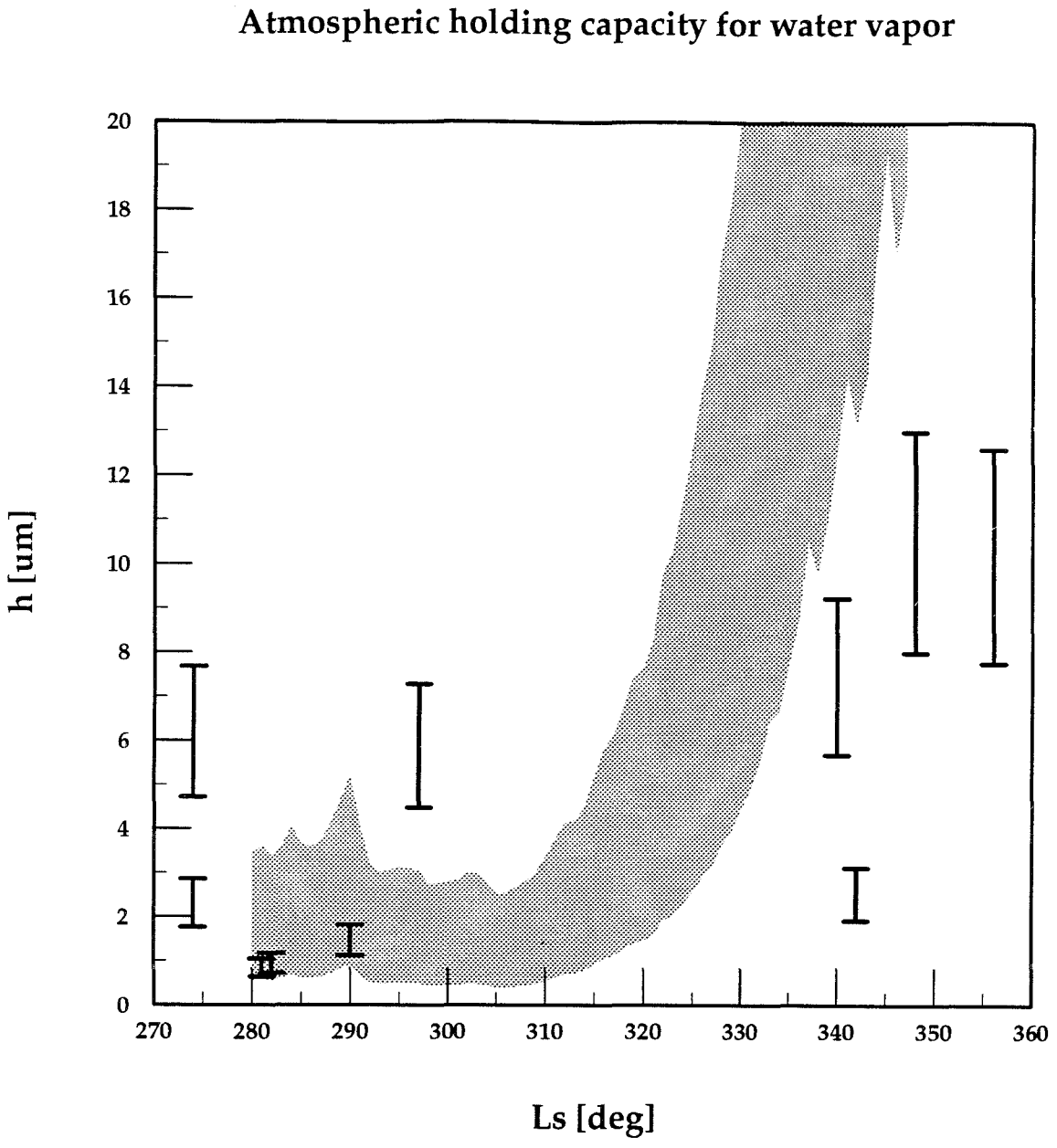

Figure 4.6 Atmospheric holding capacity for water vapor above VL-2 site (in precipitable micrometers). The shaded area is the calculated atmospheric holding capacity for water vapor from the IRTM 15 μm and VL-2 ambient sensor (using the temperature profile from Equation 4.1). The data set with the error bars are the averaged MAWD data points from individual Viking Orbiter passes corresponding to the VL-2 latitude but with varying longitude.

where ρ_{ice} is the H_2O ice density and $p_v(T)$ is the water vapor pressure at the surface temperature T_S.

The shaded area in Figure 4.6 represents the variation derived from the diurnal VL-2 site temperature cycle as calculated from the VL-2 ambient sensor and IRTM 15 μm temperature. The small peak around $L_S \approx 290°$ is because of the warmer atmosphere during the second dust storm. The irregularities at the minimum boundary at the late winter ($L_S > 330°$) are an effect of the local VL-2 meteorology. The other data set in the graph are the MAWD measurements (averaged data points including error bars). It is important to note that, during the late winter ($L_S \approx 330°$), the atmospheric water vapor content does not rise as rapidly as the atmospheric holding capacity for water vapor.

In addition to the vertical temperature profile, the saturation by water vapor (relative humidity) depends also on the vertical distribution of water vapor. In contrast to the pre-Viking suggestions of strong water vapor concentration in the bottom few kilometers (Flasar and Goody, 1975), current understanding favors a more mixed state of the water vapor in the Martian atmosphere. Water vapor is expected to mix uniformly for at least two scale heights (Davies, 1979a). There may be some enhancement of relative humidity in the bottom few kilometers, but this is primarily driven by diurnal variations in the thermal boundary layer. Atmospheric saturation near the surface on a diurnal basis is hinted at by several independent pieces of evidence: morning fogs (Jakosky *et al.*, 1988, Murray *et al.*, 1991), diurnal optical depth variation (Pollack *et al.*, 1979) and temperature inflection (Ryan and Sharman 1981).

It can be noted that at the at coldest period of the winter ($L_S < 300°$), the observed MAWD water vapor column abundance is higher than the one calculated from the Viking Lander surface temperature. This is due to the increased atmospheric temperature at altitude of 20–40 km due to the dust loading from the dust storms. My model of the vertical temperature profile does not deal with this possibility, as mentioned in the previous paragraph. This sub-adiabatic temperature profile could increase water vapor column abundance, probably combined with the transport from the lower latitudes. However, this effect becomes less important later ($L_S > 300°$) because the atmosphere clears significantly and gets cooler. Also, water vapor at these altitudes does not readily exchange with the surface on the diurnal timescale. Therefore, my calculations do not specifically apply to the possible water vapor which can be stored at these higher altitudes.

4.2.4 Atmospheric transport

For the purpose of this study, it is necessary to estimate the vertical mixing and horizontal transport of water vapor in and out of the Martian atmosphere. This is, as might be expected, poorly known. In addition to the set of Lander meteorology measurement (performed at the fixed height of only 1.5 m above the ground; Hess *et al.*, 1977), other sources are:

- the wind structure measured during the Lander descent (Seiff and Kirk 1977),
- GCM simulations (Pollack *et al.*, 1981),
- terrestrial analogies (Sutton 1953), and

- theoretical calculations (Holton 1979, Priestley 1959, Plate 1971).

More details will be presented in the relevant subsection on the physical processes of the proposed model.

There is an important distinction regarding the calculation of vertical transport of water vapor from the surface to the atmosphere. On the Earth, the greatest obstacle is formed by the boundary sublayer just above the surface (less than one meter). Once the water vapor gets above this sublayer, then further vertical transport is relatively fast compared with rate of saturation of the atmosphere with water vapor. Therefore, a simple 2-layer model can be used (Figure 4.7) — diffusion from infinite source (surface, e.g., ocean) to very large reservoir (atmosphere above the boundary sublayer) through a narrow conduit (this boundary sublayer) — Brutsaert, 1982. In the first approximation, the rate of vertical transport which depends on the relative humidity above the boundary sublayer is not a function of itself. The transport above is fast enough to diffuse water vapor away into higher altitudes from above this sublayer. This keeps the relative humidity above the boundary sublayer only a slowly changing function of the vertical transport.

The situation on Mars is quite different. The rate of sublimation (controlled by absorbed solar energy) is smaller only by a factor of about 2.3 . But the atmospheric water vapor holding capacity is lower by a factor of 10^{-4}. Therefore, it is much easier to saturate the atmosphere near the surface. A model used to calculate the vertical transport of water vapor through the Martian atmosphere has therefore to take into account the implicit dependence of the vertical transport rate on itself. This drastically limited holding capacity of the atmosphere for water vapor requires

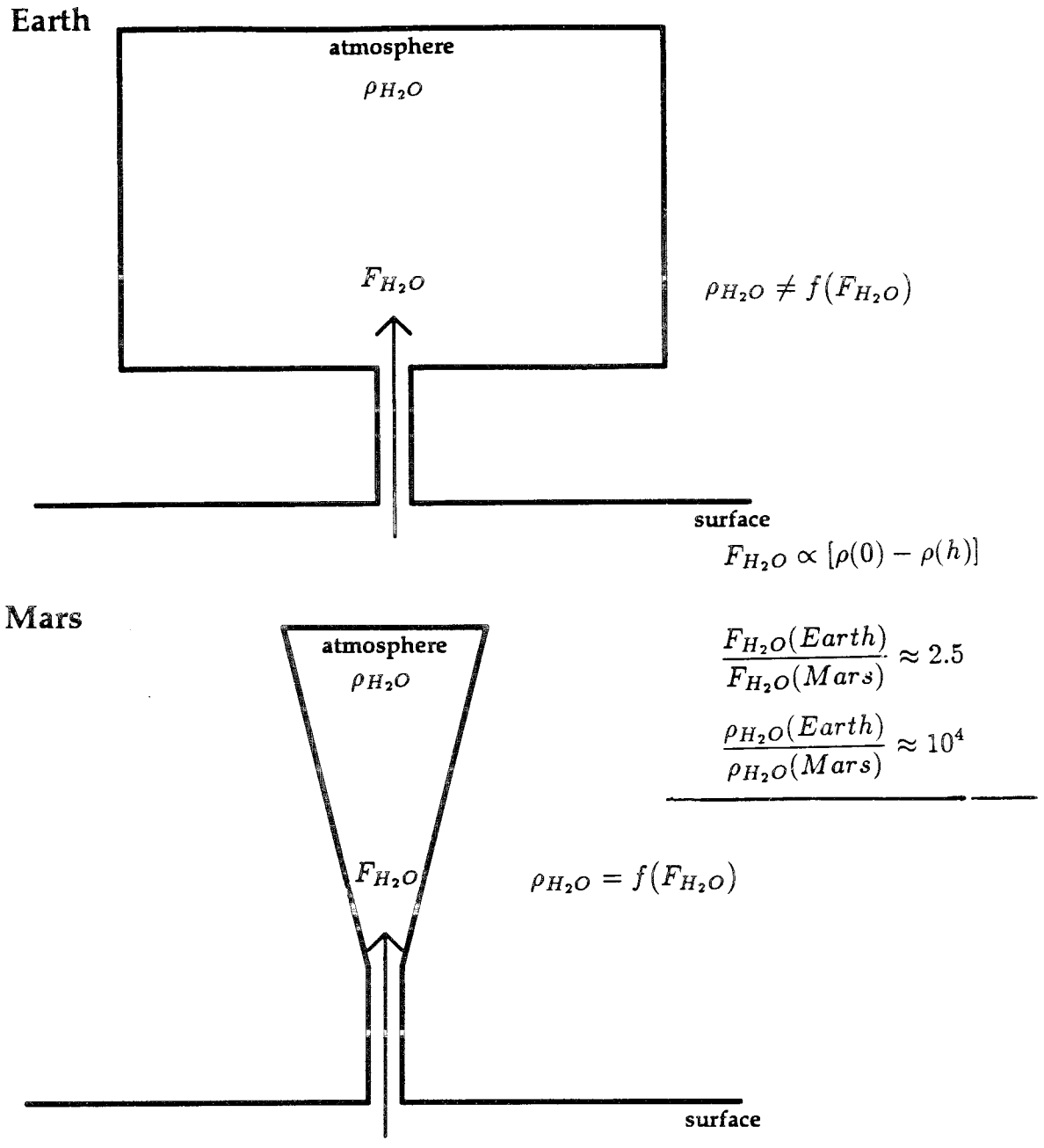

Figure 4.7 Difference in boundary layer dynamics on Earth and on Mars. On Earth, the diffusion through the laminar sublayer just above the surface is the most limiting effect. The rate of diffusion through this layer does not depend on itself because the large available holding capacity of the atmosphere (even in very humid environment) above this sublayer. On Mars, situation is quite different (due to much lower atmospheric holding capacity for water vapor). Therefore the simple 2-layer cannot be used.

the use of a multi-layer model which keeps track of different level of saturation throughout the atmosphere.

4.2.5 Surface temperature

Another important parameter for this study is surface temperature. This is required to calculate the frost stability on ground. Several sources of data were originally sought in order to assure the realistic understanding of the surface temperature. First, the Viking Orbiter infrared radiometer IRTM had a 20 μm band which gives surface temperature averaged over the field of view (typically 40 km — Kieffer *et al.*, 1977). Second, the footpad temperature sensor on the second leg of the Lander (J. Tillman, personal communication, 1989) provided data on the surface temperature at the VL-2 site. Third, I performed the numerical calculation of surface thermal balance based on the solar energy, thermal radiation and heat conduction into the ground (similar to Kieffer *et al.*, 1977 and others). However, after comparing these data, I used for this analysis only the 20 μm IRTM measurements which I considered to be most reliable in spite of the averaging effect. Data from first two sources (IRTM — solid line and footpad — dashed line) are compared in Figure 4.8. The footpad data are probably contaminated by the presence of the Lander body — a source of thermal radiation and a shade of the Sun. The conduction of heat through the footpad was considered to negligible. The diurnal minimum and maximum are averaged over 10 deg of L_S (depicted by vertical bars). In the final analysis, only IRTM data were used, because the VL-2 footpad sensor data were probably contaminated by the presence of the lander body itself.

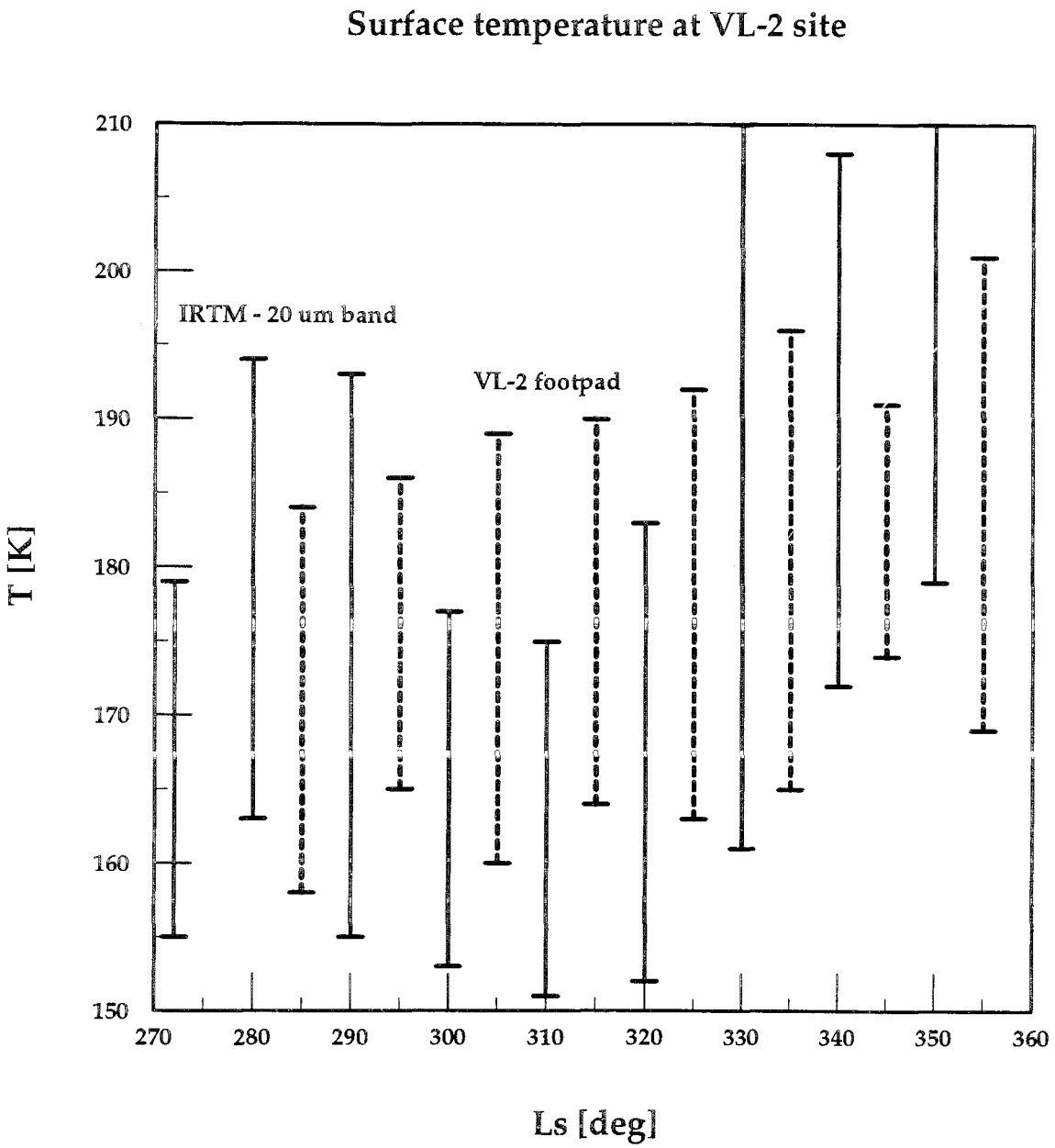

Figure 4.8 Surface temperature from IRTM (solid line) and VL-2 footpad sensor (dashed line).

4.2.6 Diffusion in the soil

I have investigated the suggestion that the diffusion in and out of the soil may play the role on the diurnal and sub-seasonal scale. The grain size distribution of the soil is the critical parameter for estimation of the diffusion transport. I have looked for suggestions about the grain size distribution at these sources:

- atmospheric scattering (Pollack *et al.*, 1979, Zurek 1982),
- thermal inertia (Kieffer *et al.*, 1977, Jakosky 1986, Murray *et al.*, 1990),
- Lander mechanical properties (Moore *et al.*, 1987),
- dust settling after landing,
- phase function from orbit and Viking Lander,
- geology arguments (presence of dunes requires sand saltation — Sharp and Malin 1984),
- dust storm arguments (wind necessary to pick up dust grains and later settling).

This indirect evidence strongly suggests the presence of a bimodal size distribution of dust/sand particles:

- very fine dust (micron and sub-micron size) which constitutes the atmospheric dust, and
- coarser particles (hundreds of μm in size, maybe bonded together) which constitute most of the mass of surface material (Moore *et al.*, 1987).

In most cases, the diffusion properties of the material would be controlled by smaller size particles. Approximate analysis, as well as careful calculation, in Zent *et al.* (1986), Clifford and Hillel (1986), Jakosky (1983), Toon *et al.* (1980), and Flasar and Goody (1975) shows that, in this case, the magnitude of atmosphere/regolith interactions (diffusion in regolith, adsorption on regolith) will be negligible on a diurnal timescale. This, of course, applies strictly only to the area and time I have studied (VL-2 winter frost).

4.3 Proposed model of cold trapping

A sketch of the proposed model is shown in Figure 4.9. My study of the Viking Lander 2 observations suggests that H_2O frost occurs in two forms:

- thin, almost continuous, early frost (Figure 4.2), and
- much thicker, patchy, later frost (Figure 4.3).

Both frost forms contain essentially the same total water content but they cover different fractions of the surface. The transition between two frost forms occurs by recondensation at local cold traps when solar insolation sublimates the first frost but the atmosphere is still too cold to transport the resultant water vapor on a global scale (beyond $10^0 - 10^4$ meters). These cold traps are created by shadowing from the small scale surface roughness — rocks, troughs, etc. The critical feature of the hypothesis is disparity between local and long-range transport of water vapor by the atmosphere which delays the release of water vapor into atmosphere. In order

Two forms of frost:

A) Early frost: thin layer (10 - 20 um)
almost continuous surface coverage

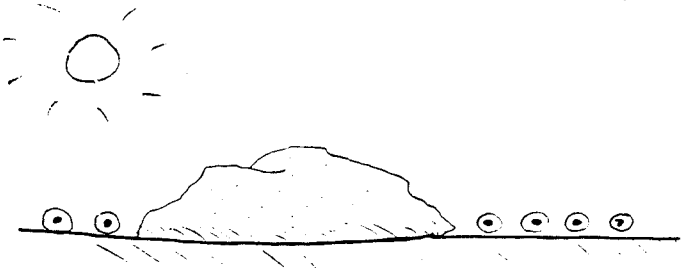

B) Later frost: thicker frost (100 - 200 um)
fraction of surface ("cold traps")

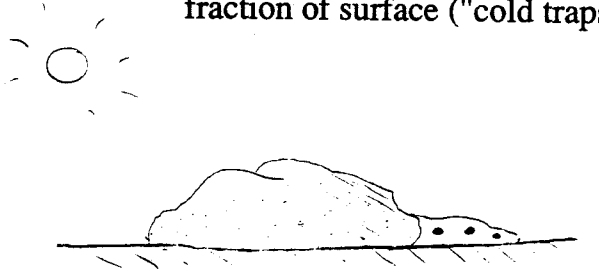

C) Transition: timing by surface temperature ($L_s \approx 315$)
limited atmospheric transport process
redeposition at locally favorable areas

Figure 4.9 Cartoon of the model

to justify my model of H_2O behavior, I must first discuss frost sublimation and condensation, surface thermal balance, and water vapor transport in the boundary layer.

4.3.1 Sublimation of frost

Water on the Martian surface occurs in only two phases — solid and vapor. The solid and vapors are in equilibrium if the partial pressure of water above solid ice follows this relation (Dorsey, 1940):

$$\log p_v(T) = \frac{A}{T} + B\log(T) - CT + DT^2 - E \ \ [Pa], \tag{4.5}$$

where A = -2445.6, B = 8.23, C = -0.01677, D = 1.2E-5, and E = -7.781. This is independent of the total ambient pressure created by other gases (CO_2 in this case). The transition from one phase to another is accompanied by the release or absorbtion of latent heat:

$$L(T) = A - B(T + C)^2 \ \ [J/kg] \tag{4.6}$$

where A = 2.839E6, B = 3.6, and C = 35. The water ice becomes unstable by either increase of the temperature of the solid phase or depletion of the vapor phase above the ice. Kinetics of transition from solid to vapor phase can be calculated in four possible regimes: molecular flow, molecular diffusion, forced convection, and free convection.

The molecular flow occurs at low temperatures where interactions between vapor molecules can be ignored because of low density of the vapor. This can be a relatively rapid form of sublimation which is limited only by the energy input and the kinetic rate ($\approx 10^{-2}$ μm/s at the typical VL-2 winter temperatures):

$$\frac{dh}{dt} \approx \frac{\mu \cdot p_v(T) \cdot v_{th}(T)}{\rho_s \cdot kT} \approx \frac{\rho_v(T)}{\rho_s} \cdot v_{th}(T). \tag{4.7}$$

where h is the frost layer thickness, μ is the molecular weight, p_v is the vapor pressure, $v_t h$ is the thermal velocity of vapor, p_s and p_v is the solid and vapor phase density. However, the conditions for this type of sublimation are truly valid on Mars only in a very thin layer just above the frost ($\approx 1 - 5$ μm). On a larger scale, some of the following mechanisms have to be considered.

Molecular diffusion is important in the stably stratified atmosphere or in the laminar sublayer which occurs just above the surface (on scale of 0.01–0.1 meter). The coefficient for the molecular diffusion of H_2O through CO_2 gas at the Martian temperatures is typically $0.001[m^2 s^{-1}]$. This would limit the water frost sublimation to only about 0.1 μm on a diurnal basis — this is based on the typical molecular diffusion distance of 10 m in one day. The remainder of solar energy input would go into increased temperature leading to corresponding higher vapor pressure.

This situation will last until the lower molecular weight of H_2O (as compared to CO_2) causes unstable stratification quite analogous to the thermals found during hot days on Earth (Ingersoll 1970). This free convection environment does not practically limit water vapor sublimation — in this case the frost sublimation is limited by solar energy input.

Even if the situation described above requires in principle very little water vapor to decrease the average molecular weight of the gas, in the practical situation inertial forces will limit this phenomenon to a rather high mixing ratio of H_2O to CO_2 which in turn is possible only at a temperature closer to the melting temperature. Therefore forced convection is the most probable concept for the water frost sublimation at the VL-2 site. Knowledge of the wind profile of the boundary layer is necessary in order to quantify this loss mechanism. Diffusion using an eddy mixing coefficient represents the simplest approach (see later in this section).

4.3.2 Condensation of frost

The opposite process of sublimation is condensation. Careful understanding of this process is required for any cold-trapping hypothesis. Water vapor is depleted from the atmosphere by coming into contact with the surface at a temperature lower than the temperature corresponding to the water vapor partial pressure $p_V(T)$. This "cold-finger" mechanism is complicated on Mars by the presence of non-condensable gas — CO_2 . Therefore, water vapor has to diffuse in on the surface from the CO_2 atmosphere and latent heat has to get away, by radiation, conduction, or convection. From the Earth analogs, we assume the existence of a laminar sublayer in the boundary layer which has a thickness several times less than the typical surface roughness (Priestley 1959). The effectiveness of the cold-trapping depends on the rate of 1) heat transfer through this laminar sublayer and 2) water vapor molecular diffusion through the same layer.

First, the heat transfer rate is dominated by the radiative transfer. This easily removes latent heat released by the condensing water vapor. The increase in surface

temperature by one degree Kelvin will suffice to remove latent heat generated by water vapor condensing at the rate of 2 μm/hour. This figure (2 μm/hour) is about the most extreme upper limit on the frost deposition rate on the surface at which latent heat can still be removed by only a slight increase in the surface temperature. Therefore, the removal of latent heat will not constitute the limiting factor on the water frost condensation on the surface. Second, water vapor diffusion (through this laminar sublayer composed of a non-condensable gas) could be the other limiting factor. The magnitude of the diffusion rate can be estimated from $x^2 \approx Dt$. For $D \approx 0.001\ m^2 s^{-1}$ and $x \approx 1$ mm, I get $t \approx 1$ msec which is much less than would be required for any reasonable rate of water vapor condensation. Therefore, this analysis of water vapor condensation in the presence of CO_2 suggests that the water vapor condensation on colder spots of the surface (cold traps) will occur at the rate controlled by supply of water vapor and will not be limited by the presence of non-condensable gas.

Another factor that should be included is the accommodation coefficient of water molecule condensation onto a rock or ice surface. Unfortunately, reliable measurements performed under the postulated Martian conditions are scarce and therefore this effect is not further quantified here. I assume the value of accommodation coefficient to be 0.8 although I have no reason to believe that this value should be substantially smaller than unity.

I have also considered another postulated mechanism for condensation — on nuclei (dust grains) in the atmosphere. However, this cannot be important on a diurnal timescale. The fall-out rate for dust grains is significantly more than one day (Pollack *et al.*, 1979). Therefore, the amount of water frost deposited on the surface is not more than a small fraction of a micrometer per day. This can be estimated

as follows: a "precipitable" layer of suspended dust (1–5 μm assuming micron sized particles and optical depth $\tau \approx 1 - 3$) times the ice/dust mass ratio of nuclei (≈ 1) divided by dust decay timescale (20–50 days). This mechanism, in order to be effective, would require very large grains with unrealistically thick water frost envelope. However, this mechanism may prevail during the initial deposition of frost on the surface in the late fall (Pollack *et al.*, 1979) when deposition rates are 10 to 100 times slower.

4.3.3 Thermal balance of thin frost layers

When describing the thermal balance of thin ice layers, several non-trivial effects must be considered — albedo, thermal emissivity, phase function. The effectiveness of masking the underlying color (i.e., red soil) of the substrate depends on the frost structure (grain size and form of deposition) as well as the thickness. Therefore, a precise calculation is very difficult, but experimental data (Clark 1980, Warren 1982) are consistent with my assumptions and measured optical properties: A water frost layer 10–20 μm thick (early frost covering completely the surface) will not be able to mask the underlaying red color of the substrate, so the frost will have reddish tint. A water frost layer 100–200 μm thick (which is suggested for the later frost in cold traps) could have largely white color (not considering a possibility of contamination by dust).

One interesting suggestion is the solid state greenhouse effect caused by solar heating beneath an ice layer. However, no significant temperature gradient can be sustained by such a thin layer (B. Jakosky, personal communication, 1990).

In addition to this effect, the reverse phenomenon has to be considered as well, which I call "inverse" greenhouse effect lacking better terminology. By this, I mean the effect of thinness of the frost layer on thermal emission from the frost. Because the frost changes the color of the surface, it has to absorb some fraction of sunlight. However, the expected early frost thickness (10–20 μm) is about the same as a thermal wavelength. This could cause the emissivity to be significantly lower than unity which would not allow the frost to reradiate all solar radiation it receives in shorter wavelengths. This excess energy would have to be conducted into the underlaying soil, and thus causing a thermal gradient at the frost/soil interface. The frost will be warmer than the soil, which is quite opposite to what is normally understood as a solid-state greenhouse. However, as in the previous paragraph, any thermal effect will be negligible for such a thin layer. But this implies that it may be quite difficult to see such a frost layer in thermal wavelengths.

A thin frost layer can also have a profound effect, in principle, on the phase function in reflection. There are suggestions (Smith *et al.*, 1969) that thin frost layers (less than about 200 μm) can exhibit a substantial specular reflection peak. This is to be compared with the Lambertian reflection of more massive layers. Unfortunately, there are essentially no laboratory data demonstrating the effect of grain size on the phase function of thin frost layers (Warren 1982), and, therefore, I did not consider the absence of a specular reflection to be a reliable indicator of thickness.

4.3.4 Surface roughness and water frost stability

Using the estimates of solid/vapor transition, sunlight absorption, and thermal emission, it is feasible to calculate the stability of water frost deposited on a surface. The temperature of the frost must be between a minimum temperature corresponding to the partial pressure of water vapor in the atmosphere (for unlimited water frost supply), and a maximum temperature corresponding to that a non-volatile material of the same albedo as the frost would achieve due to solar insolation and reradiation (for a fully saturated atmosphere). I assume that the horizontal dimensions of the frost patch are greater than the scale for the horizontal heat transport from the bare, darker surface on the diurnal timescale. (If this is not so, the stability of frost patch will be diminished.) This critical distance is about 15 cm and is basically several times larger than the diurnal thermal skin depth.

Another effect influencing the surface frost stability is the small-scale surface roughness created by rocks, troughs, etc. Small-scale surface roughness has three thermal effects which are difficult to model precisely and which were extensively discussed in the Chapter 2: 1) non-uniform sunlight distribution, 2) subsurface horizontal heat flow, and 3) radiation shadowing of the surface. Fortunately, for the purpose of this study, only the overall effect of these effects is needed here.

There is a crucial difference in the present discussion as opposed to the Chapter 2. At the VL-2 location, because the terrain is rocky and has relatively low albedo, the surface roughness creates *cold traps* which have consistently lower temperature than would have the equivalent flat surface. For some fraction of surface elements, the sunlight shadowing becomes more important than thermal reradiation from the walls. Because of low albedo, the multiple scattering of sunlight is negligible.

A point calculation shows that the net effect of such type of roughness on the temperature of certain surface elements (potential cold traps in shadow) is to moderate temperatures extremes. This is due to the less insolation during the day (lower maximum temperature) as well as due to the smaller exposure to the cold sky/space during the night hence leading to smaller losses by thermal radiation (higher minimum temperature). In reverse, the surface elements more exposed to the sunlight due to the surface roughness would experience larger temperature extremes.

4.4 Calculated frost thickness

In this work, I have used a simple one-dimensional finite difference thermal diffusion model with the radiative boundary condition on the top, with the latent heat contribution from H_2O sublimation and deposition, and with the proper solar insolation geometry. I have adjusted values of the atmospheric optical depth and thermal infrared atmospheric downward flux until I was able to replicate the IRTM surface temperature measurement. This was with no frost deposition or sublimation. The thermal inertia was kept constant at $I = 6.5$ (in units of 10^{-3} calcm^{-2} s$^{-1/2}$ deg^{-1}). The next step was to calculate the thickness of water frost deposited or sublimated using the parameters from above. The calculation was based only on thermodynamical balance and does not include mixing in the boundary layer and the cold-trapping. The frost deposition/sublimation was in the molecular flow regime, limited only by the energy balance and the kinetic rate.

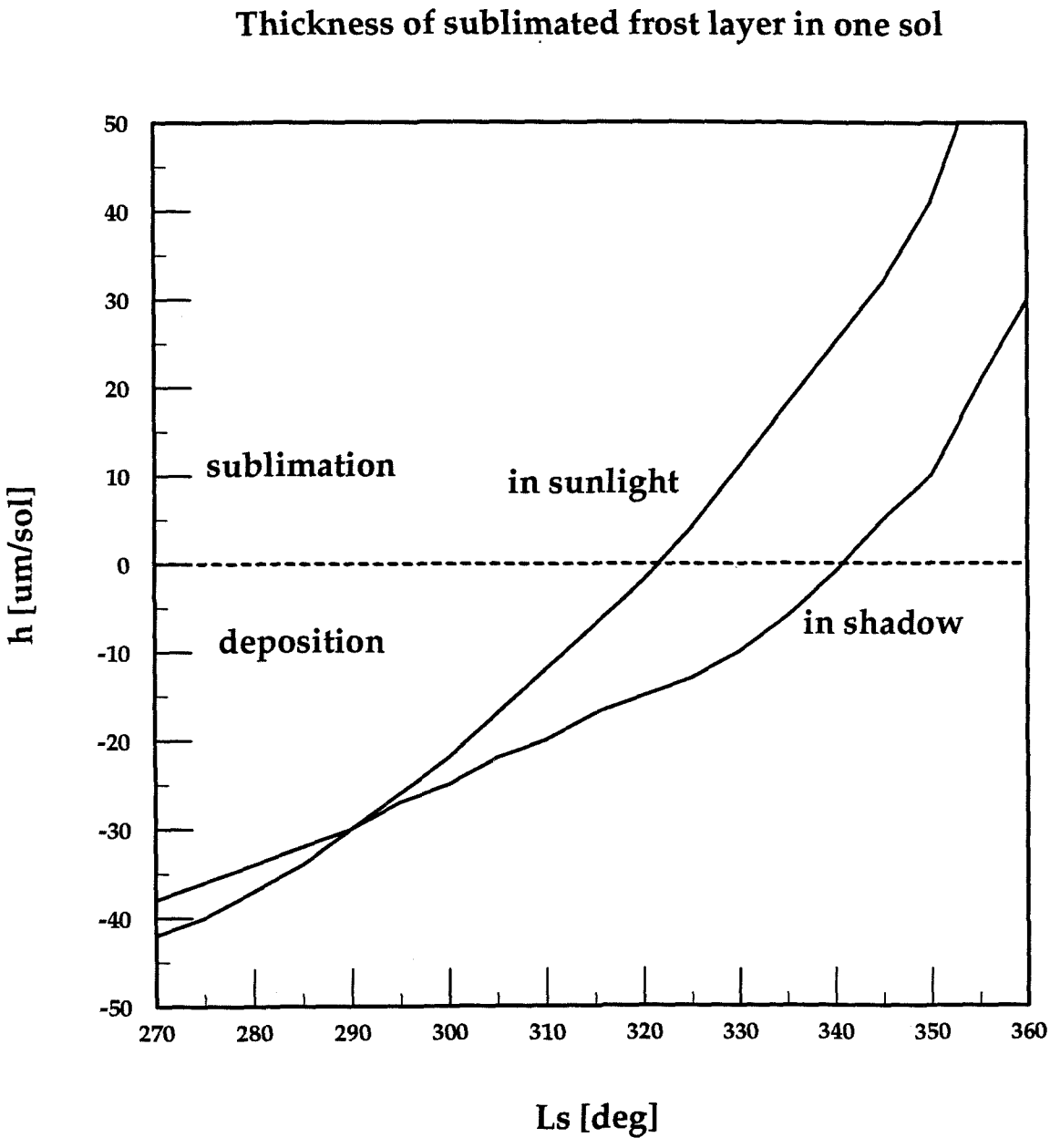

Figure 4.10 Thickness of the sublimated frost layer in one sol for two different situations (frost in full sunlight, frost in shadow) as a function of L_S.

The frost deposition was calculated from amount of latent heat necessary to keep surface temperature at a value corresponding to saturation pressure of water vapor derived from MAWD measurement:

$$L\,\dot{m} \approx \sigma T^4(IRTM) - \sigma T^4(\rho_{water}^{MAWD})$$

This, of course, assumes practically unlimited supply of water vapor from the atmosphere, which in turn would require very large vertical mixing in the atmosphere. Therefore, I do not expect this calculation to yield the realistic values for frost deposition and sublimation because I neglected the atmospheric effects (limited atmospheric transport and boundary layer mixing — see below). The values in Figure 4.10 are overestimated by a factor of several. But the purpose of this exercise is threefold.

First, it predicts fairly accurately the time when the net sublimation of water frost exceeds the net deposition and therefore when I should expect the frost layer to break up. Second, it shows that the difference between net sublimation for the fully illuminated frost and shadowed frost is about $20°L_S$ (which is consistent with the Viking Lander 2 image sequence). Third, the primary constraint on the behavior of water frost at this site is overwhelmingly the atmospheric effects (i.e., vapor supply, boundary layer mixing). Once the solar energy input reaches sufficient level for the net water frost sublimation, then it can sublime in just few days more water frost than I could ever expect in a continuous deposit on the surface at the Viking Lander 2 site. This is, of course, inconsistent with the observed behavior (I have observed that the water frost stays for much longer than a few days — it is stable for up to 80 sols).

Results are presented in Figure 4.10 — the thickness of deposited or sublimated frost layer for two situations (frost in full sunlight, frost in partial shadow) as a function of L_S. The values for the frost in full sunlight is for the thermal inertia given above ($I = 6.5$). The values for the frost in partial shadow comes from the model with the increased thermal inertia ($I = 7.7$). This is based on the temperature/roughness feedback model which preceded the better model described in Chapter 2. The increased thermal inertia value corresponds to an obscuration/shadowing of sunlight of about 20 per cent — probably typical for residual frost patches at the Viking Lander 2 site).

The work described in this section follows closely a previous study of Hart and Jakosky (1986). In addition, I have added the consideration of shadowed frost and further extended the model with boundary layer transport and frost recondensation. I believe that these three effects (shadowing, boundary layer transport, recondensation) have profound implications for behavior of water at VL-2 site and possible at other locations.

4.5 Boundary layer transport

In this section, I am going to couple the sublimation/deposition model from the previous section with the some extremely simplified boundary layer dynamics. To deal with water vapor mixing and transport in the boundary layer adequately, I have attempted to create a subset of assumptions which would be consistent with the inadequately known structure of the atmospheric boundary layer on Mars. The horizontal and vertical components of the wind in the boundary layer are:

$$u = < u > + u\prime, \tag{4.8}$$

$$w = < w > + w\prime, \tag{4.9}$$

where $< u >$ and $< w >$ designate the mean velocity and u and w designate the deviation from the mean. I am considering only the two-dimensional model with horizontal and vertical winds. I also assume the vertical atmosphere motion will average to zero ($< w >= 0$). I further assume the logarithmic wind profile (Holton 1979) for the surface layer (the thickness of which is on the order of meters or tens of meters):

$$< u >= \frac{u_*}{k} \ln(\frac{z}{z_0}), \tag{4.10}$$

where u_* is the friction velocity, k is the Karman constant experimentally determined to be about 0.4, z is the altitude, and z_0 is the roughness length. This length is approximately an order of magnitude smaller than the physical size of surface roughness (Priestley 1959). The friction velocity u_* is defined as:

$$u_*^2 = (\tau_x / \rho)_s, \tag{4.11}$$

where τ_x is the surface stress and ρ is the atmospheric density. The diffusion calculation employs the idea of an eddy diffusion coefficient which can be estimated from:

$$K\frac{\partial u}{\partial z} = u_*^2, \tag{4.12}$$

$$K = ku_*z = u_*l, \tag{4.13}$$

where l is the mixing length. This surface layer with the logarithmic wind profile extends to a height of about:

$$h \approx 0.2u_*/f, \tag{4.14}$$

where f is the Coriolis parameter. Above the surface layer, the eddy diffusion coefficient K in the Ekman layer is independent of height. This is the result of the assumption that the mixing length is proportional to the characteristic scale of the turbulent eddies, which, in turn, is nearly constant with the height above this surface layer. On the other end of the scale, mixing on the scale of surface roughness depends on the existence of a laminar sublayer. If

$$u_*z_0/\nu > 2.5 \tag{4.15}$$

then the flow is aerodynamically rough, with viscous stress smaller than eddy pressure forces from flow over surface roughness (there eventually has to be some laminar flow just next to the surface but only microscopically thin). Based on values presented in Figure 4.11, I expect this to be the case for the Viking Lander sites.

Values used for the calculation are anchored at the bottom by the Lander meteorology measurement, at the top by the GCM results, and partially by the Lander

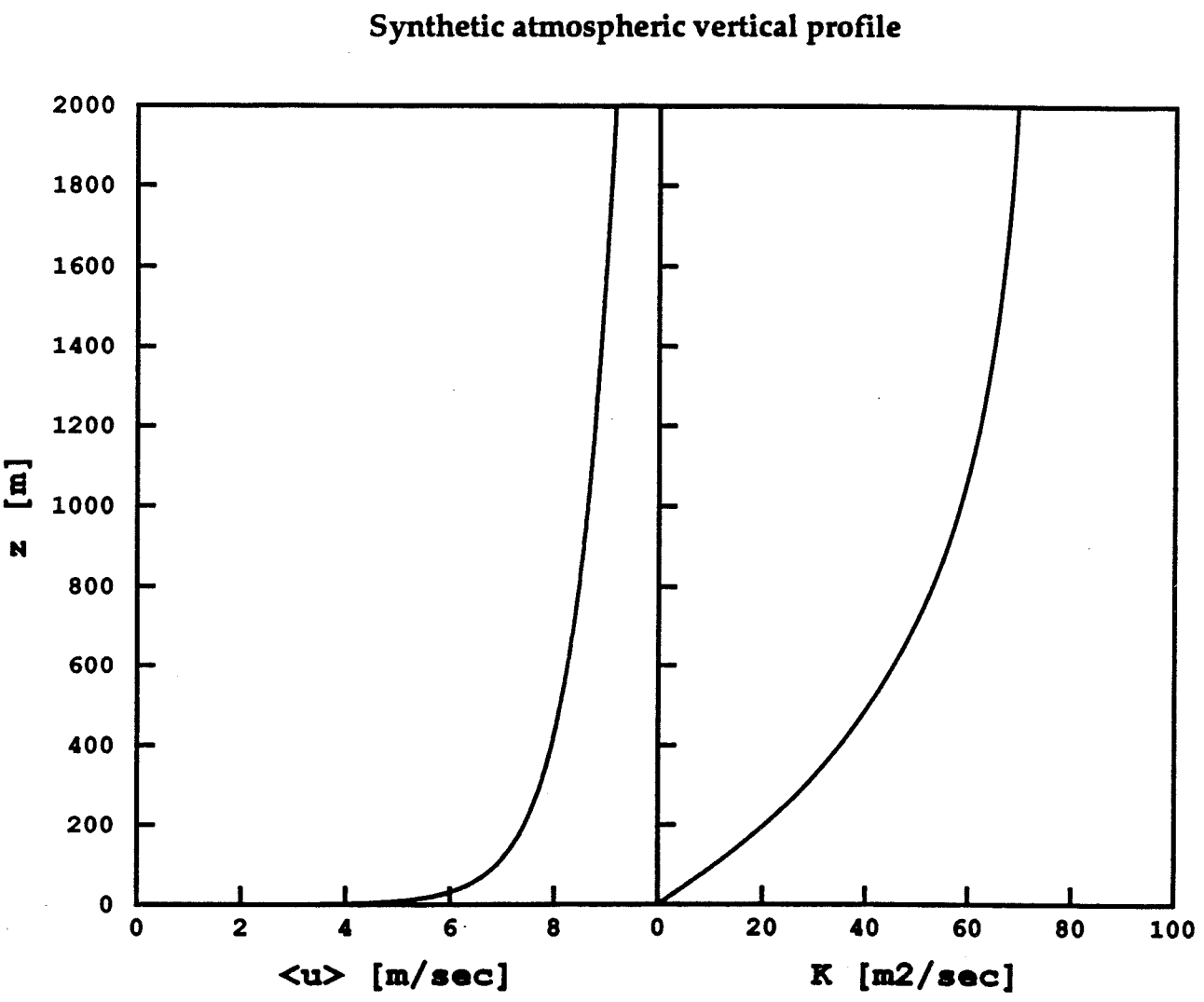

Figure 4.11 Synthetic atmospheric profile — zonal winds $< w >$ and water vapor mixing coefficient K as a function of height.

descent wind measurement. The synthetic atmospheric profile is summarized in Figure 4.11 — zonal winds and water vapor mixing coefficient as a function of height.

4.6 Quantitative test of proposed concept of cold-trapping at VL-2 site

In this section, I compare the environmental observations with expectations based upon my model. First, I present arguments based on the changes in frost surface coverage and its timing of transition as compared with frost stability. Second, evidence from the water vapor column abundance and the vertical transport in the Martian atmosphere will be discussed.

4.6.1 Frost surface coverage, its color and timing of transition

Changes of frost surface coverage and color as a function of L_S are plotted in Figure 4.12. The filled squares are red/blue ratios from the red color on the VL-2 calibration target (typically around 3.0). The empty squares are red/blue ratios from the white color on the VL-2 calibration target (typically around 1.0). The crosses represent the averaged color of the typical frost which disappeared quickly around $L_S \approx 325°$. The pluses represent the color of the late frost which stayed longer and was getting "whiter" (less red) during the general disappearance of most of the frost.

Note the sharp transition from full coverage of the surface by frost to partial coverage (typically 15 per cent). There were parallel color changes of the frost layer (also

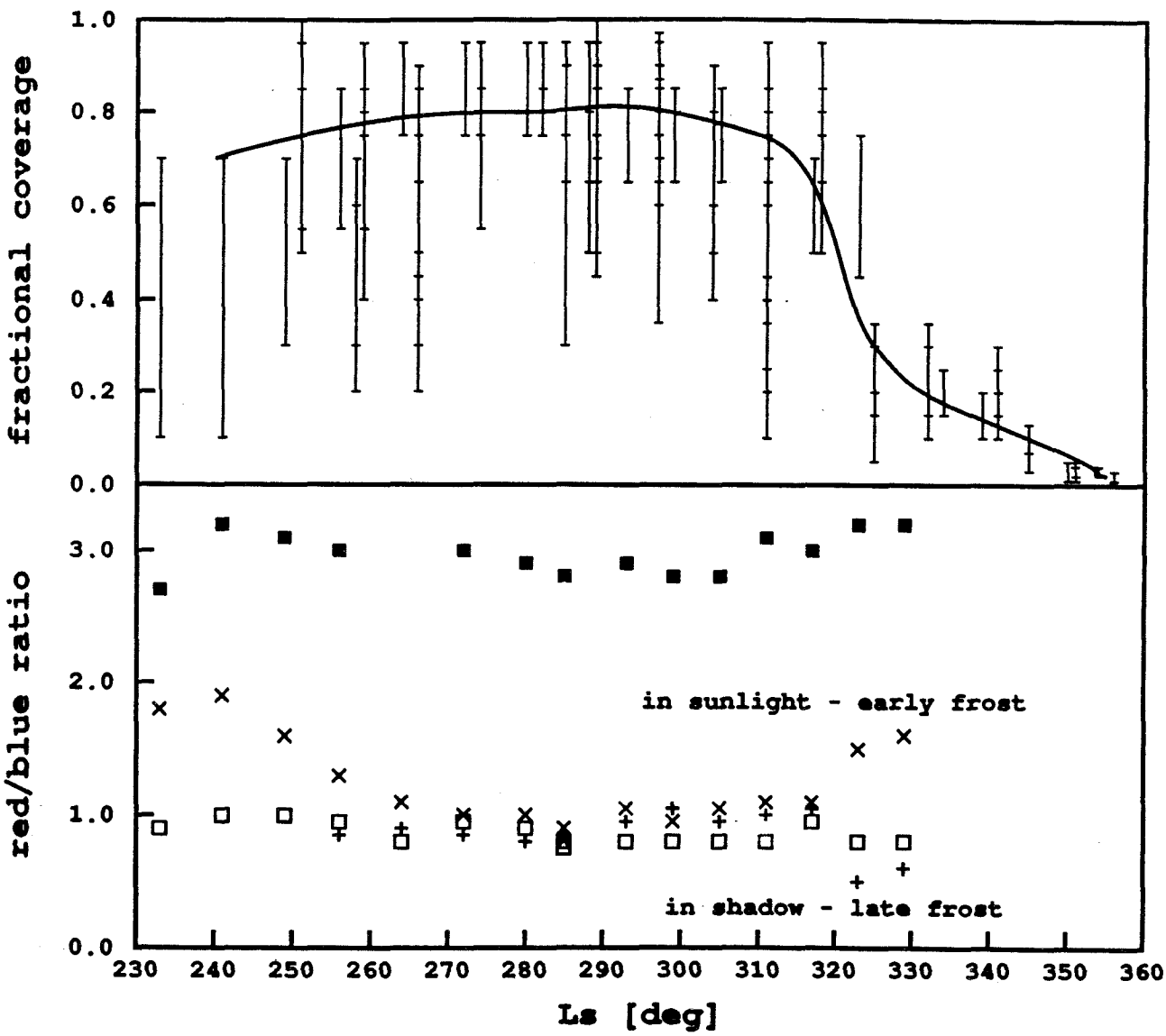

Figure 4.12 Changes of frost surface coverage and color as a function of L_S.

Figure 4.12). The disappearing frost was getting redder. This can be attributed to breaking up the surface layer and seeing more of the underlying reddish surface. On the other hand, the frost which was "destined" to stay (that is is the frost in the locally favorable areas — behind rocks, in troughs) is getting whiter. This can be explained either by a thicker layer of the water frost over red substrate or by a purer composition of recondensed frost (less dust/ice mixture).

It is interesting to compare the timing of the above mentioned transition from the full to partial surface coverage accompanied by color changes of frost. This transition occurred the first winter around $L_S = 325°$ and a few degrees earlier the second winter. Note that in Figure 4.10 it is approximately (within 5 degrees) the time when the sublimation capability of sunlight reaches the thickness that could be expected of typical continuous coverage frost — 20–50 μm. Therefore, I can conclude that the time of transition (as seen in imaging) coincides with expected transition derived from energy balance calculation.

Also note the steep slope of the solar heat input and its derived frost sublimation capability. It means that for a large portion of winter, insolation substantially lacks the energy necessary to sublime a significant amount of water frost. However, once it reaches this capability, any realistic frost layer will be sublimated very quickly (within a few days) and frost is stable only in sheltered areas — cold traps.

4.6.2 Water vapor in atmosphere — holding capacity and vertical mixing

Further tests of the model at VL-2 site can be based on the MAWD data on water vapor column abundance and its relation to the atmospheric transport of water vapor. Meridional transport of water vapor has to be limited for sublimated water vapor to be redeposited in local cold traps. Otherwise, meridianal transport will advect water vapor equatorward where it does not have to be deposited as a surface frost because atmospheric holding capacity is large compared with amount of sublimated water vapor. Meridional advection within the boundary layer itself is quite limited — water vapor has to get mixed in the atmosphere above this layer. This requires rather substantial vertical mixing of the water vapor towards altitudes above the boundary layer. In reality, the vertical mixing is limited at this latitude and season because of close-to-saturation of the atmosphere. For most of the winter, atmosphere at this latitude (VL-2 site) is saturated with water vapor during the night and above the thermal boundary during the day. This statement is based on the atmospheric temperature data and on the MAWD data (compare Figures 4.5 and 4.6). There were about 5 to 8 precipitable μm of water in the total atmospheric column (most of it within the first two scale heights). This is also supported by the evidence of morning fogs (Pollack *et al.*, 1979, Jakosky 1985, Jakosky *et al.*, 1988) and temperature inflection at the Lander sites (Ryan and Sharman 1981).

Figure 4.13 shows the estimated effect of vertical mixing of water into the almost saturated atmosphere — the diurnal cycle in the water vapor column abundance for a period of 10 sols. This is the approximate calculation of the residual water vapor content in the atmospheric boundary layer on a diurnal cycle. The calculation

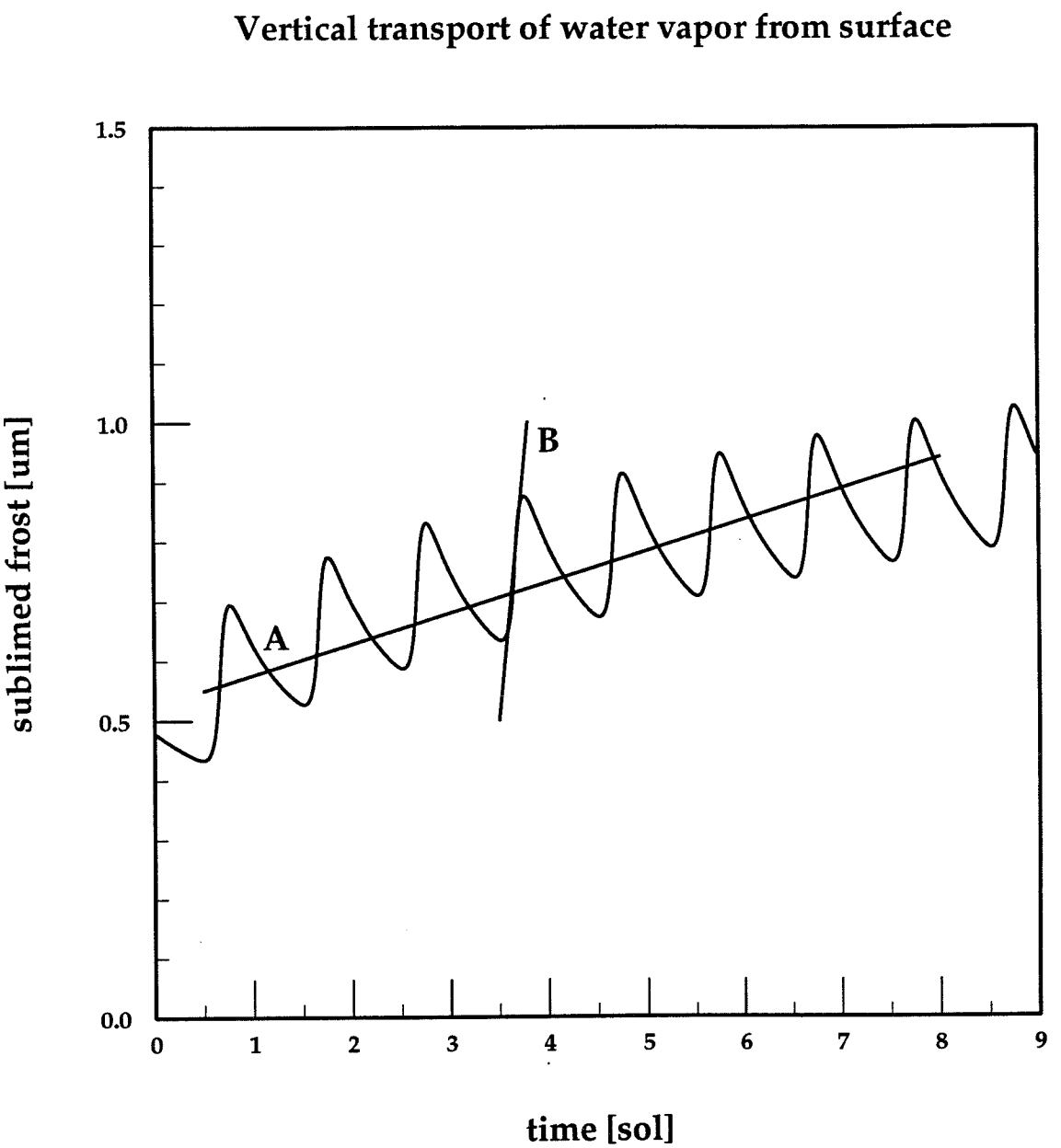

Figure 4.13 Estimated vertical mixing in the boundary layer.

is based on numerically solving the one-dimensional diffusion equation along the vertical axis z:

$$\frac{\partial \rho_{H_2O}}{\partial t} = K \frac{\partial^2 \rho_{H_2O}}{\partial z^2} \tag{4.15a}$$

The diffusion coefficient K is plotted in Figure 4.11. The initial ρ_{H_2O} corresponds to the equivalent 8 precipitable μm and is distributed uniformly. The initial constant relative humidity is approximately 60 per cent. The temperature profile is plotted in Figure 4.5 and is kept fixed for the duration of the simulation (except for the diurnal thermal boundary layer). The surface temperature and corresponding the water frost sublimation near the surface is depicted in Figure 4.10 (i.e., bottom boundary condition). The atmosphere is never allowed to saturate — water vapor diffusion upward stops if the relative humidity exceeds one hundred per cent. Any excess water vapor (above the initial concentration) which reaches the altitude of 6 km is effectively removed from the diffusion process by being stored in an effectively infinite sink above this altitude.

It is important to note that the true sublimation of the frost from the surface by solar insolation is the secular trend of the curve averaged over several sols (line A). The immediate sublimation rate (around the noon on each day) is much higher (line B — compare with Figure 4.10) but most of water vapor condenses back on the surface (cold-trapping). This calculation does not take into account the possibility of free convection during the warmest parts of a sol (very unstable atmosphere). The mixing in the boundary layer would be faster with the free convection but still does not reach the rates given by thermodynamical calculation.

There is a rapid increase in the water vapor column abundance around noon because the atmospheric thermal boundary layer approaches its highest temperature. Afterwards, there is a slow decrease in the water vapor column abundance because the thermal boundary cools down and the water vapor is redeposited from the atmosphere back on the surface. There is always a slight secular increase in the water vapor column abundance due to an increased temperature of the whole atmosphere and also because of slow mixing (leaking) of water vapor from the boundary layer to the higher altitudes where water vapor is advected equatorward. This rate of increase in the water vapor column abundance is denoted by line A.

The "leakage" from the boundary layer upward, that is, a loss from the diurnal cycle of the cold trapping, can be estimated as follows: a θ probability that a water molecule will be redeposited in a cold trap within one day is approximately the product of:

- σ fraction of surface covered by cold traps,
- "sticking" coefficient for water molecule in a water frost (which I assume at these temperatures to be close to one, about 0.8, Adamson 1982), and
- the number of times a water molecule has a chance to hit surface.

The last factor is just the ratio of the diurnal vertical distance traveled by random turbulence motion in the boundary layer over the eddy diffusion layer thickness. Therefore:

$$\theta \approx \sigma \cdot 0.8 \cdot w\prime \cdot \sqrt{t_D/K} \tag{4.16}$$

where $w\prime$ is the average deviation from the mean vertical velocity ($\approx 5m/sec$), t_D is the duration of the day, and K is the eddy diffusion coefficient ($\approx 10^2 m^2 s^{-1}$ – Figure 4.11 and Jakosky 1985). For $\sigma \approx 0.1$ (typical for the VL-2 site), I get θ close to one (within a factor of 2).

The numerical diffusion model (shown in Figure 4.13) with the parameters for mixing in the boundary layer as presented in the previous section gives the diurnal cold-trapping efficiency equal to 0.9, and thus, confirms the estimate above.

4.6.3 Conclusions about quantitative tests

There are three primary conclusions to be derived from the quantitative test of my hypothesis at the VL-2 site. First, there is a transition in the frost surface coverage and color. The timing of the transition is consistent with the layer thickness derived from the amount of water vapor in the atmosphere before winter frost formation (10–30 μm). The timing of disappearance of the frost in cold-traps in consistent with the thickness of 100–200 μm. The change in color (from slightly reddish tint to, probably, "bluish" tint) is consistent with the fresh frost redeposition into cold traps where it covers the mixture of thin-frost and dust.

Second, there is no comparable increase in the atmospheric water vapor column during the transition, not until about $20° L_S$ later. In the meantime, the water had to be stored somewhere because I see disappearance of the continuous frost coverage. This is consistent with the most of water stored in the cold traps as a frost.

Third, there is not much chance of water vapor being advected quickly (i.e., within a few sols) to the lower latitudes. The vertical mixing in the boundary layer of the almost saturated winter atmosphere is very limited and therefore water vapor cannot get into higher altitude and thus being transported globally. It has to stay close to the ground where chance of hitting the surface at the cold traps is close to one on diurnal time scale.

From these three arguments, I can conclude that my hypothesis about the cold trapping of water frost at the VL-2 site is consistent with the quantitative tests described in this section.

4.7 Observations of edge of northern seasonal frost during spring

One consequence of the theory of the cold-trapping is an effective delay by about 20 degrees of L_S in the release of water which was condensed as a surface frost during the winter. Indeed, the difference which was observed between the latitude of the peak water vapor column abundance and the latitude of the edge of the retreating CO_2 seasonal ice cap may require a mechanism for delayed release of water. Both the surface temperature and water vapor column abundance as a function of L_S are presented in Figure 4.14 for the northern seasonal cap during the spring. The surface temperature (upper curve) is measured by the 20 μm band of the IRTM instrument. The drop to 150 K surface temperature occurs at the latitude of the edge of the seasonal CO_2 frost. The boundary is not sharp because the data were binned in 2 deg bins in latitude and averaged around Mars in longitude. The water vapor column abundance data (lower curve) were measured by the MAWD instrument

and again averaged in 2 deg steps in latitude and around Mars in longitude. The data in Figure 4.14 are an average for the period of $L_S = 50° - 60°$.

Assuming that the CO_2 seasonal frost acts as a sink for water vapor seen in the atmosphere during the summer and early fall then the edge of the retreating seasonal cap should behave as a source for atmospheric water vapor. There could be, of course, no release of water vapor before the CO_2 frost retreats. However, once the CO_2 sublimates, the water vapor should appear in the atmosphere rather quickly and then be transported equatorward. Therefore, the peak of water vapor column abundance should occur just above the edge of the retreating seasonal cap. This is not, obviously, the case in Figure 4.14. The peak of water vapor is southward from the edge of the retreating seasonal cap by about 10° in latitude, which corresponds to the delay of about $20° L_S$, or 35 sols.

This is a global phenomenon and could arise from:

- seasonal water vapor release from the regolith, not from the CO_2 frost,
- residual water frost substrate below the seasonal CO_2 frost being released gradually as the surface slowly heats up,
- observational effect of clouds,
- temporary water storage in clouds, or
- water frost temporarily locked in local cold traps created by small-scale surface roughness as I have interpreted happened locally at the VL-2 site.

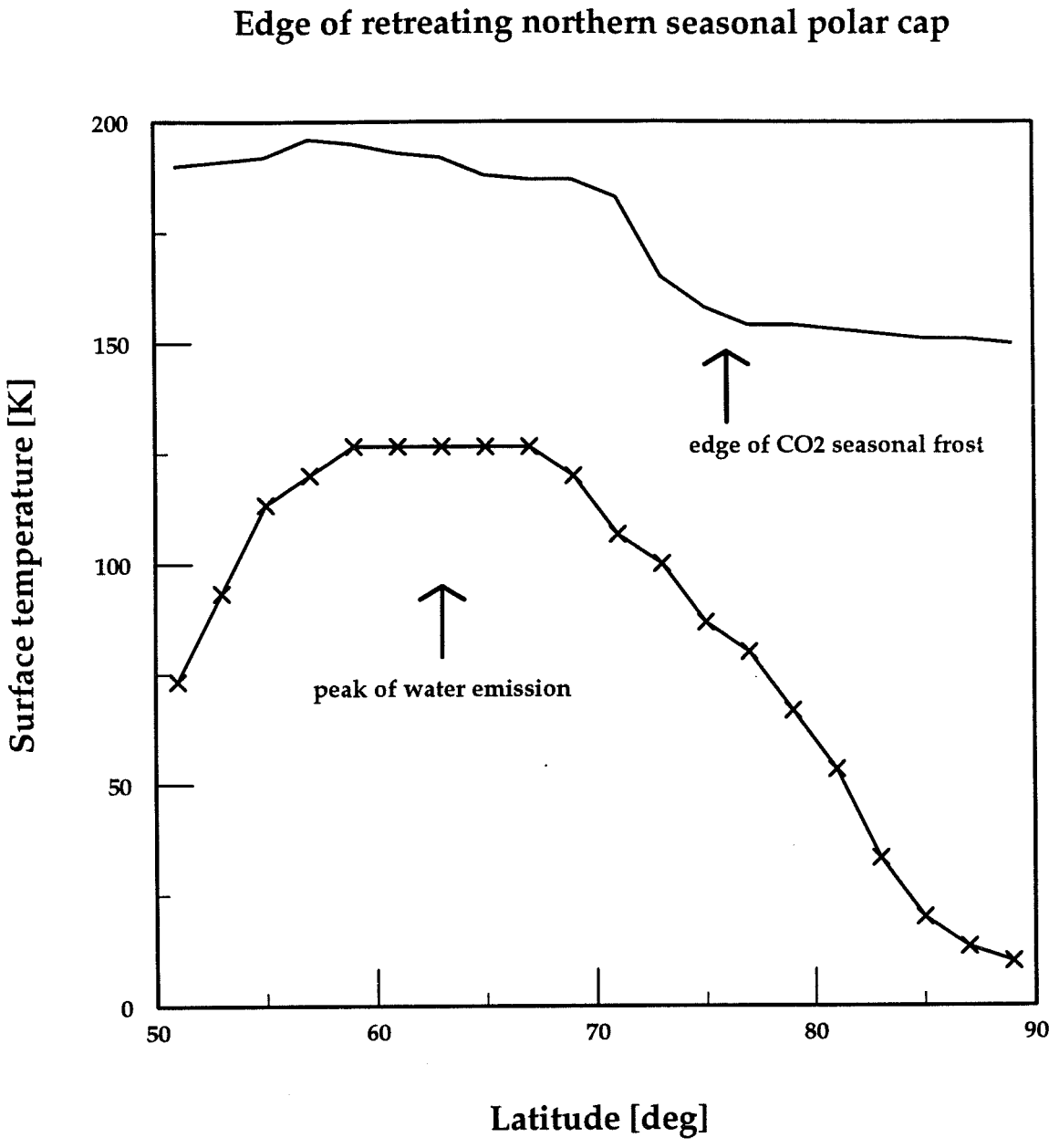

Figure 4.14 Difference between the latitude of the peak water vapor column abundance (as seen in the MAWD instrument on Viking Orbiter) and the latitude of the edge of the retreating CO_2 seasonal ice cap (a sharp drop of IRTM surface temperature towards 150 K). The MAWD data are an average for $L_S = 50° - 60°$.

The first possibility (seasonal water vapor release from the regolith) requires either unrealistic high regolith permeability to repeatedly release several tens of precipitable μm of water during the spring for many years or continuous replenishment from the atmosphere during other seasons. The continuous replenishment mechanism is definitely strongly based on a rigorous model (Jakosky 1983). However, I have to frankly admit my certain doubts about the initial assumption of this model — the equal value of a diffusion constant for diffusion in and out of regolith. Some models of micro-physics of the diffusion of vapor through regolith could yield higher values for a diffusion constant of water vapor from the regolith as compared with the diffusion back into the regolith from the atmosphere. Therefore, I believe that further work may still be needed in order to decide about this possible directional asymmetry in the diffusion constant.

The second possibility (residual water frost substrate gradually released) falls far short of providing the observed delay of water release. One sol is quite sufficient to raise the temperature of a sunlit fraction of the surface from 150 K to 190 K (equilibrium temperature for the latitude of 65° in Figure 4.14). Therefore, it would be quite difficult to use this explanation as basis for the 35 sol delay. Also, there is no evidence in Viking Orbiter imaging to support the existence of this water ice substrate below CO_2 seasonal frost.

The third possibility (observational effect of water vapor clouds) suffers from the fact that the polar hazes extend at most only a few degrees south of the polar cap edge (Christensen and Zurek, 1984). The difference in latitudes in Figure 4.14 is larger than that (about 10°).

The fourth possibility (water storage in clouds) does not provide a reservoir which would be large enough. The optical depth of hazes is about unity which corresponds to only 1–2 precipitable micrometers of water ice (Christensen and Zurek, 1984).

Finally, the fifth possibility (the temporary cold trapping model proposed in this paper) seems to be consistent with all the observations. There is, obviously, no direct evidence, only a set of circumstantial observations and physical arguments as described in the previous section. And, of course, I cannot exclude that some combination of effects mentioned above, possible with others which I did not put forth, will provide the consistent explanation. Still, the cold-trapping of water due to small scale roughness could be the relevant model for the global behavior of water on Mars.

This assertion is based on the following model: once the water vapor sublimation becomes possible (i.e., after disappearance of the seasonal CO_2 frost), in a very short time ($\approx$ 1 sol) 20 precipitable micrometers of water vapor can be released into the atmosphere. However, the long-range transport is limited for another $\approx 20° L_S$. This is due to still relatively cold atmosphere and slow mixing through the boundary layer. Therefore, water vapor can be transported only over relatively short distances (at most, few tens of kilometers). But the water vapor gets into contact with surface during the transport through boundary layer and it is redeposited back on the surface, preferentially at the colder areas created by the small-scale roughness (i.e., in cold traps). Eventually (in $20° L_S$), continuous transport through the atmospheric boundary layer coupled with the increased atmospheric temperature will allow all water frost to sublime away — even at the cold traps.

4.8 Conclusions

In this chapter, I have reviewed and considered the physics of the frost sublimation and condensation in the presence of the Martian atmosphere. As well, I have subjected this physical processes to a test case — winter frost observed by the Viking Lander 2.

I have presented quantitative evidence for the cold-trapping at the VL-2 site. This evidence consists of the frost surface coverage and color transition, timing of this transition, and limited vertical mixing and horizontal water vapor transport. Moreover, I believe that the cold-trapping must be a general property of seasonal frost and, therefore, must be considered in order to understand the evolution of the VL-2 winter frost and the surface environment of Mars in general.

My study of the VL-2 observations suggests that H_2O frost occurs in two forms:

- thin, almost continuous, early frost, and
- much thicker, patchy, later frost.

Both frost forms contain essentially the same total water content but they cover different fractions of the surface. The transition between two frost forms occurs by recondensation at local cold traps when solar insolation sublimates the first frost but the atmosphere is still too cold to transport the resultant water vapor away. These cold traps are created by shadowing from the small scale surface roughness — rocks, troughs, etc.

This hypothesis hinges on the disparity between the local and long-range transport capabilities of water vapor by the atmosphere. The local transport is driven by

abundant insolation energy available at the time of transition. This results in a large fraction of surface frost being redistributed rapidly into locally thermodynamically preferable locations — cold traps. Long range transport is constrained by the atmospheric carrying capacity. At the time of transition, the atmosphere is still cold, not far from its winter minimum, and is almost saturated by residual water vapor (5 to 8 precipitable microns). Therefore, it cannot carry much additional water vapor to lower latitudes. This disparity delays the global transport of water vapor by the atmosphere. It is important that such behavior is hinted by correlating the Viking IRTM and MAWD observations over the edge of the northern seasonal polar cap during the spring.

Mars Observer is expected to provide several potential measurements which could further verify the theory of the cold-trapping. There should be a small but consistent discontinuous albedo change of the water frost at the time when the surface energy balance will allow water to sublime. This may be interpreted in terms of water frost recondensation. Such data could be provided by the Mars Observer Camera (surface reflectance) and Thermal Emission Spectrometer (surface temperature). Also, the phase lag in water release to the atmosphere from the seasonal CO_2 frost could be observed by Pressure Modulated Infrared Radiometer (water vapor content in the atmosphere) and Thermal Emission Spectrometer (presence of CO_2 or water frost on the surface). Finally, the phase function of the thin frost may be measured in the visible wavelengths.

Chapter 5

Summary of Conclusions

I have tried to show in two specific cases (frost–surface morphology and Viking Lander 2 winter frost) the importance of small–scale processes and properties for understanding remote–sensing observations and for global modeling. I have presented both theoretical and observational evidence for inherently rough, volatile–surface morphology and for cold trapping at the VL-2 site.

It is mandatory to consider these effects if one wants to interpret correctly remote–sensing observations. Both these effects play a fundamental role in surface–frost thermal–balance calculations. Indeed, proper understanding of this issue is absolutely required to implement correctly the boundary conditions and parameterizations used in global numerical models of the volatiles' behavior on Mars.

In the first case, the evidence consists of a model of a rough–surface thermal balance, and of the terrestrial analogs of differential–sublimation structures. I concluded that there is a natural tendency for a volatile surface to develop spontaneously small–scale roughness in a sublimation–dominated environment. This behavior

- can be plausibly predicted from "first principles,"

- is difficult to model exactly,
- is observed to occur on the Earth,
- may be tested by the Mars Observer,
- has important implications for future studies of the water (and possibly for carbon dioxide) frost on Mars.

In the second case, the evidence consists of frost surface coverage and color transition, of the timing of this transition, and of the limited vertical mixing and horizontal water–vapor transport. My study of the VL-2 winter–frost observations suggests that H_2O frost occurs in two forms:

- thin, almost continuous, early frost, and
- much thicker, patchy, later frost.

Both frost forms contain essentially the same total water content but they cover different fractions of the surface. The transition between two frost forms occurs by recondensation at local cold traps when solar insolation sublimates the first frost but when the atmosphere is still too cold to transport the resultant water vapor away. These cold traps are created by shadowing from small–scale surface roughness — rocks, troughs, etc. This theory hinges on the disparity between local and long–range transport of water vapor by the atmosphere. The local transport is driven by abundant insolation energy available at the time of transition. This results in a large fraction of surface frost being redistributed rapidly into locally thermodynamically preferable locations — cold traps. Long–range transport is constrained by the atmospheric carrying capacity. At the time of transition, the atmosphere is still

cold, not far from its winter minimum, and is almost saturated by residual water vapor (5 to 8 precipitable micrometers). It cannot carry much additional water vapor to lower latitudes. This disparity delays the global transport of water vapor by the atmosphere.

I believe that inherent rough–surface morphology and frost cold–trapping must be general properties of at least some forms of seasonal and residual frost. Both effects must be considered in order to understand the global observations of Martian frost and the surface environment of Mars in general.

In order to confirm conclusively that these proposed mechanisms exist in a more general role on Mars, we are going to need more comprehensive data than those provided by the Viking mission. The Mars Observer could be an effective platform for acquisition of such data. The next few paragraphs describe possible observational tests.

In principle, differential–sublimation features in Martian seasonal and residual polar frost may be directly imaged from an orbiting spacecraft. That would be the most convincing argument. However, I expect such direct observations by the Mars Observer Camera to be only marginally possible, given the scale of terrestrial analogs of these features.

The more probable verification of the existence of differential–sublimation features is by indirect observations. There are several possibilities. In the first place, one can utilize the property found in terrestrial *penitentes*, which typically line up along the direction of the ground trace of the diurnal motion of the Sun or more specifically along the direction of maximum insolation. This is typically east–west, but it may

be modified by the presence of large–scale topography. This property is true even for polar regions. The ideal geometry for such a measurement would be from a polar–orbiting spacecraft with the local noon time of the equator crossing. One should find asymmetry in the phase integral measured in a) the orbital plane (along–track) and b) the plane normal to the orbital plane (cross–track). Approximately, these two planes correspond to the local north–south and east–west directions on the surface (Figure 3.9a).

The roughness/temperature feedback acts primarily normal to the ground trace of the maximum insolation (approximately east–west). Therefore, the surface would be relatively smooth in this direction — we are observing along the longitudinal axis of the saw–tooth pattern shown in Figure 3.9. This is reflected by labeling the symmetrical distribution of radiance in Figure 3.10 as "smooth (east–west)." For the completely smooth frost surface, radiance dependence on the viewing geometry would be symmetrical around the azimuth of the subsatellite point.

For the rough–frost surface, the peak in surface reflectance will shift towards lower phase angles, closer to the incidence direction of sunlight. This is in the left direction in Figure 3.9b. The radiance profile would be more steep, less Lambertian, as is shown by the curve with the label "rough (north–south)."

In fact, for the completely Lambertian surface, there would be no dependence of radiance on the emission angle. For the Lambertian surface, the reflectance drops off as $\cos\theta$, but the geometry factor (provided a target fills the field of view of the instrument) goes as $1/\cos\theta$, and these two factors cancel each other.

Second, the relationship between surface reflectivity and brightness temperature may also reveal the presence of differential–sublimation features. This is depicted in

Figure 3.11. There is an obvious and general relationship between an effective albedo and surface temperature — negative correlation. This relationship is depicted as "T(typical)" in Figure 3.11. For a rough surface, this relationship could vary with the viewing geometry. For example, it was suggested that differential–sublimation features play a critical role in shielding the CO_2 residual frost from direct sunlight at the southern polar frost (Paige *et al.*, 1990).

There may be CO_2 frost "hiding" along the longer (less–illuminated) side of the saw–tooth pattern in Figure 3.9. In that case, this cold frost may not be visible (for brightness–temperature measurements) for the observation geometry near the zero–phase angle when a more illuminated surface (which is predominantly H_2O ice) fills the field–of–view of the instrument (that is, of course, the whole idea of hiding the CO_2 frost). This concept assumes non–uniform temperature distribution across differential–sublimation features. As we move to larger phase angles and increase the emission angle (moving right in Figure 3.9b), we see less radiance in visible wavelengths (because of more multiple scattering, Figure 3.10), but also because of smaller brightness temperatures.

Therefore, in this situation we measure a completely reversed relationship between surface reflectance and brightness temperature for a rough surface consisting of an H_2O and CO_2 mixture than we would a the similar smooth surface. The coupled measurements using visible and thermal infrared imaging systems would be required to verify this hypothesis.

Unfortunately for both examples shown in Figures 3.10 and 3.11, the Mars Observer Camera (MOC) utilizes a pushbroom technique for surface imaging (the left side

of Figure 3.9b), and the surface–emission angle is constant. One must look therefore for second–order effects to ascertain the presence of differential–sublimation features in polar frost. Any such measurement is inherently difficult because of the separating effects of i) large–scale topography, ii) small–scale roughness, and iii) surface–material properties, on phase function observations. In the ideal case, the direct measurement of the bidirectional reflectance–distribution function (BRDF) would be the most useful (the right side of Figure 3.9b). The Thermal Emission Spectrometer (TES) may be able to provide some of this information because of its multiple viewing–angle capability. This is similar to the terrestrial measurement by the Multi–Angle Imaging Spectro–Radiometer (MISR) built by JPL for EOS. Or a frame–type camera (similar to Viking or Voyager) would be useful for retrieving the phase function of a polar–frost surface. Neverthless, for this experiment, a Mars'94 thermal–mapping radiometer (Termoskan II) with variable viewing geometry might also be suitable. In any case, TES has an important role in identifying the surface composition of southern residual frost.

Third: Fortunately, the Sun–synchronized orbit of the Mars Observer and the fixed nadir pointing combined with the Mars Observer Camera Medium Resolution mode provide an ideal vehicle for studying the seasonal evolution of polar–frost surface reflectance. This measurement could not have been done with previous spacecraft, as those were not in polar orbit. At the same time, the more variable Mars'94 orbit may be better for complementary phase–function observations with varying–illumination geometry. The lower resolution of Mars'94 cameras should not constitute any difficulty for this observation.

The development of differential–sublimation features will cause the surface reflectance of seasonal frost to increase rapidly with time shortly after insolation

first reaches the frost. This effect should be observable with repeated imaging by MOC. The difficult task is in separating the effect of changes in the properties of frost surface (for example, Paige 1985; Keiffer 1990) from the effect of small–scale roughness.

A very important property of these postulated polar frost features could be strong backscattering of a radio signal at wavelengths comparable to the suggested scale of differential–sublimation features. There are some hints that this was already observed by ground observations (Muhleman *et al.*, 1991). However, I feel that this is a rather premature interpretation and prefer to wait for observations with a better spatial resolution from orbiting spacecraft. There are also alternative explanations for this observation (Hapke 1990). Another possible confirmation is randomization of the signal polarization that is due to multiple scattering from roughness elements. Unfortunately, there will be only a limited radio–science capability on the Mars Observer and Mars'94.

Ideally, confirmation of the hypothesized differential–sublimation structures would be by direct, visual observations on the surface. The only near–term candidates appear to be the Mars Balloon of the Mars'96 mission (Linkin *et al.*, 1989). There is a slight chance of a Mars Balloon travelling through the northern residual frost on the basis of the preliminary plans. Some of the proposed future U.S. hard landers or penetrators could land at a high latitude and so perform a similar function. It does not seem to be feasible for a rover (large or mini) to land at a latitude high enough during the upcoming decade of Mars exploration. However, depending on the final outcome, a possible follow–up Mars Observer mission could have improved the imaging resolution so that direct observation of the differential–sublimation features would be possible even from the orbit.

In the case of cold–trapping, the Mars Observer is expected to provide several potential measurements. There should be a small but consistent, discontinuous albedo change of water frost at the time when the surface–energy balance will allow water to sublime. This may be interpreted in terms of water–frost recondensation. Such data could be provided by the Mars Observer Camera (surface reflectance) and Thermal Emission Spectrometer (surface temperature). Also, the phase lag in water release to the atmosphere from seasonal CO_2 frost could be observed by Pressure Modulated Infrared Radiometer (water–vapor content in the atmosphere) and Thermal Emission Spectrometer (presence of CO_2 or water frost on the surface). Finally, the phase function of thin frost may be measured in the visible wavelengths.

Finally, I wish to conlude this work by stating the importance of direct measurement of water vapor *in situ* on the surface of Mars. Such a measurement should be considered to be a mandatory experiment on any future surface mission and is critical for understanding the diurnal and seasonal water cycle and water reservoirs. I believe that there are enough potential, technological solutions to produce a practical, solid–state water–vapor detector for these future Mars missions. The challenge of the low temperature, and hence the long–time constant, is real, but these problems can be overcome by commitment to perform such a crucial scientific observation.

Bibliography

Adams, E E, and R L Brown, 1983. Metamorphism of dry snow as a result of temperature gradient and vapor density differences. *Ann Glaciol,* **4,** 3–9.

Adamson, A W, 1982. *Physical Chemistry of Surfaces.* John Wiley, Inc, New York.

Adorjan, A S, 1969. Temperature distribution in shadowed lunar craters. *J Spacecraft,* **7,** 378–380.

Amstutz, G C, 1958. On the formation of snow *penitentes. J Glaciol,* **3,** 304–311.

Andreas, E L, and S F Ackley, 1982. On the differences between ablation seasons of Arctic and Antarctic sea ice. *JAS,* **39,** 440–447.

Arvidson, R E, E A Guiness, H J Moore, J E Tillman, and S D Wall, 1983. Three Mars years: Viking Lander 1 imaging observations. *Science,* **222,** 463–468.

Ashwell, I Y, and F G Hannell, 1966. Experiments on a snow–patch in the mountains of Sweden. *J Glaciol,* **6,** 135–144.

Ball, F K, 1954. Dirt polygons on snow. *Weather,* **9,** 322–323.

Bastin, J A, and D O Gough, 1969. Intermediate scale lunar roughness. *Icarus,* **11,** 289–319.

Bell, E B, L Eisner, J Young, and R A Oetjen, 1960. Spectral radiance of sky and terrain at wavelengths between 1 and 20 microns. II. Sky measurements. *J OSA,* **50,** 1313–1320.

Brown, R H, and D L Matson, 1987. Thermal effects of insolation propagation into regolith of airless bodies. *Icarus,* **72,** 84–94.

Brutsaert, W, 1982. Evaporation into the atmosphere. D. Reidel Publishing Co., Dordrecht, Holland.

Buhl, D, W J Welch, and D G Rea, 1968. Reradiation and thermal emission from illuminated craters on the lunar surface. *JGR,* **73,** 5281–5295.

Carr, M H, 1986. Mars: A water-rich planet? *Icarus,* **68,** 187–216.

Christensen, P R, and R W Zurek, 1984. Martian north polar hazes and surface ice. *JGR,* **89,** 4587–4596.

Clark, R N, 1980. The surface condensates on Mars observed by Viking: Frost layers several tenths of a millimeter thick. *LPI Abstract,* 160–161.

Clifford, S M, 1989. Personal communication.

Clifford, S M, and D Hillel, 1986. Knudsen diffusion: the effect of small pore size and low gas pressure on gaseous transport in soil. *Soil Science,* **141,** 289–297.

Clow, G D, C P McKay, G M Simmons, and R A Wharton, 1988. Climatological observations and predicted sublimation rates at Lake Hoare, Antarctica. *J Climate,* **1,** 715–728.

Colbeck S C, 1983. An overview of seasonal snow metamorphism. *Rev Geo Space Phys,* **20,** 45-61.

Colwell, J E, and B M Jakosky, 1987. The evolution of topography on a comet. *Icarus,* **72,** 128–134.

Colwell, J E, B M Jakosky, B J Sandor, and S A Stern, 1990. Evolution of topography on comets. II. Icy Craters and Trenches. *Icarus,* **85,** 205–215.

Crank, 1954. *The Mathematics of Diffusion.* John Wiley, Inc, New York.

Davies, D W, 1979a. The vertical distribution of Mars water vapor. *JGR,* **84,** 2875–2879.

Davies, D W, 1979b. The relative humidity of Mars' atmosphere. *JGR,* **84,** 8335–8340.

Davies, D W, C B Farmer, and D D LaPorte, 1977. Behavior of volatiles in Mars' polar areas. *JGR,* **82,** 3815–3822.

Dorsey, N E, 1940. *Properties of Ordinary Water-substance.* Reinhold Publishing Corp, New York.

Drewry, D J, 1972. A quantitative assessment of dirt cone dynamics. *J Glaciology,* **11,** 431–446.

Flasar, F M, and R M Goody, 1975. Diurnal behavior of water on Mars. *Planet Space Sci Rev,* **34,** 161–181.

Guiness, E A, R E Arvidson, and D C Gehret, 1979. Color changes at the Viking landing sites over the course of a Mars year. *JGR,* **84,** 8355–8364.

Guiness, E A, C E Leff, and R E Arvidson, 1982. Two Mars years of surface changes seen at the Viking Lander sites. *JGR,* **87,** 10051–10058.

Haberle, R M, and B M Jakosky, 1991. Transport of water from residual north polar cap on Mars. In press.

Hansen, O L, 1977. An explication of the radiometric method for size and albedo determination. *Icarus,* **31,** 456–482.

Hapke, B, 1981. Bidirectional reflectance spectroscopy. 1. Theory. *JGR,* **86,** 3039-3054.

Hapke, B, 1984. Bidirectional reflectance spectroscopy. 3. Correction for macroscopic roughness. *Icarus,* **59,** 41–59.

Hapke, B, 1990. *Icarus,* **88,** 407-412.

Hart, H M, and B M Jakosky, 1986. Composition and stability of the condensate observed at the Viking Lander 2 site on Mars. *Icarus,* **66,** 134–142.

Hastenrath, S, and B Koci, 1981. Micromorphology of the snow surface at the Quelccaya Ice Cap, Peru. *J Glaciol,* **27,** 423–428.

Hess, S L, R M Henry, C B Leovy, J A Ryan, and J E Tillman, 1977. Meteorological results from the surface of Mars: Viking 1 and 2. *JGR,* **82,** 4559–4574.

Holton, J R, 1979. *An Introduction to Dynamic Meteorology.* Academic Press, New York.

Ingersoll, A P, 1970. Mars: Occurrence of liquid water. *Science,* **168,** 972–973.

Ingersoll, A P, 1974. Mars: The case against permanent CO_2 frost caps. *JGR,* **79,** 3403–3410

Jahn, A, and M Klapa, 1968. On the origin of ablation hollows (polygons) on snow. *J Glaciol,* **7,** 299–312.

Jakosky, B M, 1979. The effects of non–ideal surfaces on the derived thermal properties of Mars. *JGR,* **84,** 8252–8262.

Jakosky, B M, 1982. Ph.D. thesis, California Institute of Technology, Pasadena.

Jakosky, B M, 1983. The role of seasonal reservoirs in the Mars water cycle — I. Seasonal exchange of water with the regolith. *Icarus,* **55,** 1–18.

Jakosky, B M, 1985. The seasonal cycle of water on Mars. *Space Sci Rev,* 41, 131–200.

Jakosky, B M, 1986. On the thermal properties of Martian fines. *Icarus,* 66, 117–124.

Jakosky, B M, R W Zurek, and M R La Pointe, 1988. The observed day–to–day variability of Mars atmospheric water vapor. *Icarus,* **73,** 80–90.

Jones, K L, R E Arvidson, E A Guiness, S L Bragg, S D Wall, C E Carlston, and D G Pidek, 1979. One Mars year: Viking Lander imaging observations. *Science,* **204,** 799–806.

Kieffer, H H, T Z Martin, E D Miner, F D Palluconi, A R Peterfreund, and B M Jakosky, 1977. Thermal and albedo mapping of Mars during the Viking Primary Mission. *JGR,* **82,** 4249–4291.

Kieffer, H H, 1990. H_2O grain size and the amount of dust in Mars' residual north polar cap. *JGR,* **95,** 1481–1494.

Kotlyakov, V M, and I M Lebedeva, 1974. Nieve and ice penitentes. *Zeitschrift fur Gletscherkunde und Glazialgeologie,* **Bd. X,** 111–127.

Kraus, H, 1966. Freie und bedeckte Ablation. *Khumbu Himal,* **1,** 203–235.

Leighton, R B, and B C Murray, 1966. Behavior of carbon dioxide and other volatiles on Mars. *Science,* **153,** 136–144.

Lindal, G F, 1979. Viking Radio occultation measurements of the atmosphere and topography of Mars. *JGR,* **84,** 8443–8456.

Linkin, V M, 1989. The Mars Balloon system for the Mars 1994 missions. *IAF Paper 89-488.*

Lliboutry, L, 1954. The origin of *penitentes*. *J Glaciol,* **2,** 331–338.

Lliboutry, L, 1956. Nieves y Glaciares de Chile. Ediciones de la Universidad de Chile, Santiago de Chile.

Malin, M C, and J Zimbelman, 1988. Surface morphology of cometary nuclei. Unpublished manuscript.

Moore H, R E Hutton, G D Clow, and C R Spitzer, 1987. Physical properties at the Viking Lander sites. *USGS Professional Paper 1389.*

Muhleman D O, B J Butler, A W Grossman, and M A Slade, 1991. Radar Images of Mars. *Science,* **253,** 1508–1513.

Murray, B C, *et al.*, 1990. Preliminary assessment of Termoskan observations of Mars. Submitted to Planet Space Sci Rev.

Paige, D A, 1985. Ph.D. thesis, California Institute of Technology, Pasadena.

Paige, D A, K E Herkenhoff, and B C Murray, 1990. Mariner 9 observations of the South polar cap of Mars: Evidence for residual CO_2 frost. *JGR,* **95,** 1319–1336.

Pettit, E, and B Nicholson, 1930. Lunar radiation and temperatures. *Astroph J,* **71,** 102-135.

Pffefer, W T, and C S Bretherton, 1987. The effect of crevasses on the solar heating of a glacier surface. *IAHS Publ,* **170,** 191–205.

Plate, E J, 1971. Aerodynamic characteristics of atmospheric boundary layers. AEC Critical Review Series.

Pollack, J B, D S Colburn, F M Flasar, R Kahn, C E Carlston, and D Pidek, 1979. Properties and effects of dust particles suspended in the Martian atmosphere. *JGR,* **84,** 2929–2945.

Pollack, J B, C B Leovy, P W Greiman, and Y Mintz, 1981. A Martian general circulation experiment with large topography. *JAS,* **38,** 3–29.

Post, A, and E R LaChapelle, 1971. *Glacier Ice.* University of Washington Press, Seattle.

Press, W H, B P Flannery, S A Teukolski, and W T Vetterling, 1988. *Numerical Recipes in C.* Cambridge University Press.

Priestley, C H B, 1959. Turbulent transfer in the lower atmosphere. Univ of Chicago Press, Chicago.

Rhodes, J J, R L Armstrong, and S G Warren, 1987. Mode of formation of "ablation hollows" controlled by dirt content of snow. *J Glaciol,* **33,** 135–139.

Richardson, W E, and R D M Harper, 1957. Ablation polygons on snow — further observations and theories. *J Glaciol,* **3,** 25–27.

Rudy, D P, 1988. Ph.D. thesis, California Institute of Technology, Pasadena.

Ryan, J A, and R D Sharman, 1981. Water frost point detection on Mars? *JGR,* **86,** 503–511.

Saari, J M, and R W Shorthill, 1963. Isotherms of crater regions on the illuminated and eclipsed Moon. *Icarus,* **2,** 115–136.

Schwerdtfeger, W, editor, 1976. *Climates of Central and South America.* Elsevier Scientific Publishing Company, Amsterdam.

Seiff, A, and D B Kirk, 1977. Structure of the atmosphere of Mars in summer at midlatitudes. *JGR,* **82,** 4364–4378.

Sharp, R P and M Malin, 1984. Surface geology from Viking Landers on Mars: Second look. *GSA Bull,* **95,** 1398–1412.

Sloan R, J H Shaw, and D Williams, 1955. Infrared emission spectrum of the atmosphere. *J OSA,* **45,** 455–460.

Smith, A M, K E Tempelmeyer, P R Muller, and B E Wood, 1969. Angular distribution of visible and near IR radiation reflected from CO_2 cryodeposits. *AIAA J,* **7,** 2274–2280.

Snyder, C W, 1979. The planet Mars as seen at the end of Viking Mission. *JGR,* **84,** 8487–8519.

Spencer, J R, 1990. A rough–surface thermophysical model for airless planets. *Icarus,* **83,** 27–38.

Sutton, J J, C B Leovy, and J E Tillman, 1979. Diurnal variations of the Martian surface layer meteorological parameters during the first 45 sols at the Viking Lander sites. *JAS,* **35,** 2346–2355.

Sutton, O G, 1953. *Micrometeorology.* McGraw–Hill Book Co, New York.

Svitek, T, and B C Murray, 1988. *Penitentes* on Mars? Abstract, 4th International Mars Conference.

Svitek, T, and B C Murray, 1990. Winter frost at Viking Lander 2 site. *JGR,* **95,** 1495–1510.

Takahashi, S, T Fujii, and T Isida, , 1973. Origin and development of polygonal ablation hollows on a snow surface. *Low Temperature Science,* Series A, **31,** 191–207.

Toon, O B, J B Pollack, W Ward, J A Burns, and K Bilski, 1980. The astronomical theory of climate change on Mars. *Icarus,* **44,** 552–607.

Troll, C, 1942. Busserschnee in den Hochgebirgen der Erde. *Petermanns Geographische Mitteilungen,* **Nr. 240.**

von Hofmann, G, 1963. Zum abbau der Schneedecke. *Archiv fur Meteorologie, Geophysik und Bioclimatologie,* **B13,** 1–20.

von Hofmann, G, 1967. Zur Rolle des Warmehaushaltes bei der Selektiven Ablation. 259–266.

Wall, S D, 1981. Analysis of condensates formed at the Viking 2 Lander site – the first winter. *Icarus,* **47,** 173–183.

Warren, S G, 1982. Optical properties of snow. *Rev Geoph Space Phys,* **20,** 67–89.

Wilson, J W, 1953. The initiation of dirt cones on snow. *J Glaciol,* **2,** 281–287.

Winter, D F, and J A Krupp, 1971. Directional characteristics of infrared emission from the Moon. *Moon,* **2,** 279–292.

Wright, C S, and R E Priestley, 1922. *Glaciology — British Terra Nova Antarctic Expedition.* Harrison and Sons, London.

Zent, A P, 1986. Distribution and state of water in the high–latitude shallow subsurface of Mars. *Icarus,* **67,** 19–36.

Zurek, R W, 1982. Martian great dust storms: an update. *Icarus,* **50,** 288–310.